

# High Power Femtosecond Doubly Resonant Optical Parametric Oscillator

Von der Fakultät für Mathematik und Physik  
der Gottfried Wilhelm Leibniz Universität Hannover  
zur Erlangung des Grades

**Doktor der Naturwissenschaften**

- Dr. rer. nat. -

genehmigte Dissertation

von

**Christian Markus Dietrich, M. Sc.**

geboren am 26.12.1988 in Goch

2023

Referent: Prof. Dr. Uwe Morgner

Korreferent: Prof. Dr. Detlev Ristau

Korreferent: Prof. Dr. Carsten Fallnich

Tag der Promotion: 18.8.2023

## Kurzzusammenfassung

Christian Markus Dietrich

### High Power Femtosecond Doubly Resonant Optical Parametric Oscillator

Diese Arbeit befasst sich mit dem Design, der Charakterisierung und der Stabilisierung eines leistungsstarken doppeltresonanten optisch parametrischen Oszillators (DROPO), der im Wellenlängenbereich von  $2\ \mu\text{m}$  Femtosekundenpulse emittiert. Das System wird von einem Femtosekunden-Kerr-Linsen-modengekoppelten Yb:YAG-Scheibenlaser gepumpt, mit einer zentralen Wellenlänge von  $1\ \mu\text{m}$ , ca. 20 W Ausgangsleistung und einer Wiederholrate im MHz-Bereich.

Aufgrund der phasenabhängigen Verstärkungsbedingung des nichtlinearen Prozesses ergibt sich ein komplexes spektrales Verhalten des DROPOs, wenn die Resonatorlänge verändert wird. Dieses wird stark von der Resonatordispersion beeinflusst. Das System wird bei unterschiedlichen Parametern in dieser Arbeit experimentell untersucht und mit numerischen Modellen simuliert. DROPOs zeigen periodische Bereiche, bei denen das System emittiert, wenn der Resonator verstimmt wird. Ein Weg, um die Anzahl dieser Resonanzen im entarteten Bereich zu erhöhen, wird in dieser Arbeit vorgestellt und experimentell nachgewiesen. Hierdurch kann die Benutzbarkeit solcher Systeme erhöht werden.

Um den DROPO auf einer dieser Resonanzen zu stabilisieren, werden häufig Stabilisierungsverfahren verwendet, bei denen Systemgrößen mit einer Frequenz moduliert werden. Dieses Verfahren kann zusätzliches Rauschen in der Ausgangsleistung oder im optischen Spektrum erzeugen, welche ggf. Experimente stören kann. In dieser Arbeit wird ein Stabilisierungsansatz ohne Modulation gezeigt, der eine Asymmetrie zwischen einem spektral gefilterten Summenfrequenzsignal und dem DROPO-Signal ausnutzt. Dies ermöglicht die Verwendung eines Proportional-Integral-Regler um eine DROPO-Resonanz auf längeren Zeitskalen zu stabilisieren.

Neben der zeitlichen Stabilität benötigen einige Experimente hohe Spitzelleistungen. Passive Überhöhungsresonatoren sind bekannt für ihre Fähigkeit, diese Leistungen zur Untersuchung von nichtlinearen Prozesse zu erzeugen. Bis zu dieser Arbeit war nicht bekannt, ob in DROPOs solche Überhöhungen auch erreichbar sind. Diese Arbeit zeigt, dass durch die Wahl der richtigen Resonatorparameter eine Überhöhung innerhalb des DROPO Resonators möglich ist. Die experimentellen Ergebnisse werden durch ein semianalytisches Modell ergänzt, welches zeigt, dass die theoretischen Grenzen der maximalen Überhöhung ähnlich eines passiven Überhöhungsresonators sind.

**Schlüsselwörter:** Doppelt resonanter optisch parametrischer Oszillator, nichtlineare Optik, Split-Step Fourier Methode, Verstärkungsresonator, Stabilisierung



## Abstract

Christian Markus Dietrich

### High Power Femtosecond Doubly Resonant Optical Parametric Oscillator

Optical parametric oscillators (OPOs), which rely on an optical parametric amplification in a cavity, can extend the available optical frequency range of common laser sources. In a doubly resonant OPO (DROPO) two optical frequencies resonate in the cavity and with their ability to phase-lock to the pump, tailored multi-color electric fields can be generated. For example, such fields can be used for high harmonic generation or to generate THz radiation with MHz repetition rate.

This thesis focuses on the design, characterization and stabilization of a high power femtosecond doubly resonant optical parametric oscillator (DROPO) that emits in the 2  $\mu\text{m}$  wavelength range. The system is pumped by a femtosecond Kerr-lens mode-locked Yb:YAG thin-disk laser, with a central wavelength around 1  $\mu\text{m}$ , tens of watts of output power and a repetition rate in the MHz range. Due to the phase dependent amplification condition of the nonlinear process, a complex spectral behaviour arises, when the cavity length is detuned. It is strongly influenced by the dispersion in the cavity. The detuning behaviour is experimentally examined in this work and numerical models for its explanation are derived. DROPOs show characteristic on/off switching resonances when the cavity length is detuned. A new way to extend the number of detuning resonances in the degenerated regime is found and experimentally proven. In order to stabilize these systems on one of these resonances dither based schemes are often employed. These schemes induce additional noise in the oscillator which can disturb the experiment. In this work, a dither free approach is chosen which takes advantage of an asymmetry between a spectrally filtered sum frequency signal and the DROPO's signal, when the cavity is detuned. Thus, it allows to use a proportional integral servo controller to stabilize the DROPO resonances for longer time scales. In addition to stability over time, some experiments also require high peak power. Passive enhancement cavities are well known for their ability to confine pulses and generate high peak powers to drive nonlinear processes. Before this work it was unknown if DROPOs can also achieve this enhancement. This thesis answers this question and shows that by choosing the right cavity parameters a strong enhancement is possible. The experimental results are underlined with a semianalytical model which elaborates that the theoretical limits of the maximum enhancement are similar to the passive enhancement cavity ones.

To summarize, in this thesis a DROPO in the 2  $\mu\text{m}$  wavelength range is presented, which will be used for the generation of single cycle THz pulses in the future.

**Key words:** Doubly resonant optical parametric oscillator, nonlinear optics, split-step Fourier method, enhancement cavity, stabilization

# Contents

<b>1</b>	<b>Introduction</b>	<b>1</b>
<b>2</b>	<b>Theoretical aspects</b>	<b>5</b>
2.1	Optical parametric amplification . . . . .	5
2.2	Cavity properties . . . . .	12
2.3	Femtosecond DROPOs . . . . .	15
2.4	Self-phase locking . . . . .	16
2.5	Phase sensitivity of the frequency mixing . . . . .	16
2.6	Numerical simulation of the DROPO . . . . .	18
2.7	Conclusion . . . . .	22
<b>3</b>	<b>Impact of higher-order dispersion coefficients</b>	<b>25</b>
3.1	Experimental setup . . . . .	25
3.2	Spectral tuning behaviour . . . . .	32
3.3	Spatial effects, spectral dependencies on the pump power and crystal phase-matching . . . . .	44
3.4	Conclusion . . . . .	47
<b>4</b>	<b>Resonant enhancement</b>	<b>49</b>
4.1	Introduction . . . . .	49
4.2	Amplitude based model of the nonlinear interaction . . . . .	50
4.3	Experimental setup for enhancement measurements . . . . .	59
4.4	Interplay of the crystal length and pump power . . . . .	61
4.5	Influence of the GDD and TOD on the enhancement . . . . .	65
4.6	DROPO detuning resonance width in dependence of the losses . . . . .	66
4.7	Conclusion . . . . .	68

---

<b>5</b>	<b>Dither free stabilization</b>	<b>71</b>
5.1	Introduction . . . . .	71
5.2	Proportional-integral controller . . . . .	72
5.3	Numerical simulation of sum frequency generation . . . . .	74
5.4	Stabilization setup . . . . .	75
5.5	Experimental characterization of the sum frequency generation . . . . .	79
5.6	Performance of the Stabilization . . . . .	82
5.7	Self-phase locking . . . . .	85
5.8	Conclusion . . . . .	87
<b>6</b>	<b>Summary and outlook</b>	<b>89</b>
	<b>Appendices</b>	<b>93</b>
<b>A</b>	<b>Split-step method based model</b>	<b>95</b>
<b>B</b>	<b>Design of optical and electric elements</b>	<b>111</b>
<b>C</b>	<b>Additional alignment routines and measurements</b>	<b>117</b>
C.1	Alignment procedures . . . . .	118
C.2	Passive Stabilization . . . . .	120
	<b>List of Figures</b>	<b>124</b>
	<b>List of Tables</b>	<b>135</b>
	<b>Bibliography</b>	<b>137</b>
<b>7</b>	<b>Related publications</b>	<b>151</b>
	<b>Acknowledgements</b>	<b>155</b>
<b>8</b>	<b>Curriculum Vitae</b>	<b>157</b>

# Chapter 1

## Introduction

Shortly after the invention of the laser in 1960 [1], the first intensity dependent nonlinear responses of matter were measured [2]. This discovery has led to a new branch of optics, the nonlinear optics. With effects, such as the second harmonic generation (SHG), difference frequency generation (DFG), electro-optical Kerr effect, the optical frequencies from lasers can be converted to new regions with high efficiency [3, 4, 5]. Doubly resonant optical parametric oscillators (DROPOs) are cavity feedback supported optical parametric amplifiers, which are based on the difference frequency generation. They transform one pump photon into two lower energy photons. The one with the larger photon energy is called signal and with the smaller photon energy is called idler.

Their ability to reach new wavelength ranges opens up many new possibilities in science, industry and application. For example, the down-converted light in the mid-infrared range can be used to measure gas absorption with spectroscopy [6, 7]. Pumped by CEP stabilized femtosecond lasers, DROPOs can generate stable frequency combs [8]. With these combs, molecules can be traced with Vernier spectroscopy [9] or they can be deployed as a frequency calibrator for astronomic telescopes [10]. Recent works show that DROPOs can be used for adiabatic quantum computation [11, 12], too. The DROPO presented in this paper will be used to generate and examine so-called Brunel radiation [13], which was the main motivation to build such a system. With the combined light of pump and the DROPO's down-converted light, THz radiation can be generated, which can possibly reveal information about ionization delays of electrons in the future [14, 15, 16].



This project was preceded by many developments of optical parametric oscillators (OPOs) in the last years. The history of these systems started in 1965 when Robert C. Miller and J.A. Giordmaine demonstrated the first OPO [17]. The active field of OPO development delivered many advances, for example, in terms of efficiency and spectral bandwidth. Reliable nonlinear crystals like barium borate (BBO) [18], potassium titanyl phosphate (KTP) [19], quasi-phase-matched materials like periodically-poled lithium niobate (PPLN) [20], or orientation-patterned gallium phosphide (GaP) [21] are well known examples. With the progress of ultrafast lasers and synchronous pumping, OPOs could be pumped with high efficiency and their development was further pushed to new regimes [22]. Moreover, OPOs can mainly be operated in two different states, single and doubly resonant. In 1968 J.E. Bjorkholm demonstrated that parametric oscillation can not only be generated within a cavity where both frequencies (doubly resonant) are trapped, but also with only one resonant color (single resonant) [23]. Due to their ability of continuous frequency tunability, single resonant OPOs nowadays are more prevalent than their doubly resonant counterparts. Several systems have been demonstrated, pumped by ultrashort Ti:Sa systems delivering down to sub-20-fs pulses in the visible and mid-IR wavelength range [24, 25]. Also, broadband tunable noncollinear OPOs were developed, which can be tuned from the visible to the NIR spectral region [26, 27]. In comparison to singly resonant OPOs, DROPOs show a lower pump threshold [28], but due to the parametric amplification condition between signal and idler, a more complex spectral tuning behaviour appears [29]. Studies about the DROPOs quantum statistics were made in the 90s. Here, squeezed states were observed and studied experimentally [30, 31] and theoretically [32, 33]. DROPOs can lock the relative phase of the degenerated signal electric field with respect to the pump wave's phase. This self-phase locking was demonstrated in the cw case in 1990 and for femtosecond lasers in 2010 [34, 8]. Stable subharmonic frequency combs [35, 36] can be generated by femtosecond DROPOs, which can also be used for trace molecular detection [37], spectroscopy [38], and for the generation of quantum networks and clusters [39, 40]. Moreover, back and forth conversion dynamics between pump and signal/idler wavelengths in the nonlinear medium can be used to generate solitons in the cavity. This in return allows influencing the temporal shape of the signal pulses by maintaining their coherence with the pump [41, 42]. This thesis complements the DROPO achievements mentioned above. The main goal is to demonstrate the first Yb:YAG thin-disk pumped DROPO in the 2  $\mu\text{m}$  regime,

---

which can handle the high average powers and pulse durations around 250 – 350 fs of such systems. It is built for the generation of asymmetric electric fields, which can be used for Brunel radiation experiments in the future. The DROPO's output spectrum depends among others on the higher-order dispersion terms introduced into the system. This behaviour is explained in detail with experiments and a theoretical model in this thesis. A method to increase the cavity detuning length of the self-phase locking regime is presented. Furthermore, in order to realize intracavity experiments, which take advantage of strong resonating fields, a high enhancement is required. This thesis shows ways to increase the intracavity fields, with a focus on low output coupling. Easy access to the temporal dynamics in the nonlinear crystal is given by equations, solved by an analytical solution. Another problem to be solved is to demonstrate a stabilization scheme for this system. DROPOs show discrete resonances, when the cavity is detuned. To stabilize the system on one resonance, often dither locking schemes are used, which have the disadvantage that they can induce additional noise into the system [43]. A dither-free method is presented, motivated by [44], with the main focus on stability and daily use. The covered topics should help future scientists to understand and build DROPOs more rapidly, but also to pave the way for new concepts of doubly and singly resonant OPOs.

## Structural summary

This thesis is structured in the following way: in Chapter 2 basic equations of the linear and nonlinear effects are given. Moreover, the theoretical treatment of short pulses in dispersive media is shown and the coupled differential equations of the DFG process are explained in detail. Special features of femtosecond pumped DROPOs are described. Then, the theoretical basics of a split-step based model for the DROPO dynamics are presented. In Chapter 3 the experimental setup and the used system parameters are described. The measured influence of the higher-order dispersion terms is compared with the numerical model. In Chapter 4 the main subject is the intracavity enhancement of the DROPO's signal and idler. A semianalytical model is introduced, which is then benchmarked with experimental values. Moreover, influences of pump power and output coupling on the detuning resonance width are presented. Then, a dither-free stabilization scheme is detailed in the last chapter of the experimental results. Measurements of the optical feedback function are shown, ending with the

performance of the stabilized system. At last, the whole thesis is summed up and an outlook for future experiments is given.

# Chapter 2

## Theoretical aspects

In this chapter, the concept of the underlying physical effects of a femtosecond DROPO is explained. At first, the optical parametric amplification will be explained. The theoretical background of an OPO will be discussed and the phase-matching condition in the crystal and the cavity will be derived. The difference between a cw-DROPO and femtosecond DROPO is discussed and the self-phase locking phenomenon is shown. At last, a numerical model for the DROPO is presented, which is compared with experimental results in Chapter 3.

### 2.1 Optical parametric amplification

The heart of an OPO is the optical parametric amplification process, which is described in this section. When an electric field  $E$  propagates through a material, the material's polarization  $P$  can be written as a power series [5]:

$$P = \epsilon_0 \chi^{(1)} E + \epsilon_0 \chi^{(2)} E^2 + \epsilon_0 \chi^{(3)} E^3 + \text{h.o.t.}, \quad (2.1)$$

where  $\chi^{(i)}$  is the  $i$ -th expansion order of the electric susceptibility and  $\epsilon_0$  the vacuum permittivity. For a, in relation to the atom's field, weak electric field the polarization is linear. For a strong field, higher-order terms need to be taken into account. For parametric amplification, the second-order term is important. With a superposition of two scalar electric fields with the angular frequencies  $\omega_1$  and  $\omega_2$ :

$$E = E_1 \exp[i(-\omega_1 t)] + E_2 \exp[i(-\omega_2 t)] + \text{c.c.}, \quad (2.2)$$

neglecting the propagation term  $kz$  and the spectral phase  $\varphi$ , where  $\omega_1 > \omega_2$ , the second order polarization term  $P^{(2)}$  in Eq. (2.1) can be rewritten to [5]:

$$P^{(2)} = \epsilon_0 \chi^{(2)} \begin{bmatrix} E_1^2 \exp[2i\omega_1 t] & \text{Second harmonic of } \omega_1 \\ + E_2^2 \exp[2i\omega_2 t] & \text{Second harmonic of } \omega_2 \\ + 2(E_1^2 + E_2^2) & \text{Optically rectification} \\ + E_1 E_2 \exp[i(\omega_1 + \omega_2)t] & \text{Sum frequency} \\ + E_1 E_2 \exp[i(\omega_1 - \omega_2)t] & \text{Difference frequency} \end{bmatrix}. \quad (2.3)$$

The resulting polarization contains various mixing products of the incident light fields, such as the second harmonic generation (SHG), sum frequency generation (SFG) and difference frequency generation (DFG). With optical rectification, THz radiation can be generated [45, 46, 47].

The second order susceptibility can be described by a contracted tensor  $d_{ij}$ , after considering different symmetries of the nonlinear medium [3]. As most of the indices of the tensorial susceptibility or the electric field are zero, the tensorial susceptibility can be further reduced to the scalar valued effective susceptibility  $d_{\text{eff}}$ . The scalar susceptibility can be calculated for a combination of crystal geometry and incident field polarizations.

In DROPOs, the used nonlinear effect is the DFG, but also parasitic SFG and SHG occur. In these systems, a pump field  $E_1(\omega_1)$  is converted into two different fields  $E_2(\omega_2)$  and  $E_3(\omega_3)$  with  $\omega_1 \geq \omega_2 \geq \omega_3$ . An efficient frequency mixing happens, if the energy conservation is fulfilled:

$$\hbar\omega_1 = \hbar\omega_2 + \hbar\omega_3 \quad (2.4)$$

and the phase-mismatch  $\Delta k$  in the crystal is zero:

$$\Delta k = k_2 + k_3 - k_1 = 0, \quad (2.5)$$

where  $k = \omega n(\omega)/c$ . In Fig. 2.1 the energy conversion of the DFG and SFG process and the phase-mismatching is schematically illustrated. In Fig. 2.1 (a) the DFG process is shown in an energy level diagram. The dotted lines denote virtual levels of the atom, which interact with the incoming pump photon  $\omega_1$ . It is split in two new photons with

the frequencies  $\omega_2$  and  $\omega_3$ , respectively. In Fig. 2.1 (b) the sum frequency process is shown. Here, two photons are combined to one photon. In Fig. 2.1 (c), the phase-mismatch is presented. For optimal generation, the sum of  $k(\omega_2)$  and  $k(\omega_3)$  needs to be equal to  $k(\omega_1)$ , which means  $\Delta k = 0$ , otherwise it will not lead to an efficient frequency mixing.

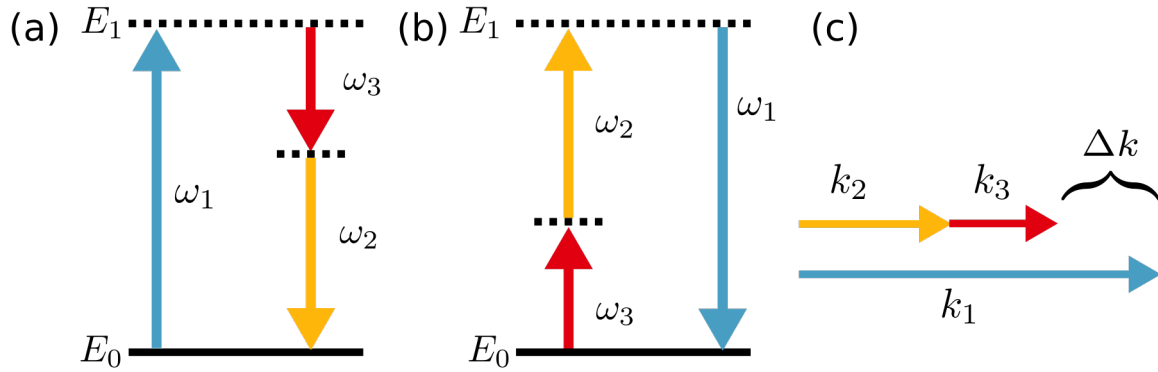


Figure 2.1: Energy conservation and phase-matching in a nonlinear crystal. The energy level  $E_0$  is the ground state, while the dotted lines denote virtual levels. (a) Down-conversion process: a frequency  $\omega_1$  is split up in two frequencies with lower energy. (b) Sum frequency process: the inverse of the down-conversion process. (c) Phase-matching: the interacting frequencies have different wave numbers  $k_{1,2,3}$ , due to their frequencies and refractive indices. The phase mismatch  $\Delta k$  needs to be zero for efficient frequency mixing.

## Birefringent crystal phase-matching

The refractive index in materials depends on the frequency of the electric field, normally  $n(\omega_1) > n(\omega_2) > n(\omega_3)$ , so that in general  $\Delta k \neq 0$ . To realize the phase-matching between two interacting fields, birefringent crystal phase-matching is used [48, 49, 3]. The DROPO, presented in this thesis, is operated with a birefringent beta barium borate (BBO) crystal. The refractive indices of this crystal are dependent on its orientation with respect to the light field. BBO is an uniaxial crystal so that two axis of the linear susceptibility tensor are equal. Two different refractive indices can be used, the ordinary  $n_o$  and extraordinary  $n_e$ . They can be addressed with two orthogonal linear polarizations called (e)xttraordinary and (o)rdinary. The

type I process:

$$e \rightarrow o + o \quad (2.6)$$

is chosen, where the pump is e and signal and idler are o polarized. The refractive index of the pump  $n_\theta(\theta)$  can be tuned by the angle  $\theta$  between the crystal axis and the wave vector, which can be calculated by [3]:

$$\frac{1}{n_\theta(\theta)^2} = \frac{\cos^2 \theta}{n_o^2} + \frac{\sin^2 \theta}{n_e^2}. \quad (2.7)$$

For some angles  $\theta$  the phase mismatch is zero, which can be found, for the DFG process in the collinear case, by solving the following equation:

$$n_{\omega_1}(\theta) = \frac{n_o(\omega_2) + n_o(\omega_3)}{2}. \quad (2.8)$$

In the degenerated case ( $\omega_3 = \omega_2$ ),  $n_o(\omega_2)$  and  $n_o(\omega_3)$  are equal.

## Phase-matching bandwidth and other limiting factors

The previous considerations are only true for monochromatic fields of fixed wavelengths. As OPOs allow tuning the wavelengths and short pulses can not be approximated by monochromatic spectra, the limitations of the phase-matching bandwidth have to be considered, resulting in a decreased efficiency of the optical process. It can be calculated by [3, 5]:

$$\eta = \text{sinc}^2 \left( \frac{\Delta k L_c}{2} \right). \quad (2.9)$$

The mismatch factor can be determined for different phase-matching angles  $\theta$  and different down-converted frequencies. Depending on the crystal length  $L_c$ , the maximum phase-matching bandwidth and angular acceptance can be predicted [5].

Additional to  $\eta$ , other effects can limit the conversion efficiency. To determine the crystal length corresponding to the highest conversion efficiency, effects like the walk-off angle and the group velocity mismatch need to be taken into account. The walk-off

angle  $\rho$  between the pump and the signal/idler beam is defined by [5]:

$$\rho = \tan^{-1} \left( \frac{n_o^2}{n_e^2} \tan \theta \right) - \theta. \quad (2.10)$$

Depending on the waist size of the beams, the maximum length of the spatial overlap between the fundamental and down-converted beam can be calculated by  $\rho$ .

The different group velocities of the beams in the crystal also influence the maximum length of the crystal, where the pulses temporarily overlap. This temporal walk-off can be approximated by [50]:

$$L_{c,\max} = \tau_p \left( \frac{1}{v_{s,i}} - \frac{1}{v_p} \right)^{-1}, \quad (2.11)$$

where

$$v_{p,s,i} = \left( \frac{\partial \phi(\omega)}{\partial \omega} \Big|_{\omega_{p,s,i}} \right)^{-1} \quad (2.12)$$

is the group velocity of pump, signal or idler and  $\tau_p$  is the pump pulse duration.

## Coupled propagation equations

Electric fields can be described by a complex amplitude  $A(z, t)$  and a carrier wave with its central frequency  $\omega_0$  of the optical spectrum. The complex electric field  $E(z, t)$  can be described as [51, 52]:

$$E(z, t) = A(z, t)e^{i(\omega_0 t - k_0 z)} + \text{c.c.}, \quad (2.13)$$

with the time  $t$ , the propagation distance  $z$ , the central frequency of the optical spectrum  $\omega_0$ , the central wave number  $k_0 = \omega_0 n(\omega_0)/c$ , the speed of light in vacuum  $c$  and the refractive index  $n(\omega_0)$ . Here, the electric field is treated in one spatial dimension.

The dynamics of the three interacting electric fields in the nonlinear crystal can be complex. To derive the coupled differential equations for the down-conversion process, several simplifications of the system are used. Here, an isotropic, homogeneous, lossless and nonmagnetic nonlinear medium with a weak birefringence is assumed. These



properties match those of the BBO crystal in the experiment. Linearly polarized light fields and the slowly varying envelope approximation are taken into account [5]. For the down-conversion case the following three coupled differential equations for the interacting waves of the DFG process can be found [5]:

$$\frac{dA_i}{dz} = i \frac{\omega_i}{n_i c} d_{\text{eff}} A_p A_s^* e^{i\Delta k z}, \quad (2.14)$$

$$\frac{dA_s}{dz} = i \frac{\omega_s}{n_s c} d_{\text{eff}} A_p A_i^* e^{i\Delta k z}, \quad (2.15)$$

$$\frac{dA_p}{dz} = i \frac{\omega_p}{n_p c} d_{\text{eff}} A_s A_i e^{-i\Delta k z}, \quad (2.16)$$

with the complex field amplitudes  $A_{p,s,i}$  of pump, signal, idler and the corresponding refractive indices  $n_{p,s,i}$ . Every equation describes a specific type of conversion:

- Equation (2.14) describes the difference frequency generation of the pump and the signal wave to generate or deplete the idler wave
- Equation (2.15) describes the difference frequency generation of the pump and the idler wave to generate or deplete the signal wave
- Equation (2.16) describes the sum frequency generation of the signal and the idler wave to generate or deplete the pump wave

Equation (2.16) shows that signal and idler can be back converted to the pump, which is fully phase-matched, too. In Chapter 4, a detailed theoretical and experimental analysis of the back conversion effect and its influence on the performance of the oscillator is given.

The parametric process is a phase dependent process. One can define the relative phase relationship between the three interacting fields as [53]:

$$\gamma = \phi_s + \phi_i - \phi_p - \Delta k z, \quad (2.17)$$

where  $\phi_{p,s,i}$  are the corresponding relative phases of the electric fields and  $z$  is the propagation in the nonlinear crystal. The equations (2.14) - (2.16) have an analytic solution in the plane wave approximation. The solution is very comprehensive and can be found in [5, 53]. In Fig. 2.2, examples are illustrated for different  $\gamma$ .

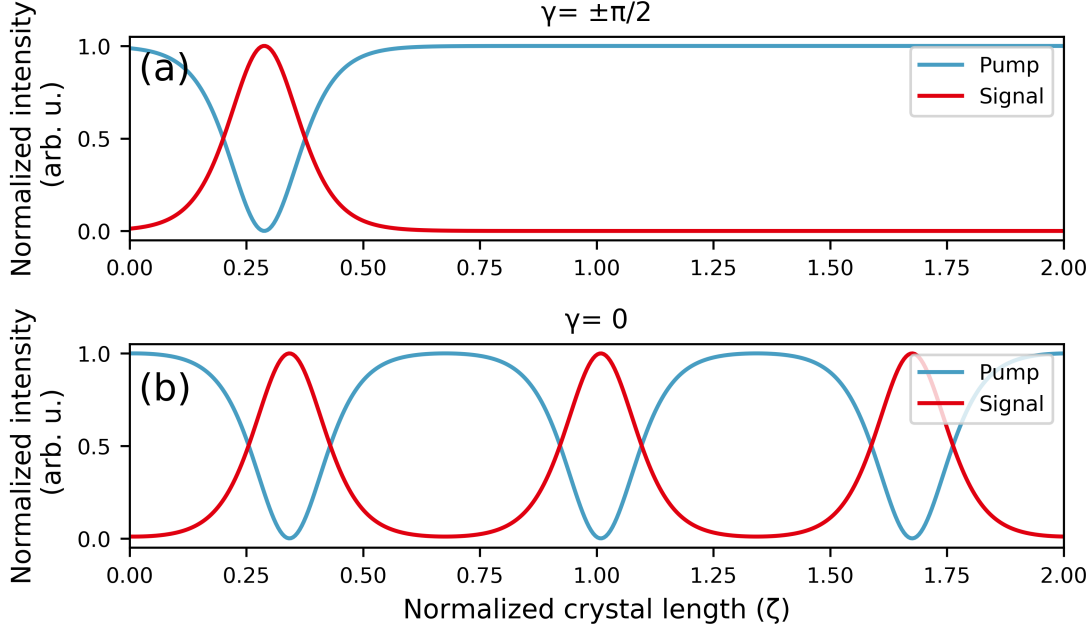


Figure 2.2: Examples of the analytic solution of equations (2.14) - (2.16) at degeneracy. The expected conversion of the pump (blue) to the signal wave (red) and the back conversion is displayed. (a) For  $\gamma = \pm\pi/2$ , the solution shows only one cycle of nonlinear interaction. (b) When  $\gamma$  is unequal to  $\pm\pi/2$ , oscillation occurs in the crystal. Because of this sensitivity on the phase and input power, in a realistic OPO, virtually no stable output power is possible.

On the x-axis the normalized crystal length  $\zeta = d_{\text{eff}} \sqrt{2I\omega_p\omega_s\omega_i / (\epsilon_0 c^3 n_p n_s n_i)} z$  with the combined intensity  $I$  of pump, signal and idler is presented. Here,  $\Delta k$  is set to zero and the down-converted frequencies are degenerated ( $\omega_s = \omega_i$ ). Losses of the crystal are neglected. In Fig. 2.2 (a), one can see that for  $\gamma = \pm\pi/2$  the pump intensity has a single conversion cycle to signal and then back to its initial intensity. In the case of  $\gamma \neq \pm\pi/2$  like in Fig. 2.2 (b) the solution shows several oscillations within the crystal, which can differ in frequency in dependence of the incoming amplitudes of the electric field. Here, efficient and stable frequency mixing is difficult. In conclusion, for  $\Delta k = 0$ , amplification can be obtained for  $\gamma = \pm\pi/2$  leading to the transformation of Eq. (2.17) into:

$$\phi_p = \phi_s + \phi_i \pm \frac{\pi}{2}. \quad (2.18)$$

## 2.2 Cavity properties

The optical parametric down-conversion is used in different regimes. For amplifier systems with several MHz repetition rate and several  $\mu\text{J}$  of pump pulse energy, optical parametric amplifiers rely on a weak signal, the seed, being amplified by a highly energetic pump beam, often in a single pass geometry [52].

With most laser oscillators, which have repetition rates of several tens of MHz and pulse energies typically  $< 1 \mu\text{J}$ , high efficiencies cannot be reached in a single pass optical parametric amplifier (OPA). To generate high efficiencies a cavity around the nonlinear crystal is built. It allows to build up the signal/idler fields with small gain in many round trips. The cavity supported amplification is called optical parametric oscillator. In the following, the influence of the cavity on the nonlinear process is discussed.

### Longitudinal modes

An optical cavity allows, similar to a Fabry-Pérot interferometer, only specific longitudinal modes to propagate inside the cavity. The intensity of the modes  $I_{\text{long}}$  can be approximately<sup>1</sup> described by [55, 56]:

$$I_{\text{long}}(\omega) \propto \frac{1}{1 + F \sin^2 k(\omega)L_c}, \quad (2.19)$$

where  $L_c$  is the cavity length,  $k$  the wave number and  $F$  is the finesse, defined by the combined amplitude reflectance of all mirrors  $r$  [55]:

$$F = \frac{\pi r}{1 - r^2}. \quad (2.20)$$

The longitudinal modes form a comb in the frequency range. The width of each comb peak is determined by the finesse. The free spectral range (FSR) describes the spacing between the maxima [55]:

$$\text{FSR} = \frac{c}{2L_c}. \quad (2.21)$$

---

<sup>1</sup>The following discussion assumes, for better understanding, that the cavity is passive. A more precise description would be possible with the Schawlow-Townes limit [54], where the linewidth of the optical system is described by the spectral bandwidth of the oscillator and the output power.

Ultrashort lasers with broad spectra can have hundreds of thousands of generated longitudinal modes, depending on their repetition rate and spectral bandwidth. The maximum in frequency space of Eq. (2.19) can be calculated by [55]:

$$k(\omega)L_c = q\pi \Leftrightarrow q\frac{\pi c}{\omega} = L_c, \quad q \in \mathbb{N}. \quad (2.22)$$

It can be seen that the frequency of the maximum can be altered, if the cavity length is changed. In a DROPO, signal and idler need to be simultaneously in resonance in the cavity. In general  $k_s$  and  $k_i$  are not equal, so in most cases a frequency pair is only partly resonant for a given cavity length  $L_c$ . When  $L_c$  is altered, the position of the resonances is changing described by Eq. (2.22). For specific lengths, matched cases of signal and idler can be found. In Fig. 2.3 this situation is shown for a continuous wave (cw-)DROPO at non-degeneracy. Equation (2.19) is shown for a chosen signal and idler frequency for different cavity lengths. The cw-DROPO displays resonances in the output power when the cavity length is altered. The highest possible output power corresponds to a perfect superposition between the signal and idler mode structure. The width of the resonances of the cw-DROPO is affected by the finesse of signal and idler  $F_s$  and  $F_i$ . Here, the maximum detuning of the length of one combined mode can be calculated by [57]:

$$\Delta\nu_{\max} = \Delta\nu_s + \Delta\nu_i = \frac{\text{FSR}_s}{2F_s} + \frac{\text{FSR}_i}{2F_i}, \quad (2.23)$$

where  $2\Delta\nu_{s,i}$  is the full width at half maximum (FWHM) of the corresponding resonance,  $\text{FSR}_{s,i}$  the free spectral range for signal and idler. Higher finesse reduces the likelihood of overlap between signal and idler modes. For the generation of down-converted light, the cw-DROPO needs to fulfill energy conservation, phase-matching and two resonance conditions. To continuously tune the frequency of a cw-DROPO, the pump frequency, the phase-matching and the length of the DROPO need to be adapted simultaneously [58, 59]. Because of this, cw-DROPOs are more difficult to control and stabilize than their single resonant counterpart.

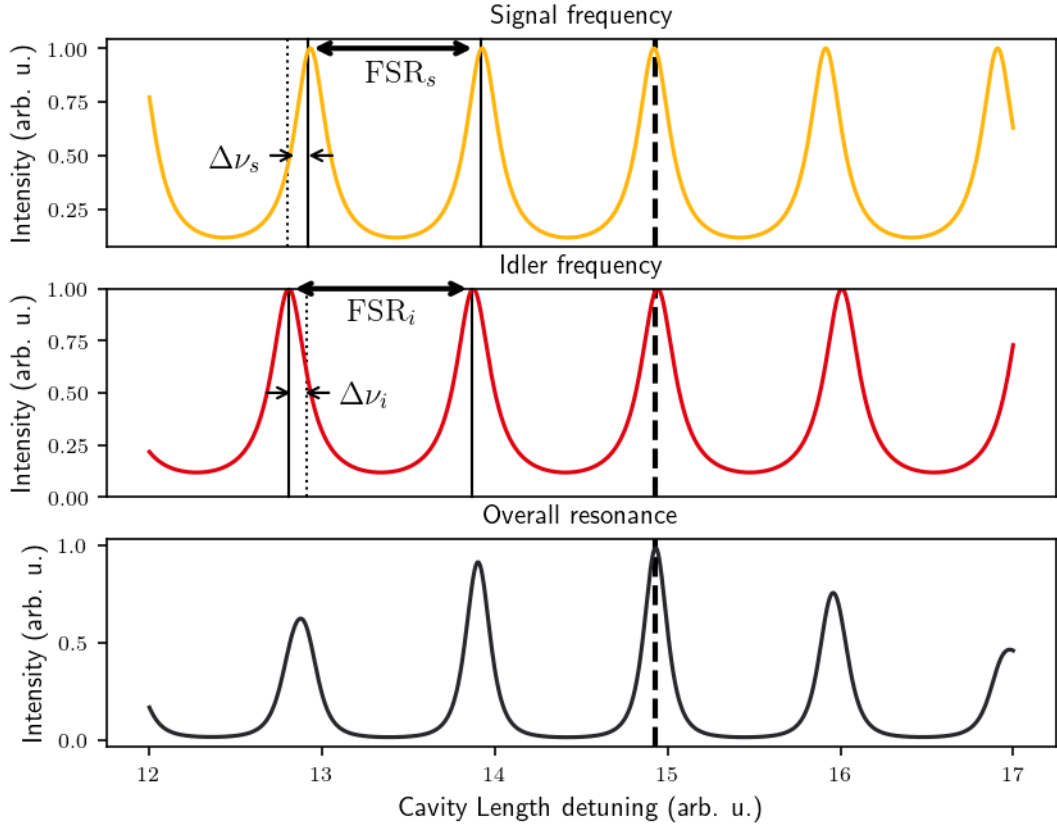


Figure 2.3: Longitudinal modes of a cw-DROPO. Signal (yellow) and idler (red) modes need to be simultaneously resonant in the cavity. In the top and middle panel, the signal and idler longitudinal modes are illustrated. Additionally, their free spectral range and the FWHM of the corresponding resonance  $\Delta\nu_{s,i}$  are shown. Their multiplied function defines the DROPO frequency modes and the possible performance at that working point. Depending on the finesse and the pump laser frequency, the signal and idler modes need to coincide well in the cavity (dotted lines), for efficient conversion.

## 2.3 Femtosecond DROPOs

The concept of the cw-DROPO needs to be extended for femtosecond DROPOs. First considerations with multi-mode systems are shown in [60]. The publication describes that the DROPO threshold is the same as in cw-operation. In Fig. 2.4, a schematic concept is presented how a non-degenerated femtosecond DROPO is working [8]. Since the pump modes have an exact spacing defined by the FSR, they can split in different

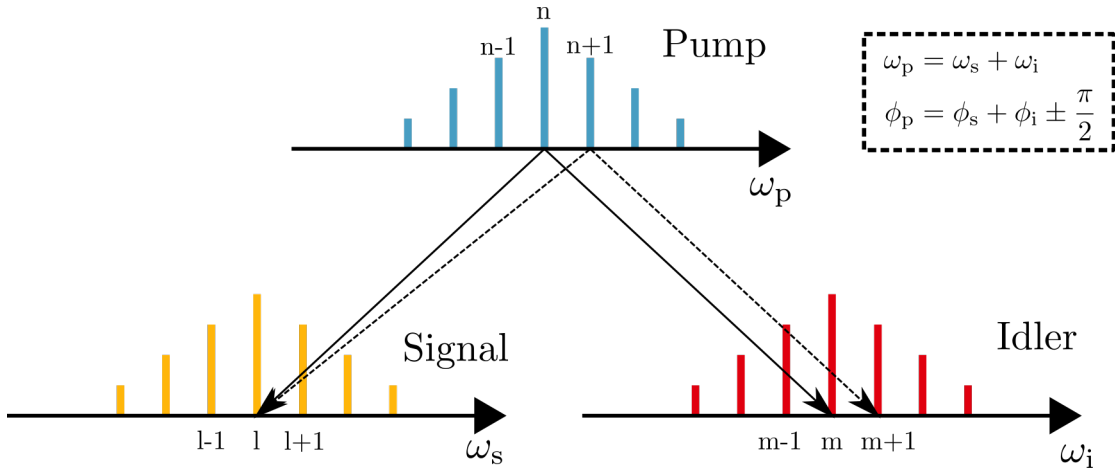


Figure 2.4: Crosstalking of modes in a DROPO. For example the  $n^{\text{th}}$  and  $n^{\text{th}} + 1$  pump mode of a mode-locked laser can both split in the  $l^{\text{th}}$  signal mode and separate in the  $m^{\text{th}}$  and  $m^{\text{th}} + 1$  idler mode to fulfil the energy conservation. With the amplification phase condition Eq. (2.18), a phase relation between the pump, signal and idler is made.

combinations of signal and idler modes, like for example, the  $n^{\text{th}}$  pump mode in the  $l^{\text{th}}$  and  $m^{\text{th}}$  signal/idler mode. It is possible that the same pump mode gets down-converted to the  $l^{\text{th}} + 1$  and  $l^{\text{th}} - 1$  mode for example, as long as it fulfils the energy conservation (Eq. (2.4)). As shown in Fig. 2.4, two pump modes  $n$  and  $n + 1$  can convert also in one signal mode  $l$ . The energy conservation needs to be fulfilled also here, so the resulting idler modes have to be  $m$  and  $m+1$ . Since the amplification phase condition (Eq. (2.18)) is valid and a mode-locked laser has a fixed phase relationship between its modes, the phase of the  $m$  and  $m+1$  mode needs to be the same with  $\phi_m = \phi_n - \phi_l = \phi_{n+1} - \phi_l = \phi_{m+1}$ . With this mechanism a crosstalk between the signal/idler modes is established, which locks their phase to each other [8]. Femtosecond DROPOs show also in the non-degenerated case, moderate power stability [61]. In

comparison to cw-DROPOs, many pump modes can contribute to one signal or idler mode. The DROPO selects efficient combinations of pump and signal/idler modes, so that simultaneously resonance (see Fig. 2.3) for every signal/idler longitudinal mode is maintained.

## 2.4 Self-phase locking

When a cw-DROPO is running at the degeneracy point ( $\omega_s = \omega_i$ ), signal and idler are indistinguishable. Equation (2.18) can be simplified to

$$\phi_p = 2\phi_s \pm \frac{\pi}{2}. \quad (2.24)$$

In comparison to the non-degenerated state, where the phases of signal and idler combs can adapt freely, the relative phase of the degenerated signal is locked to the pump ones. The phase stability between pump and signal is mentioned in literature as the self-phase locking effect of a DROPO and observed in several systems [34, 8, 62]. The locking mechanism can be seen as similar to the injection-locking of two laser, where in the DROPO case signal and idler lock each other [63, 64]. The resulting coherence properties to the pump are necessary for the generation of multi-color fields to generate THz radiation, which is one of the motivations of this thesis.

For a femtosecond DROPO the concept of self-phase locking needs to be extended [8, 61]. To understand the self phase locking in a femtosecond DROPO Fig. 2.4 can be used. In the non-degenerated state the crosstalk between the modes locks the phases of neighbouring signal (and idler) modes. When the DROPO is tuned to degeneracy the signal and idler modes begin to overlap. The neighbouring signal and idler modes can now establish a stable phase relationship to all modes, which lead to the locking of the signal phase to the pump. In general, the degenerated resonances of the femtosecond DROPO are self-phase locked, however possibly intermediate degenerated resonances are not locked, which are presented in Chapter 3.

## 2.5 Phase sensitivity of the frequency mixing

DROPOs show a periodic on/off switching in power, when the cavity length is tuned [65, 61]. This discrete resonances depend on the amplification phase condition (Eq. (2.18))

and are further discussed in Chapter 3. The width of the resonances is for typical setups several tens of nanometer and depends on the pump power and cavity finesse. The following theoretical discussion is adopted from the publication [8]. The presented formalism can be used to calculate the maximum possible phase mismatch of signal/idler per roundtrip  $\Delta\phi = \phi_p - \phi_s - \phi_i \mp \pi/2$ . For the calculation of the roundtrip phase mismatch, a matrix formalism of the DROPO is chosen [8, 66]:

$$\begin{pmatrix} A_s(z = L_c) \\ A_i^*(z = L_c) \end{pmatrix} = \mathbf{M} \begin{pmatrix} A_s(z = 0) \\ A_i^*(z = 0) \end{pmatrix}, \quad (2.25)$$

$$(2.26)$$

$$\mathbf{M} = \begin{pmatrix} r & 0 \\ 0 & r \end{pmatrix} \begin{pmatrix} e^{i\Delta\phi} & 0 \\ 0 & e^{i\Delta\phi} \end{pmatrix} \begin{pmatrix} \cosh(gL_c) & i \sinh(gL_c) \\ -i \sinh(gL_c) & \cosh(gL_c) \end{pmatrix}. \quad (2.27)$$

$A_s$  and  $A_i$  describe the normalized signal and idler fields. The matrix  $\mathbf{M}$  is used to describe the transformation of the two fields after one roundtrip. The first matrix (from left) of  $\mathbf{M}$  induces the cavity losses  $\alpha$  with  $r^2 = 1 - \alpha$ , where  $r$  is the amplitude reflectivity of the cavity. The second matrix adds the phase mismatch to the equation. The third matrix contains with the gain  $g$  the solution of the DFG equations [66]. The equations are solved with a small signal/idler approximation without pump depletion. If the oscillator runs in the steady state regime, the field vector replicates itself after the multiplication with  $\mathbf{M}$ . The determinant of  $\mathbf{M} - \mathbf{I}$ , where  $\mathbf{I}$  is the identity matrix, gives the gain/loss balance of the system [8]:

$$(gL_c)^2 = \alpha^2/4 + \Delta\phi^2. \quad (2.28)$$

It can be directly seen that a non-zero phase mismatch can be compensated by increasing the gain, i.e. stronger pump pulses. The equation can be therefore transformed into [8]:

$$\Delta\phi = \frac{\alpha}{2} \sqrt{r_p - 1}, \quad (2.29)$$

with  $r_p = (gL_c)^2/(gL_c)_0^2$  being the pump parameter, where  $(gL_c)_0^2 = (\alpha/2)^2$  is the DROPO threshold [8]. To calculate the maximum theoretical cavity detuning length  $\Delta L$  of a DROPO, the relation

$$\frac{\Delta\phi}{2\pi} = \frac{\Delta L}{\lambda_s/2} \quad (2.30)$$



can be used, where  $\lambda_s$  is the signal wavelength at degeneracy. The resulting equation is

$$\Delta L = \frac{\lambda_s \alpha}{4\pi} \sqrt{r_p - 1}. \quad (2.31)$$

It should be noted that a factor of two is added, to cover the width of a DROPO resonance on both sides. In Chapter 4, experimental measurements of the resonance width are presented.

## 2.6 Numerical simulation of the DROPO

In order to investigate the spectral and temporal dynamics of a femtosecond DROPO, numerical simulations are performed. The results are compared in Chapter 3 and 4 with the experimental results.

### Short optical pulses and dispersive media

Mode-locked pulses can be described by Eq. (2.13). With the Fourier transform  $\mathfrak{F}(f(t)) = \int_{-\infty}^{\infty} f(t)e^{-i\omega t} dt$ , the electric field in the frequency domain  $\tilde{E}(\omega)$ , with the spectral phase  $\varphi$ , can be calculated [52]:

$$\tilde{E}(z, \omega) = \mathfrak{F}(E(z, t)) = |\tilde{E}(z, \omega)|e^{i\varphi(\omega)} + \text{c.c.} \quad (2.32)$$

When the electric field propagate in a dispersive medium, a spectral phase  $\phi$  is added:

$$\phi(\omega) = k(\omega)z = \frac{\omega n(\omega)}{c} L_{\text{mat}}, \quad (2.33)$$

with the refractive index  $n(\omega)$  and a given material length  $L_{\text{mat}}$ . The phase can be expanded in a Taylor series:

$$\begin{aligned} \phi(\omega) = \phi(\omega_0) &+ \left. \frac{\partial \phi(\omega)}{\partial \omega} \right|_{\omega_0} (\omega - \omega_0) + \frac{1}{2} \left. \frac{\partial^2 \phi(\omega)}{\partial \omega^2} \right|_{\omega_0} (\omega - \omega_0)^2 \\ &+ \frac{1}{6} \left. \frac{\partial^3 \phi(\omega)}{\partial \omega^3} \right|_{\omega_0} (\omega - \omega_0)^3 + \text{h.o.t.} \end{aligned} \quad (2.34)$$

The derivatives are defined as the following:

$$\left. \frac{\partial \phi(\omega)}{\partial \omega} \right|_{\omega_0} = \text{group delay (GD)} \quad (2.35)$$

$$\left. \frac{\partial^2 \phi(\omega)}{\partial \omega^2} \right|_{\omega_0} = \text{group delay dispersion (GDD)} \quad (2.36)$$

$$\left. \frac{\partial^3 \phi(\omega)}{\partial \omega^3} \right|_{\omega_0} = \text{third-order dispersion (TOD)}. \quad (2.37)$$

Since different optical materials are used in DROPO cavities, the derivatives can play a role. In Chapter 3 the impact of this terms on the spectral behaviour of the DROPO, when the cavity length is detuned, is closer discussed.

## Numerical model

The three coupled equations (2.14) - (2.16) for the DFG process perform well in the cw-case. However, in pulsed applications the frequency bands of signal and idler can overlap and the influence of the material dispersion must be taken into account. By joining signal and idler in a single waveform, the following two equations can be used [67, 68, 69]:

$$\frac{\partial A_{s,i}(t, z)}{\partial z} = \hat{\beta}_{s,i} A_{s,i}(t, z) - i\kappa A_p(t, z) A_{s,i}^*(t, z), \quad (2.38)$$

$$\frac{\partial A_p(t, z)}{\partial z} = \hat{\beta}_p A_p(t, z) - i\kappa A_{s,i}(t, z) A_{s,i}(t, z). \quad (2.39)$$

Here, the ordinary polarized signal and idler fields are superimposed to one amplitude  $A_{s,i}$ . The change of the extraordinary pump field  $A_p$  is defined by the second equation. The influence of the dispersion is described with the first term on the right-hand side and the nonlinear interaction is described with the second term. The equations can be derived from a reduced 1+1D Maxwell equation, which is discussed in detail in [70] and [71].

The dispersion in the crystal is described by the operators  $\hat{\beta}_{s,i} = \mathfrak{F}^{-1} \beta_{s,i} \mathfrak{F}$  and  $\hat{\beta}_p = \mathfrak{F}^{-1} \beta_p \mathfrak{F}$ , with  $\beta_{s,i} = n_s(\omega) \omega / c$  and  $\beta_p = n_\theta(\omega, \theta) \omega / c$ . The refractive indices  $n_p = n_\theta(\omega, \theta)$  and  $n_s$  are calculated with the Sellmeier coefficients from [72] and Eq. (2.7). The nonlinear interaction parameter is defined as  $\kappa = d_{\text{eff}} \omega_p / (2cn_p)$ .

The equations are solved via a 1D split-step method [73]. In Fig. 2.5, the basic structure of the model of the DROPO is shown. Signal and idler are amplified by a strong pump pulse in the nonlinear crystal. The nonlinear part of the differential equations is solved in time with the Euler method and the dispersion of the crystal is added in the spectral domain. The propagation of the waves through the crystal is calculated for small crystal increments  $dz$ . The dispersion and nonlinearity are calculated alternately. Behind the crystal, the losses of the mirrors, the cavity and the output coupling is considered. The spectral phases of all dispersive elements and the detuning of the cavity is included before the next amplification process. The model converges to a steady state after a few hundred roundtrips.

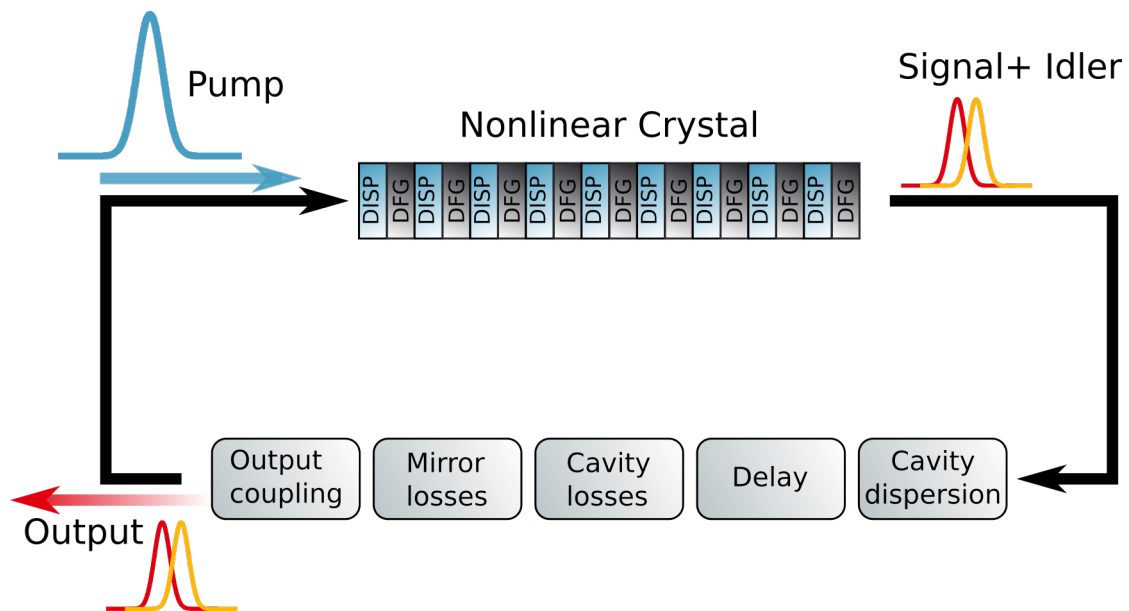


Figure 2.5: Scheme of the numerical model. The differential equations are solved by the split-step method. The nonlinear part is solved in the time and the impact of dispersion is calculated in the spectral domain. To complete the roundtrip, the cavity dispersion (without crystal), losses, the time and phase delays are included. Also, the high reflectivity (HR) mirrors are simulated to have optimal conditions at the borders of the high reflective wavelength region. Approximately 300 roundtrips are necessary to reach the steady state. At the end, the outcoupled power is calculated.

To calculate one roundtrip in the simulated DROPO the following steps are done:

- The simulation of roundtrip  $q$  begins with a  $\text{sech}^2$ -shaped pump pulse with a

complex amplitude  $A_p$  and a non-zero  $A_{s,i}$  as a seed for the simulation.

- The nonlinearity is calculated in the time domain with the Euler method:

$$A'_{s,i}(t, j dz) = A_{s,i}(t, j dz) - i\kappa dz A_p(t, j dz) \cdot A_{s,i}(t, j dz) \quad (2.40)$$

$$A'_p(t, j dz) = A_p(t, j dz) - i\kappa dz A_{s,i}^2(t, j dz), \quad (2.41)$$

where  $dz$  is the spatial increment in the crystal. The index  $j \in 1, 2, \dots, N$  is the propagation index for the increments in the crystal.

- The fields are Fourier transformed to the frequency domain and the dispersion of the crystal is added:

$$A_{s,i}(t, (j+1)dz) = \mathfrak{F}^{-1} [\mathfrak{F} [A'_{s,i}(t, j dz)] e^{i\beta_{s,i} dz}] \quad (2.42)$$

$$A_p(t, (j+1)dz) = \mathfrak{F}^{-1} [\mathfrak{F} [A'_p(t, j dz)] e^{i\beta_p dz}] \quad (2.43)$$

After  $N$  steps, the interaction in the crystal is fully simulated. For the losses, group delay and dispersion (up to the third order) of the cavity, a function is defined [67]:

$$D(\omega) = i\alpha(\omega) + \text{GD}_r(\omega - \omega_0) + \text{GDD}_r(\omega - \omega_0)^2/2 + \text{TOD}_r(\omega - \omega_0)^3/6. \quad (2.44)$$

The parameter  $\alpha$  includes the losses of the output coupler (OC)  $\alpha_{\text{OC}}$ , of the mirrors and additional losses  $\alpha_{\text{add}}$  [67]:

$$\alpha = \alpha_{\text{OC}} + N_m \alpha_m(\omega) + \alpha_{\text{add}}, \quad (2.45)$$

where  $N_m$  is the number of mirrors and  $\alpha_m(\omega)$  includes the reflectivity curve of one mirror. The signal/idler fields for the next roundtrip  $A'_{s,i}(t, 0)$  are then defined by [67]:

$$A'_{s,i}(t, 0) = \mathfrak{F}^{-1} e^{iD(\omega)} \mathfrak{F} A_{s,i}(t, Ndz). \quad (2.46)$$

To calculate the electric field outside the cavity, signal and idler are multiplied by the transmission of the OC. It defines the outcoupled field. In the Appendix A, an example of the source code of the simulation is presented. In Fig. 2.6, a typical calculation is shown, which is discussed in the next chapter (see Tab. 3.3 and figure caption for parameters). In Fig. 2.6 (a) the DROPO resonances are shown in dependency of the

pump power. It can be seen that the degenerated resonances around 0 fs detuning have the lowest threshold. The output power increases with higher pump powers. In Fig. 2.6 (b) the change of the spectrum of the DROPO with 20 W pump power is shown in relation to the cavity length detuning. The DROPO gives a complex spectral response on the detuning, which depends on higher-order dispersion terms.

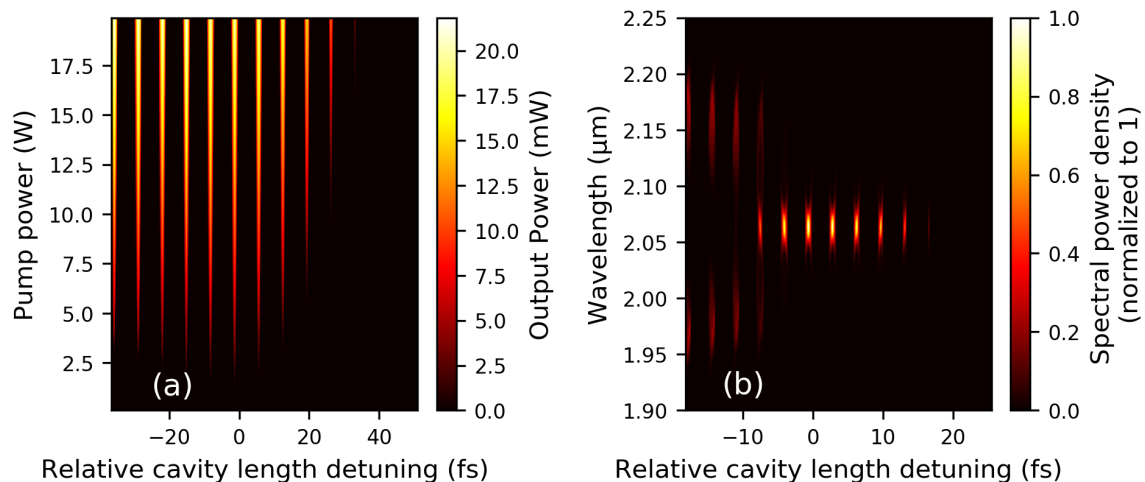


Figure 2.6: Simulation of the emission structure of the DROPO obtained with the split-step based model. The cavity is detuned by a couple of micrometers. Here, a crystal length of 1 mm and an OC of 0.05% is chosen. The GDD is set to  $0 \text{ fs}^2$  and the TOD to  $20000 \text{ fs}^3$ . Detuning resonances with a typical width of a few tens of nanometers appear. (a) Emission behaviour when the pump power is increased. Depending on the threshold of every detuning resonance, individual slopes can be observed. (b) Spectrum near degeneracy with 20 W pump power. At exactly one half of the pump frequency, several peaks appear. The DROPO is switching from the non-degenerated regime to the self-phase locking state.

## 2.7 Conclusion

This chapter includes theoretical considerations used to evaluate the experimental results later in this thesis. Electric fields were discussed as well as the influence of the dispersion on them. Nonlinear processes and their mathematical description were presented. Also, the impact of the cavity on the DROPO and the self-locking effect was

---

described. At last, the split-step based model, which is compared to the experimental measurements in the next chapter was explained.



# Chapter 3

## Impact of higher-order dispersion coefficients

In this chapter, the experimental setup of the DROPO is presented and important parameters of the DROPO cavity are explained. The spectral tuning of the DROPO, depending on the GDD and TOD, is discussed in detail, supported by measurements and simulations. Furthermore, additional spectral effects are revealed and discussed. Parts of the experimental and theoretical results have been published in [74, 67, 75].

### 3.1 Experimental setup

The DROPO is pumped by a home-built Kerr-lens mode-locked Yb:YAG thin-disk laser [76]. The pulse duration is around (270 – 310) fs, the repetition rate is 32.5 MHz and the average power output 24 W, depending on day-to-day performance. In Fig. 3.1 the most important properties of this system are presented. In Fig. 3.1 (a) the typical  $\text{sech}^2$ -shaped spectrum of the laser is shown, which is formed by the soliton solution of the resonating fields in the laser cavity. The spectral width is approximately 3.9 nm (FWHM). In Fig. 3.1 (b) the pulse duration is measured with an A.P.E pulseCheck autocorrelator. For a  $\text{sech}$ -shaped pulse a pulse duration of  $\tau_p = 306$  fs is calculated (FWHM). The time-bandwidth product is 0.336, which is close to the one of a bandwidth limited  $\text{sech}$ -shaped pulse of 0.315 [52]. In Fig. 3.1 (c) the RF spectrum of the laser at its repetition rate is illustrated.



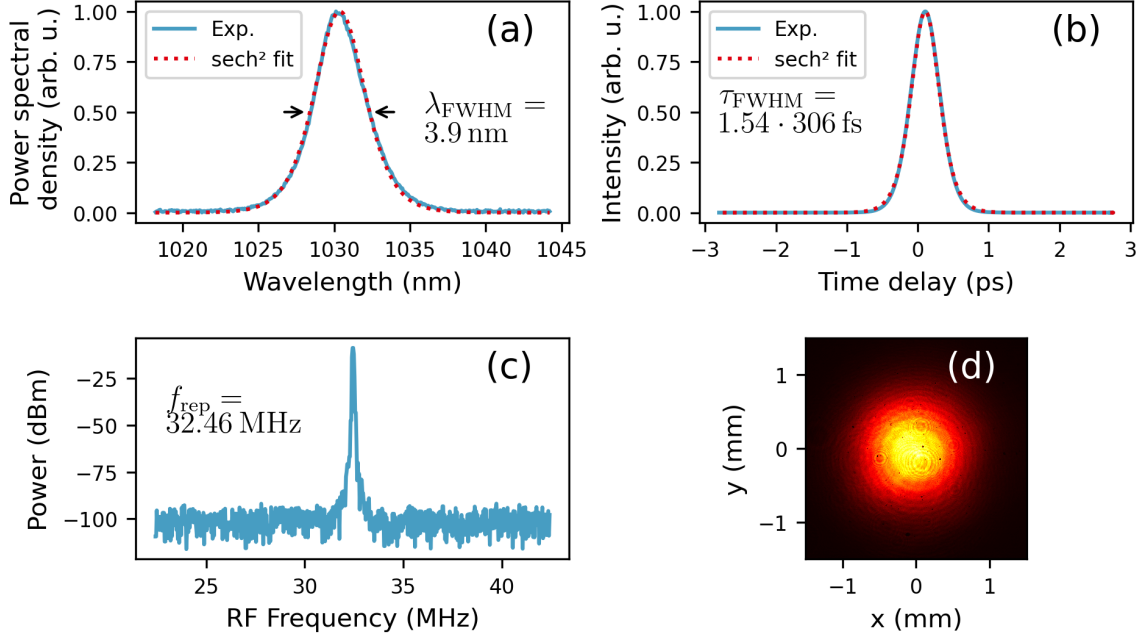


Figure 3.1: Properties of the Yb:YAG pump laser for the DROPO. (a) sech<sup>2</sup>-shaped optical output spectrum of the laser. The recalculated spectral width is around 3.9 nm (FWHM). (b) Autocorrelation of the pulse. The pulse duration for a sech pulse is 306 fs (FWHM). (c) RF spectrum of the pump laser. (d) Gaussian beam profile of the pump.

The outcoupled beam of the laser has a nearly Gaussian profile in space, which is shown in Fig. 3.1 (d). The laser's output power can be controlled by a motorized  $\lambda/2$  wave plate and a thin-film polarizer. The final polarization for the DROPO is tuned by a second  $\lambda/2$  wave plate. The s-polarized pump is focused by a lens with a focal length of 400 mm into the Brewster-cut BBO crystal of the DROPO. The DROPO cavity itself is designed as a bow-tie ring cavity with two focal points, where the nonlinear crystal is placed in the larger one. The length of the cavity can be controlled by a piezo translation drive (piezosystem jena GmbH TRITOR 100, resolution 0.2 nm), together with a manual translation stage. Different dispersive optical plates can be inserted in Brewster's angle into the cavity. The down-converted light is coupled out through an output coupling mirror (OC), with transmissions between 0.5% and 30%. In the following, a basic sketch of the setup is presented in Fig. 3.2 and the parts are discussed in more detail.

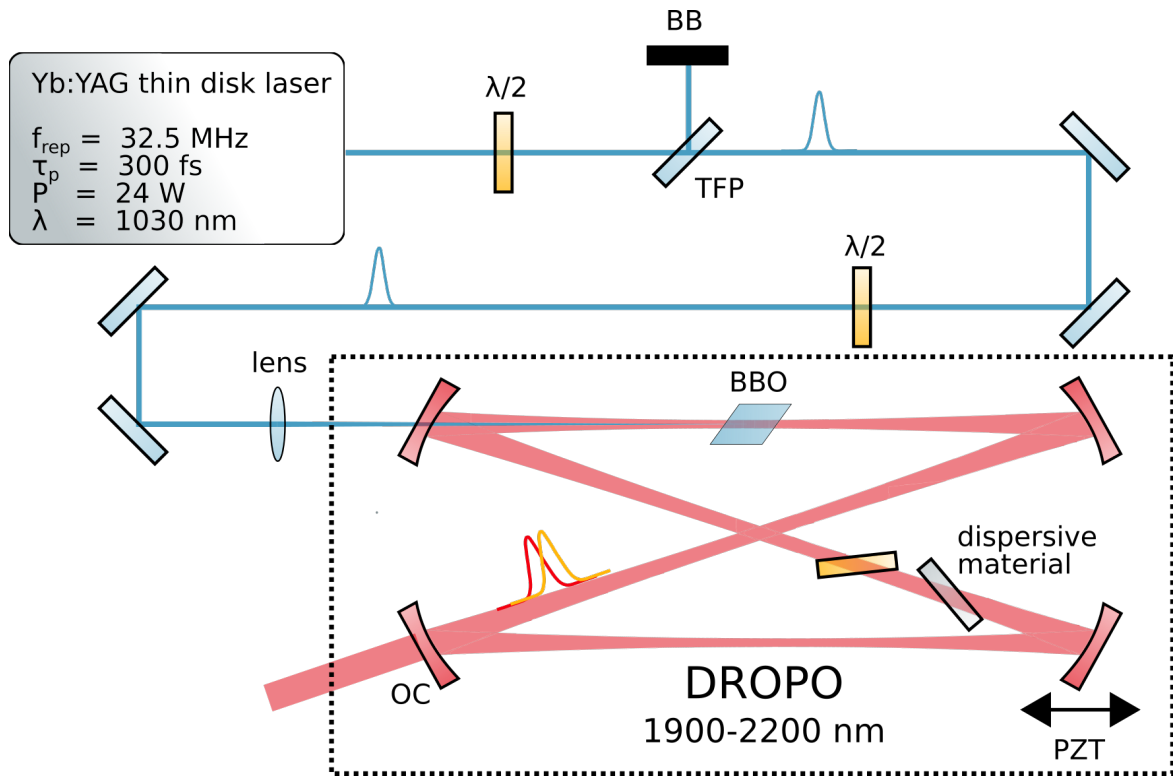


Figure 3.2: Scheme of the DROPO setup. The power of the thin-disk laser (blue) is controlled by a thin-film polarizer (TFP) in combination with a  $\lambda/2$  - wave plate and a beam block (BB). A second wave plate rotates the polarization for efficient pumping and a lens ( $f = 400 \text{ mm}$ ) is focussing the pump into the BBO crystal. The crystal has a thickness between 1 mm and 3 mm. The DROPO cavity (red) has two focussing mirror pairs with radii of curvature (ROC) of 300 mm and 500 mm. Positive and negative dispersive material can be inserted into the DROPO cavity to control the higher-order dispersion terms. The length can be tuned by a piezo translation stage (PZT). The light is coupled out by an output coupling mirror (OC).

## Choice of the nonlinear crystal

BBO is an uniaxial nonlinear crystal. The phase-matching is realized by critical phase-matching (see for details [77, 48]). In the experimental setup, it is used in a type-I  $e \rightarrow oo$  down-conversion configuration. Although the nonlinear coefficient of BBO is approximately  $d_{\text{eff}} = 1.80 \text{ pm/V}$ , and is therefore one magnitude lower than the nonlinearity of a periodically poled lithium niobate (PPLN) ( $14 - 17 \text{ pm/V}$ ), it has some benefits over the PPLN [78]. BBO is not suffering from the photorefractive effect like a PPLN, which allows pumping the crystal with higher powers. Likewise, larger crystals can be produced so that the pump focusing and cavity beam waist radius can be better optimized for the available pump specifications. In this setup, with a central wavelength of  $2064 \text{ nm}$ , the DROPO will work close to the absorption edge of the BBO crystal [79], especially when it operates in non-degenerated mode. The crystal is mounted on a copper block, which cools it sufficiently passively. A suitable alternative to BBO would be a BIBO crystal, which has a higher  $d_{\text{eff}}$  with  $2.60 \text{ pm/V}$ , but a similar phase-matching and transmission profile. With Eq. (2.7) and (2.9), the phase-matching in dependence on the wavelength and the crystal angle,  $\theta$  can be calculated. In Fig. 3.3, the phase-matching curve for DFG with  $1030 \text{ nm}$  pump wavelength inside a  $2 \text{ mm}$  long BBO crystal is illustrated. The phase-matching for the degeneracy can be found at the angle of  $\theta = 21.35^\circ$ . For larger angles, it narrows down to distinct signal and idler. In the experiment, different crystals lengths between  $1$  and  $3 \text{ mm}$  are used. The phase-matching bandwidth increases when the crystal length is reduced. The crystals are cut in Brewster's angle for minimal losses of the signal at a wavelength of  $2064 \text{ nm}$ . Despite the fact that the Brewster's angle is calculated and set for the degeneracy case ( $58.60^\circ$ ), the losses are negligible in the non-degenerated regime, too, because of the wavelength dependence of the Brewster's angle is small. For further information, the crystal geometry is illustrated in detail in Appendix B. The optimal crystal length depends on the temporal and spatial walk-off effect, the used pump power, the focusing of the down-converted and pump light as well as on the cavity specifications e.g. Some of these parameters are difficult to measure or to calculate, but there are some upper limits which can be estimated. Equation (2.11) describes the temporal walk-off of the pump and the signal in the nonlinear crystal. With the group velocity of signal  $v_{\text{gs}} = 1.7897 \cdot 10^8 \text{ m/s}$  and pump  $v_{\text{gp}} = 1.8084 \cdot 10^8 \text{ m/s}$ , the maximum interaction length in the crystal can be calculated to be around  $L_{\text{max}} = 5.2 \text{ mm}$ .

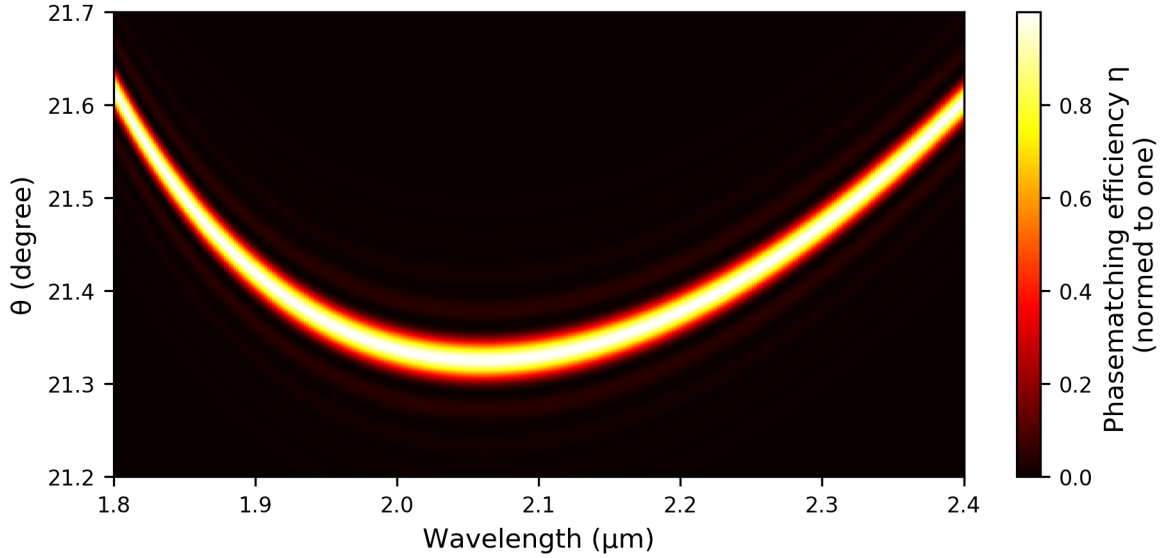


Figure 3.3: Phase-matching of a BBO crystal for difference frequency generation in dependency of the crystal angle  $\theta$  and the wavelength of the down-converted light. The pump wavelength is 1030 nm. The crystal length in this simulation is  $L_c = 2$  mm. At  $\theta = 21.3^\circ$ , the degeneracy point is phase-matched. At this point, the phase-matching is relatively broadband and allows a wide tuneability of the system.

The spatial walk-off of the extraordinary polarized field can be calculated with Eq. (2.10), which is  $\rho = 2.96^\circ$ . For an crystal with a length of 3 mm the spatial offset between pump and signal/idler is around  $150 \mu\text{m}$  after the crystal. For a mode diameter of around  $70 \mu\text{m}$  in the cavity, no efficient interaction between pump and signal/idler at the end of the crystal would be possible. The spatial walk-off defines the maximum of useful crystal length, however depending on the other DROPO parameters even shorter crystals can give a better performance. An analysis can be found in Chapter 4.

## Cavity design

The high reflective (HR) cavity mirrors were manufactured by the Laser Zentrum Hannover [80]. They are coated by the ion beam sputtering method to reach a reflectivity of around 99.9% at 2064 nm and a high damage threshold. Moreover, the mirrors are highly reflective between 1950 nm and 2150 nm for an angle of incidence (AOI) of  $11^\circ$ . The AOI can be tuned up to approximately  $\pm 10^\circ$  without changing the HR

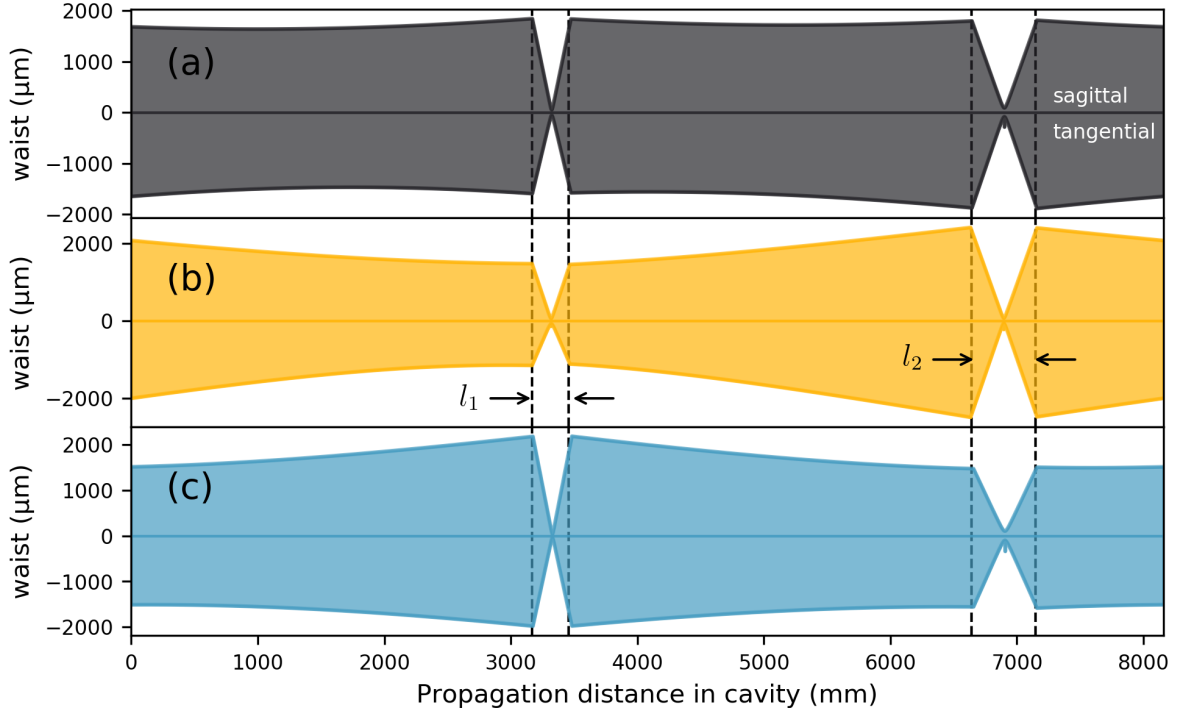


Figure 3.4: Calculated beam waist radius in sagittal and tangential direction for different mode parameters in the used bow-tie cavity. (a-c) The tuning of the curved mirror distance  $l$  of one focal spot can be compensated by the other mirror set by maintaining the maximum of stability in the cavity. In Tab. 3.1, the distances  $l$  and the corresponding beam waists  $w$  in the focus are presented.

regime significantly. The backside of the mirrors has an anti-reflective coating for 1032 nm to pump the crystal. To avoid possible back conversion effects, covered in Chapter 4, the cavity is designed in a bow-tie configuration, to have no second pass through the nonlinear crystal without the presence of the pump. For the design, two pairs of curved mirrors with 300 and 500 mm radius are used in the cavity. The system needs to be synchronized to the repetition rate of the pump (32.46 MHz), which results in a required cavity length of 9.24 m. To calculate the cavity beam radius  $w$ , the commercial software vWaistWatcher is used. It is based on the ABCD matrix formalism. In Fig. 3.4, the resulting cavity modes for different mirror configurations are presented. In (a-c) the distance between the two mirror pairs  $l_1$  and  $l_2$  is tuned slightly. Explicit lengths  $l_1$  and  $l_2$  and the resulting focal beam waists are shown in Tab. 3.1. The simulated modes in Tab. 3.1 (a-c) are calculated in the stability maximum ( $\approx 0$ )

Table 3.1: Focal beam waist radius  $w_{1,2}$  in dependence of the mirror distances  $l_{1,2}$ .

Mode in Fig. 3.1	$l_1$ (mm)	$l_2$ (mm)	$w_1$ ( $\mu\text{m}$ )	$w_2$ ( $\mu\text{m}$ )
(a)	295	523	67	64
(b)	302	512	50	90
(c)	305	500	41	109

of the cavity. By changing the distance between the mirrors, while maintaining a constant stability of the cavity, the beam waist  $w_{1,2}$  can be tuned continuously. In the experiments performed in the scope of this thesis, a configuration is chosen where the two focal points of the mode have radii of around  $50 \mu\text{m}$  and  $70 \mu\text{m}$ . The BBO crystal can be positioned in both focal spots. Nevertheless, in the  $50 \mu\text{m}$  spot the crystal was quickly damaged by the high intensities in experiment, therefore only the larger focus is used. The astigmatism of the mirrors is nearly compensated by the Brewster-cut crystal in the focus and can be further compensated by additional plates in the second focus. The tuning of the DROPO in the spectral regime has only a small effect on the mode and can be neglected. For all presented experiments, the pump spot size is around  $110 \mu\text{m}$  which is generated by a  $400 \text{ mm}$  lens. One mirror is mounted on a translation stage to tune the cavity length manually by hand. Moreover, a piezo actuator (piezosystemjena TRITOR 100) can tune the cavity length by up to  $160 \mu\text{m}$  with sub-nanometer precision. Additionally, a rapidly tunable piezo (PT130.20) is used for the stabilisation (see Chapter 4 and 5). In Appendix B, the detailed design of the cavity is presented.

## Dispersive materials

To change the roundtrip dispersion inside the cavity, various materials can be inserted in the collimated parts of the cavity. The requirements for these plates are a high transparency at the DROPO wavelength and should be available with low imperfections and defined surface form tolerances. In the  $2 \mu\text{m}$  wavelength range, materials with positive and negative group velocity dispersion (GVD) can be found. The TOD for all used materials is positive. Suitable negative dispersive materials are BBO and fused silica, where ZnSe, Si, GaAs, GaP and air have positive GVD. For the exper-

Table 3.2: GVD and TOD for different materials with  $\lambda_0 = 2064$  nm

Material	GVD (fs <sup>2</sup> /mm)	TOD (fs <sup>3</sup> /mm)
$\beta$ -BBO [72]	-140	+1042
Fused silica [81]	-115	+526
BaF <sub>2</sub> [82]	-5	+80
ZnSe [83]	+247	+315
GaP [84]	+503	+682
Silicon [85]	+781	+979
GaAs [86]	+981	+1440
Air[87]	$+7.6 \cdot 10^{-4}$	+0.11

iments, only BBO, air, fused silica and ZnSe are used, as these materials are also transparent for a 515 nm or 700 nm alignment beam. In Tab. 3.2 some GVD and TOD values are presented. Since the down-converted light around 2064 nm is near to the absorption bands of water, also the humidity in the air needs to be taken into account. A temperature of 295 K and the atmospheric pressure is chosen. The humidity in the laboratory is around 60% and increases the TOD of the air from 0.008 fs<sup>3</sup>/mm at 0% humidity to 0.11 fs<sup>3</sup>/mm.

## 3.2 Spectral tuning behaviour

In the following part, the general cavity length detuning behaviour is explained in detail and how it depends on the GD, GDD and TOD.

### Higher-order dispersion in the cavity

Equation (2.18) in Chapter 2 describes the relative phase relationship between pump, signal and idler, which lead to the typical on-off switching of the DROPO. For further analysis we can modify this equation to:

$$0 = \phi_s + \phi_i + 2\pi N, \quad (3.1)$$

where  $N = 1, 2, 3, \dots$  is an integer, which represents the periodicity of the phases. The pump phase  $\phi_p$  is set to  $\pm\pi/2$ . The phases  $\phi_s$  and  $\phi_i$  are affected by the higher-order dispersion in the system. With Eq. (2.34), the round-trip phase of signal and idler for a given signal frequency  $\omega$  and idler frequency  $2\omega_0 - \omega$  can be expanded up to the third order around the DROPO's central frequency  $\omega_0$  by:

$$\phi_s(\omega) = \phi_{0s} + (\text{GD} + \delta\tau)(\omega - \omega_0) + \frac{1}{2}\text{GDD}(\omega - \omega_0)^2 + \frac{1}{6}\text{TOD}(\omega - \omega_0)^3 + \delta\tau\omega_0 \quad (3.2)$$

$$\phi_i(\omega) = \phi_{0i} + (\text{GD} + \delta\tau)(\omega_0 - \omega) + \frac{1}{2}\text{GDD}(\omega_0 - \omega)^2 + \frac{1}{6}\text{TOD}(\omega_0 - \omega)^3 + \delta\tau\omega_0, \quad (3.3)$$

where  $\omega_0$  is half of the pump frequency and  $\delta\tau = \Delta L/c$  the added time delay per length change  $\Delta L$  when the cavity length is detuned. If the two Taylor series are inserted into the round-trip phase-matching equation (3.1) the odd GD and TOD term are cancelling each other out<sup>1</sup>. These Taylor series lead to the final equation [67]:

$$\delta\tau(\omega, N) = -\frac{1}{2\omega_0}\text{GDD}(\omega - \omega_0)^2 - \frac{\pi}{\omega_0}N. \quad (3.4)$$

Using this equation, the shape of the DROPO's resonances in the spectral domain can be calculated. Equation (3.4) satisfies various combinations of the cavity time delay of the DROPO, the GDD, and the DROPO frequencies. When the cavity time delay is detuned, different DROPO signal and idler frequency pairs can be generated in a single resonance. Due to the periodicity of the round-trip phase-matching equation multiple resonances appear, which are separated by a time delay of  $\frac{\pi}{\omega_0}$ . For non-zero GDD values one resonance forms a parabola with its vertex located at  $\omega_0$ . The opening direction of the resonance is determined by sign of the GDD. The case is interesting when the GDD is compensated. In this case the resonance becomes frequency independent. In the further course, a second mechanism that affects the frequency of the DROPO and establishes them in the zero GDD is described.

The arrival time of the pulses in the crystal is important for the amplification process, too. In general, the optimal amplification is reached, when the pump, signal and idler

---

<sup>1</sup>I want to thank the anonymous reviewer of [67] for his additional remarks to this derivation.



pulses have the optimal overlap. However, when the signal and idler pulses propagate through the cavity, their group delay is influenced by the dispersion profile, resulting in a delay between the two pulses. When the pulses in the crystal interact with the pump, they are amplified depending on their overlap with it. With the assumption that optimal amplification occurs at best pulse overlap, the resulting DROPO frequencies can be calculated. The group delay curve  $\text{GD}_R(\omega)$  describes the group delay for a pulse with a central frequency  $\omega$ . This curve can be derived with Eq. (2.34) [67]:

$$\text{GD}_R(\omega) = \frac{\partial \phi(\omega)}{\partial \omega} = \text{GD} + \text{GDD}(\omega - \omega_0) + \frac{1}{2}\text{TOD}(\omega - \omega_0)^2 + \delta\tau. \quad (3.5)$$

It is important to distinguish between the curve  $\text{GD}_R(\omega)$  and the coefficient GD of Eq. (3.2) and (3.3). For perfect synchronous operation of the DROPO, the round-trip time of signal and idler needs to be matched to the repetition rate. The synchronous frequencies can be calculated with Eq. (3.5) by taking into account the added time delay  $\delta\tau$  and cavity dispersion. For efficient amplification of frequencies, both equation (3.4) and (3.5) should be fulfilled.

## Experimental verification

For experimental verification, a 2-mm-long BBO crystal and a 2% OC are used. The high finesse of the cavity, due to the low output coupling, increases the detuning sensitivity (see Chapter 2.5) of the DROPO and lowers the threshold, so it can be pumped with less power. The low pump power allows avoiding a possible thermal expansion of the crystal and additional third order effects like self phase modulation and four wave mixing [88]. Moreover, the dispersion is tuned by fused silica and ZnSe plates, which are placed in the collimated part of the cavity mode. With this combination, the GDD can be tuned from the negative to the positive regime, while the TOD is positive. The mirrors of the cavity are not chirped. Their GDD and TOD can be neglected. The outcoupled beam is coupled to an OCEAN NIR-QUEST256 spectrometer, which measures the optical spectrum. When the cavity is matched to the repetition rate of the pump, the cavity length can be detuned by several micrometers in operation, depending on the crystal length, the transmission of the output coupler and the built-in materials, which are inducing additional losses.

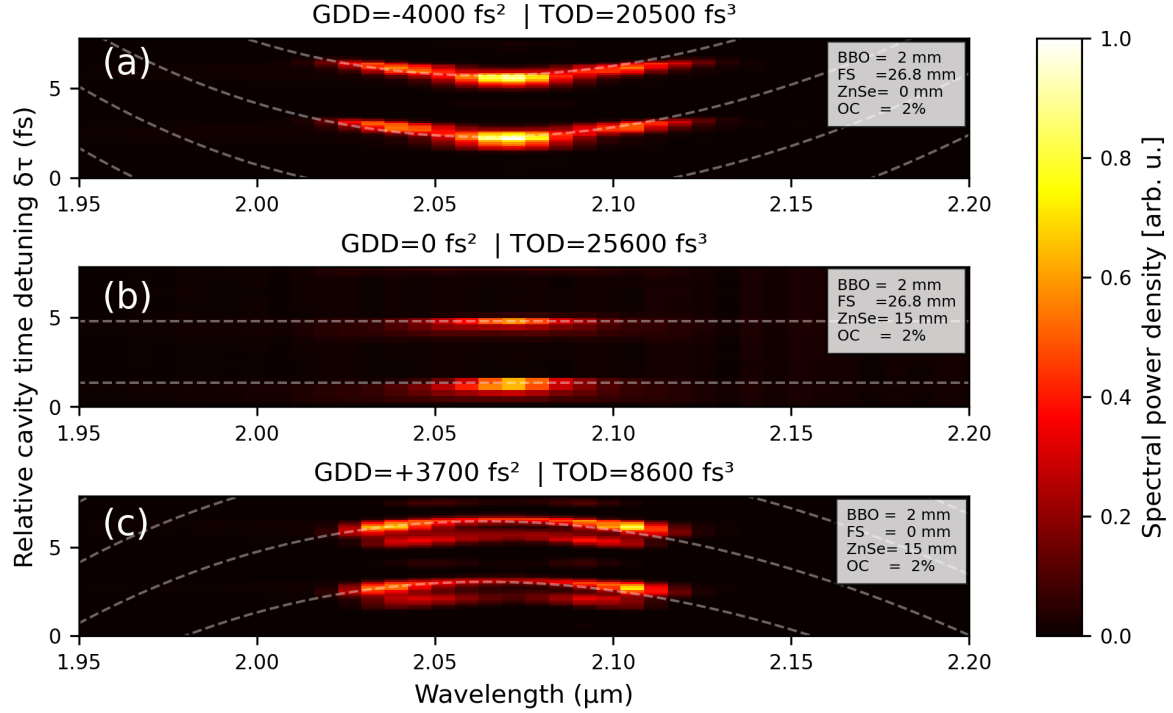


Figure 3.5: Experimental measurements of discrete detuning resonances at the degeneracy of the DROPO, when the cavity length is detuned. The parameters of the inserted optical plates, crystals and OC are presented in the small gray box. The theoretically predicted roundtrip phase-matching resonances are presented as gray dotted lines. (a-c) DROPO resonances, with negative, zero and positive intracavity GDD. The curvature of the resonances, which is described by Eq. (3.4), can be clearly seen.

Figure 3.5 shows the optical spectrum of single resonances at degeneracy in dependence of the cavity length. They were taken from the full measurement in Fig. 3.6. Three measurements with different combinations of FS and ZnSe plates at degeneracy are presented. The measurements are examples of cases with negative, zero and positive GDD per cavity roundtrip. The wavelengths that fulfil Eq. (3.4) are plotted as dotted lines. It can be seen that the theoretical considerations agree well with the experimental measurements. The resonances have, as predicted, a distance of one half of the DROPO's central wavelength. The bending, which is caused by the non-zero GDD in Fig. 3.5 (a) and (c), matches well to Eq. (3.4). In Fig. 3.5 (c) additional weaker resonances can be seen, which appearing at specific conditions, especially with low losses in the cavity. This additional resonances are discussed further in Sec. 3.3.

When the GDD is not zero, the DROPO can be detuned smoothly from the degeneracy to the non-degenerated state in one resonance (see Fig. 3.5 (a,c)). Why the DROPO stops to emit at a certain detuning on one resonance is not sufficiently clear. The specific shape of the resonance and tunability depends on the cavity properties like gain, losses or crystal length. The work of D. N. Puzyrev and D. V. Skryabin [89] on the tuning curves of  $\chi_{(2)}$  microresonators is interesting for this topic. The theory may be adapted to DROPO systems, to better explain the shape of single resonances in the future.

At the zero GDD point the full resonance is degenerated and no wavelength tuning on one resonance is possible. While the individual resonances are well described by the

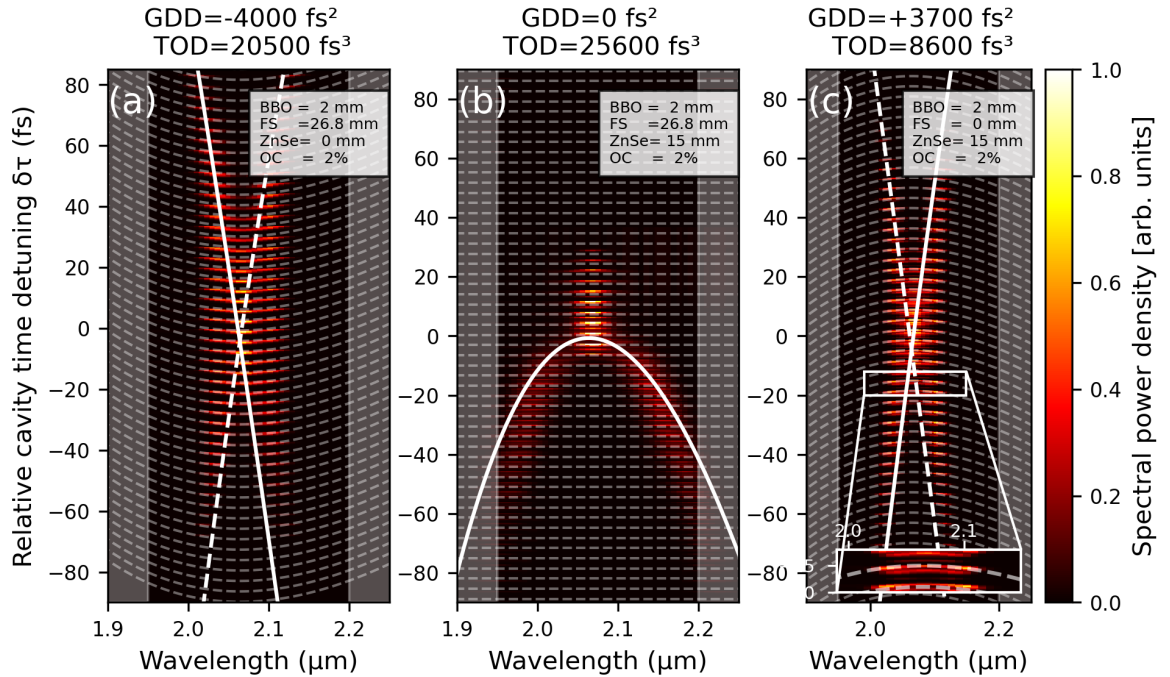


Figure 3.6: Experimental measurements of the global spectral detuning characteristics of the DROPO (see also [67]). The gray bars left and right indicate the borders of the HR mirrors. The white continuous line is the group delay curve from Eq. (3.5), which describes the synchronized wavelengths with the pump. The white dotted lines symbolize the non-group-matched colors in the non-zero GDD regime. (a,c) X-shaped structure with negative or positive GDD. (b) Inverse Y-shaped structure with self-phase locked regime at the top. The GDD is set to zero.

roundtrip phase matching condition (Eq. (3.1)), the group delay curve Eq. (3.5) plays an important role for the global detuning behaviour of the DROPO. Depending on the GDD and TOD, the DROPO's signal and idler pulses have different relative group delays in respect to the pump pulse, which result in different emission behaviour of the system. In Fig. 3.6 the full detuning of the DROPO with (a) negative, (b) zero and (c) positive GDD, with their group delay curve is presented. The TOD is in all three cases positive. The grey bars, left and right in the subplots indicate the limitation of the bandwidth, namely the reflectivity of the cavity mirrors. The dotted lines indicate Eq. (3.1) for every resonance. A small length mismatch between the measured resonances and the theoretically predicted is noticeable due to a small inaccuracy of the piezo system or drifts of the DROPO cavity.

When the cavity length is detuned, different wavelengths are synchronized with the pump. The continuous white line in Fig. 3.6 presents this group delay matched frequencies from Eq. (3.5) in dependency of  $\delta\tau$ . The equation has the form of a parabola. The coefficient GD of Eq. (3.5) is fitted, so that the group delay curve intersects the degeneracy of the measurement. In Fig. 3.6 (a), the GDD is negative and therefore the vertex of the parabola is not at degeneracy. The curve can be approximately seen as a straight line in this graph. It can be recognized that for negative relative cavity time detuning only the idler and for positive only the signal is group delay matched. Due to the energy conservation, the other signal/idler (dotted line) also needs to be generated, which leads to the X-shaped detuning plot. This applies analogously to the case with positive GDD, which can be seen in Fig. 3.6 (c). In the zero GDD regime in Fig. 3.6 (b), the group delay curve is a parabola. Both signal and idler are synchronized to the repetition rate of the pump at the same time detuning. The DROPO can be detuned from the non-degenerated resonances to pure degenerated resonances, which occurs at the vertex of the group delay (GD) parabola. Here, the frequency  $\omega_0$  is group delay matched, resulting in optimal performance of the system at degeneracy. The TOD term in the group delay equation determines whether the parabola is open in the positive or negative detuning direction. When the TOD is positive, it is not possible to group delay match any wavelength to the pump for positive relative cavity time detunings. The description of the global emission behaviour of the DROPO, using the group delay curve, is systematically investigated for the first time in this thesis and in [67]. In Fig. 3.7, another measurement with a 3 mm crystal and full

pump power is illustrated. It is pumped with full power and due to the higher gain, the DROPO can be detuned in a larger regime than in Fig. 3.6. Several detuning resonances are measured. In comparison to the measurements in Fig. 3.6, it can be recognized that in Fig. 3.7 (a) and (c), the change of the DROPO wavelengths on one resonance (see small inlay) stagnates in the non-degenerated regime and deviates from the roundtrip phase matching condition. The origin of this effect is still unknown; it can be assumed that third order nonlinearities like self phase modulation can be the reason. The global emission behaviour is following the group delay curves, too. There is a strong consistency between measurement and the theoretical considerations. At zero GDD, the influence of the mirror borders is well visible, beginning at  $-50$  fs. The DROPO's emission wavelengths start to deviate from the group delay curve. The system tries to find a balance between minimum losses and maximum gain along the group delay curve. This example shows that the group delay matching acts as a soft criterium. It can be expected that the gain on the GD curve is the highest, but the oscillator is running at the point, where gain minus losses is maximum. Besides this, it can be seen that in the high loss region, where the borders of the HR mirrors are, the detuning resonances get broader. This effect is explained in Section 4.6, where the dependence between the detuning resonances width and the losses is described in more detail.

The self-phase locking state can appear in all three dispersion regimes where the central wavelength around  $2064$  nm is group delay matched. However, it is more suitable to choose the running point at zero GDD when the DROPO should be used at degeneracy.

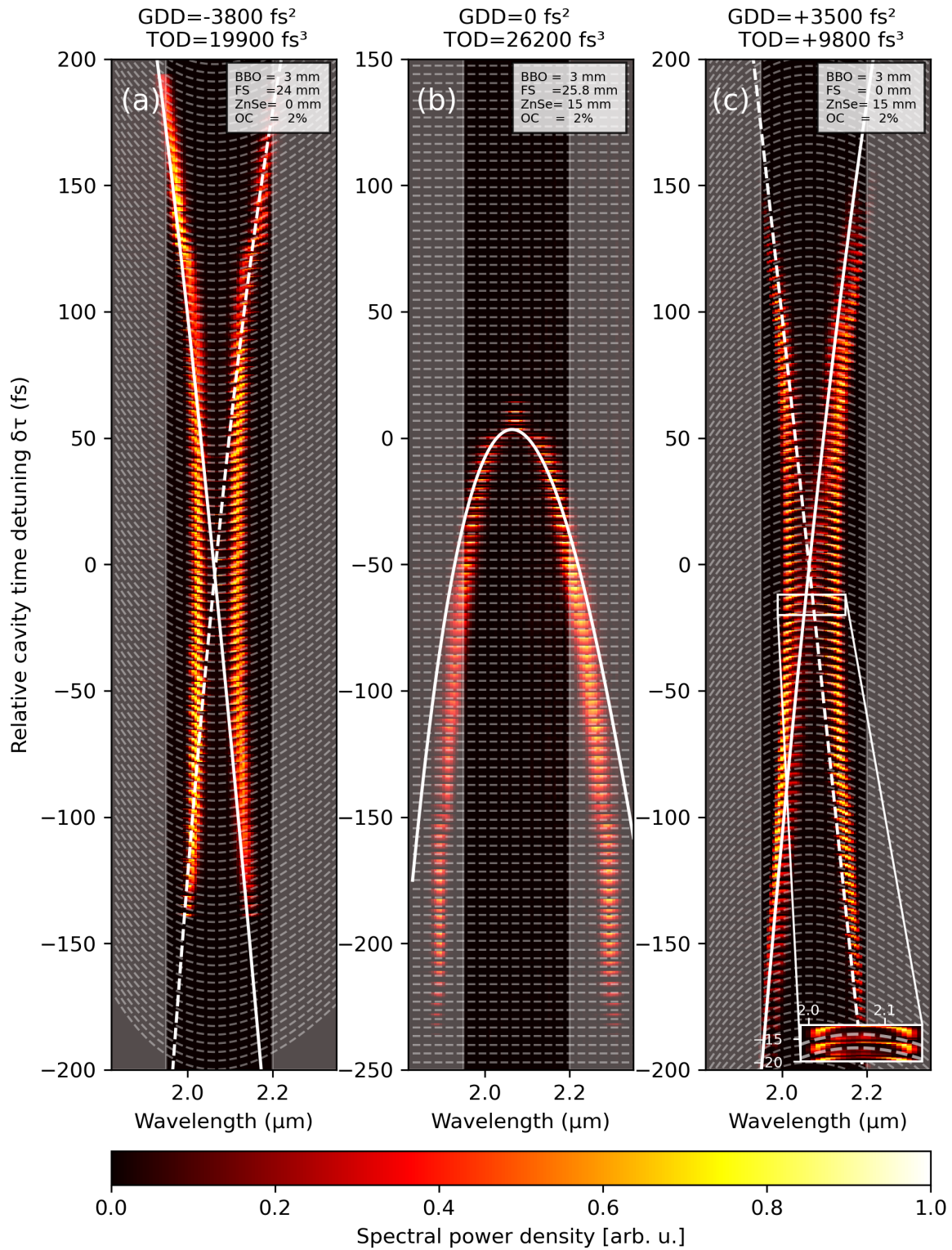


Figure 3.7: Experimental measurements with a 3 mm crystal, 16 W pump power and 0.5% output coupling for different values of intracavity dispersion. Even when the DROPO is detuned on large scales, DROPO resonances can be measured. The consistency between Eq. (3.4 - 3.5) and the experiment can be seen, too.

## Simulation with the split-step based model

The detuning behaviour of the DROPO can be analysed and predicted by the numerical model, which is introduced in Chapter 2.6. The model is implemented with the programming language Python [90] and the corresponding libraries NumPy [91], Matplotlib [92], SciPy [93] and Pickle [94]. An example script can be found in Appendix A. Uwe Morgner, Ihar Babushkin and Ayhan Demircan programmed the main framework, and it was extended at the group workshop 2018 by several persons including Sven Kleinert. The code was adapted to the DROPO setup by the author of this thesis. With small effort, the program can be used for other DROPO systems. The used parameters in this thesis are shown in Tab. 3.3 [67].

Table 3.3: Constants and variables for the numerical model

explanation	variable	value
points in the time/frequency frame	$N$	512
maximum number of round-trips	$N_r$	300
time window	$T$	14 ps
crystal thickness	$L_c$	2 mm
effective nonlinear susceptibility	$d_{\text{eff}}$	1.83 pm/V
nonlinear interaction parameter	$\kappa$	$3.4 \cdot 10^{-6} \text{ V}^{-1}$
phase-matching angle	$\theta$	$21.32^\circ$
2 mm crystal GDD	$\text{GDD}_c$	$-250 \text{ fs}^2$
2 mm crystal TOD	$\text{TOD}_c$	$+2400 \text{ fs}^3$
pump wavelength	$\lambda_p$	1032 nm
pump pulse duration	$\tau_p$	300 fs
repetition rate	$f_{\text{rep}}$	32.6 MHz
number of mirrors	$N_m$	12
losses of all mirrors at degeneracy	$\alpha_m$	5%
output coupling losses	$\alpha_{\text{OC}}$	2%
additional cavity losses	$\alpha_{\text{add}}$	10%

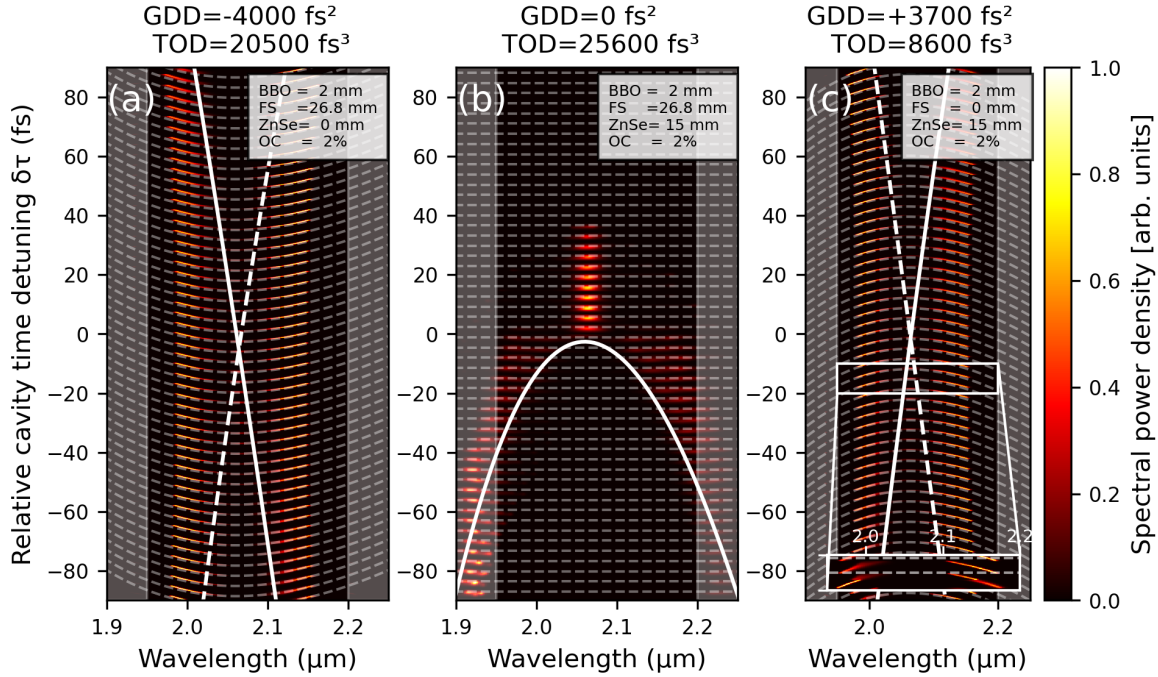


Figure 3.8: Split-Step based simulation of the DROPO (see also in [67]) with the numerical model of Sec. 2.6. The influence of the round-trip phase condition and the group delay matching can be recognized. The simulations are in good agreement with the experimental measurements, presented in Fig. 3.6.

The time window is large enough to avoid that the pulse is effected by the borders in the time domain. In the main loop, the spectrum for different cavity lengths is calculated. In Fig. 3.8 the results from the model are represented. The cavity parameters from the experimental results presented in Fig. 3.6 are used in this simulation. To match the experimental resolution, a Gaussian filter function is used, which is smoothing the theoretical results. The simulation agrees very well to the experiment. Not only the detuning resonance in dependency to the GDD are correctly simulated, but also the group delay curve fits well to the simulation. To fit the calculated to the experimental data, additional cavity losses of 10% are chosen. Various effects can be the reason for the difference in losses. Since the numerical model has only one spatial dimension and uses the plane wave approximation, spatial effects like spatial pump inefficiencies, which depend on the focused Gaussian light beams, birefringence of the crystal and spatial walk-off are not taken into account [95]. In addition to the DFG, parasitic SFG



processes between pump and signal/idler can also take place, which are not included in the model. Unknown losses from the crystal, defects in the mirrors or absorption from air can lower the performance of the experiment, too.

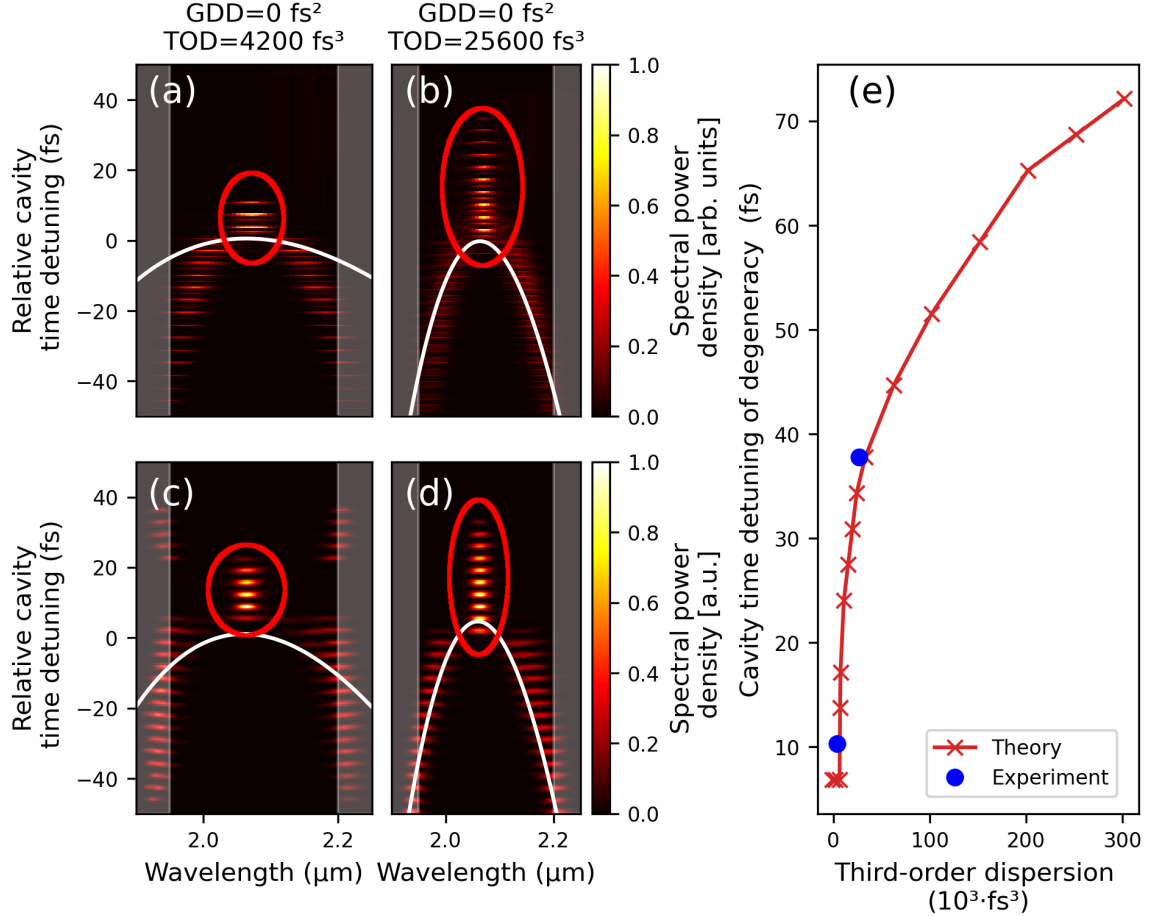


Figure 3.9: (a-b) Experimental measurements with  $\text{GDD} = 0 \text{ fs}^2$  and different TODs (see also in [67]). (c-d) Corresponding simulations. (e) Sum of relative cavity time detuning of all degenerated resonances in dependence of the TOD.

Equation (3.5) depends quadratically on the TOD. With a suitable ratio between ZnSe and FS, the GDD can be kept at zero. By increasing the amount of both, the TOD can be tuned further into the positive regime. In Fig. 3.9 (a-b) two measurements and their simulations (c-d) can be seen. The DROPO is configured with a low TOD profile in Fig. 3.9 (a) by using 3 mm BBO and 1 mm ZnSe. The second configuration has a high intracavity TOD by introducing 3 mm BBO and 15 mm ZnSe and 26,8 mm FS,

which can be seen in Fig. 3.9 (b). The system is adjusted in the experiment to optimize the maximum amount of degenerated detuning resonances. If the TOD is increased by maintaining zero GDD, the group delay curve (white thick line), which has at zero GDD the shape of a parabola, is stretched along the relative cavity time detuning axis. With high TOD values, the DROPO cavity needs to be detuned more to change significantly the spectral behaviour. This can be seen in the experiment, too. For the low TOD case, only a few degenerated resonances can be measured. Three resonances can be recognized, which gives a total relative cavity time detuning around 10 fs for all degenerated resonances. For the high TOD many more degenerated resonances are visible. Here, a relative cavity time detuning of around 38 fs can be achieved. This shows that higher TOD values lead to more resonances in the degeneracy regime. This effect can be beneficial for certain stabilization schemes and better handling of the system. To control the TOD, high amounts of material need to be introduced into the system. This can have a negative impact on the performance of the DROPO. To avoid this effects, tailored chirped mirror designs to control the cavity GDD and TOD can be used in future system designs.

The experimental data can be compared with the numerical model, which can be seen in Fig. 3.9 (d-e). The experimental results agree with the model when the parameters of Tab. 3.3 are used. An interesting case is where the GDD and TOD are zero and Eq. 3.5 is a constant. The simulation of this situation is shown in Appendix A. The spectral behaviour in this case is symmetrical again, and non-degenerated detuning resonances appear on both sides of the degenerated ones. With zero GDD and TOD, all frequencies, which are phase-matched by the nonlinear crystal, can resonate in the cavity simultaneous on one detuning resonance. However, it is not clear if such a system is stable. Figure 3.9 (c), with its low TOD value is in the transition to this state and in the positive detuning region, non-degenerated resonances are appearing. However, in the experiment, it was not possible to measure them. A reason could be that the amplification of these resonances is relatively low in the experiment and they are not overcome the DROPO threshold.

In the outlook of this thesis a way is described to use the zero GDD and TOD regime to possibly generate few cycle pulses with this dispersion regime with a DROPO.

### 3.3 Spatial effects, spectral dependencies on the pump power and crystal phase-matching

In the following, secondary spectral effects are discussed. Higher-order transversal modes, dependence of the spectral tuning to the crystal phase-matching angle and pump power are presented.

#### Spatial effects of the cavity length detuning

In some cases, when the system is well-adjusted, the output coupling is low or the pump power is relatively high, additional resonances appear between the already discussed ones, which were observed in [61], too. In Fig. 3.10 an example of these resonances

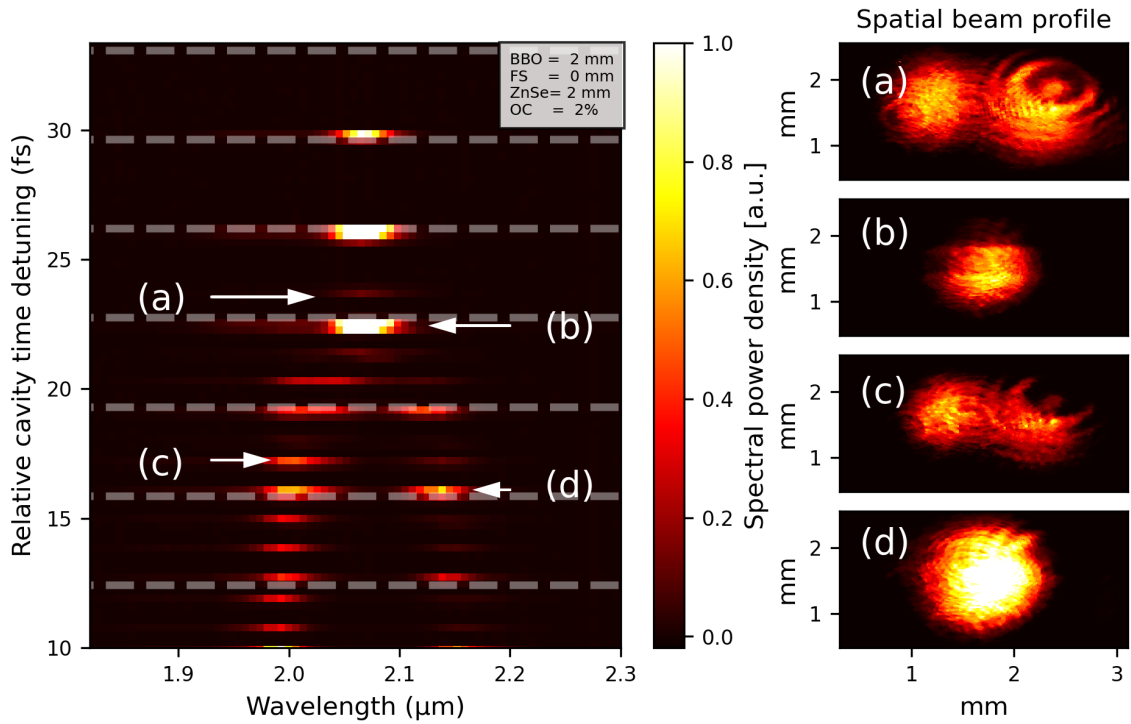


Figure 3.10: Left: detuning resonances of a DROPO. The beam profile and optical spectrum is measured simultaneously when the cavity length is detuned. A 2 mm crystal with an OC of 2% is used. Right: beam profile measured with a CCD camera. The theoretically predicted detuning resonances (b,d) and extraordinary ones (a,c) correspond to  $TEM_{00}$  and  $TEM_{10}$  transversal modes.

is presented. On the left-hand side, a typical detuning measurement is shown. The additional detuning resonances like (a) and (c) are position on a third of the usual length between the main lines (b) and (d). On the right-hand side of Fig. 3.10 the spatial profile is measured by two photon absorption on a silicon CCD chip. It can be seen that the DROPO runs in (a) and (d) in the  $TEM_{10}$  Hermite-Gaussian transversal mode. The interference pattern is caused by scattering on an optical absorption filters. Why this additional lines appear is not completely clear. A reason can be that the higher-order transversal modes shift the roundtrip phases of the electric fields, similar to the mode dispersion in fibers [96], so that the resonances of the DROPO appear at different positions.

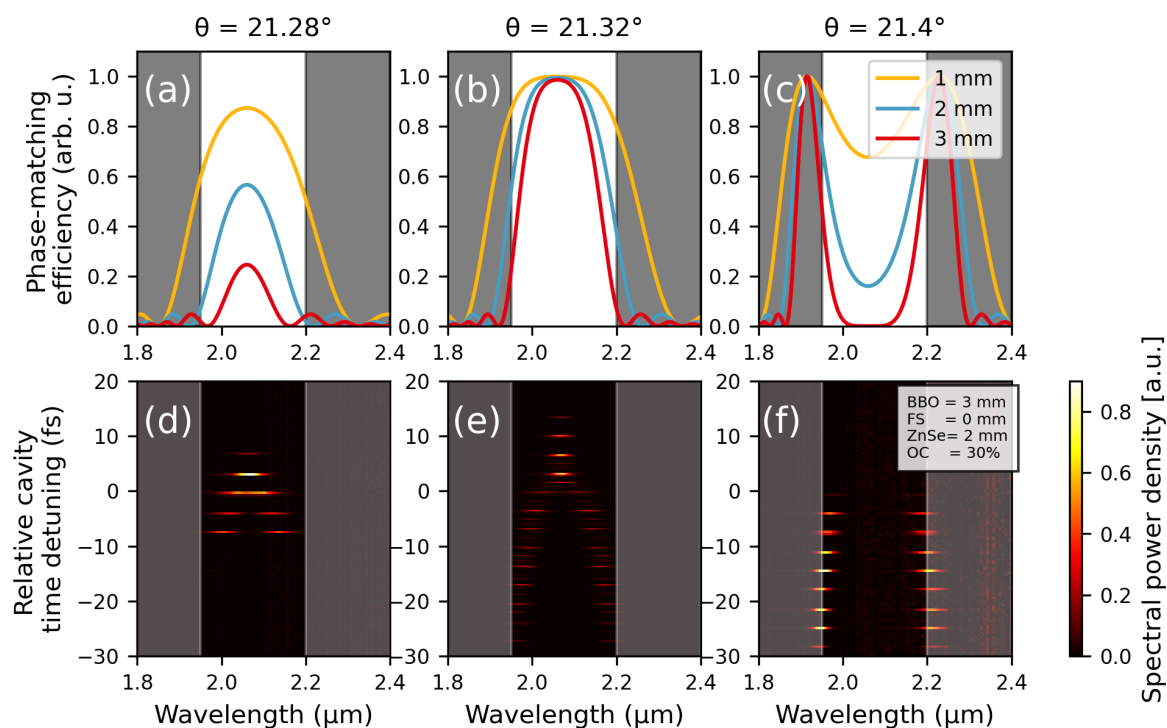


Figure 3.11: Detuning of the nonlinear crystal angle  $\theta$ . In the top row slices of the phase-matching curve in Fig. 3.3 for different crystal thicknesses are presented. In the bottom row the experimental results are shown. With the optimal phase-matching angle the degenerated and non-degenerated regime of the DROPO can be measured (b,e). Small detuning of the angle can lead to emission at degeneracy only (a,d) or outside in the non-degenerated regime (c,f).

### **Influence of the phase-matching angle**

The phase-matching angle for degeneracy is around  $\theta = 21.32^\circ$ . When the crystal is set into the cavity, it needs to be fine-tuned to that angle. In Fig. 3.11, simulations and measurements for small phase-matching angle detunings are presented. Figure 3.11 (a-c) show the calculated phase-matching curve for specific crystal angles, which is shown above the plots. Since this small angular changes ( $\sim 0.05^\circ$ ) within the crystal could not be measured precisely, in Fig. 3.11 (d-f) corresponding measurements for the three calculated examples are presented. When the phase-matching angle is tuned from lower to higher values, the wavelengths at degeneracy are phase-matched first with low efficiency (see Fig. 3.11 (a,d)). At around  $21.32^\circ$  the degeneracy point is optimally phase-matched in the calculation. The highest output powers at degeneracy should be expected here (see Fig. 3.11 (b,e)). For the presented measurements in this thesis the middle configuration is chosen, to provide the highest gain at degeneracy. For higher phase-matching angles, the efficiency of the degeneracy is decreasing and non-degenerated wavelengths are phase-matched. It is possible to avoid degeneracy at all (see Fig. 3.11 (c,f)).

### **Pump power dependence**

The DROPO resonances change with the pump level. In Fig. 3.12 (a-c), a resonance is presented for different pump powers. It is measured in a cavity with negative GDD around  $-3900 \text{ fs}^2$  and a TOD of  $20000 \text{ fs}^3$ . The crystal of 3 mm and a 2% OC are used. For low pump levels first the degenerated frequencies overcome its threshold and with higher pumping the non-degenerated appear. This behaviour can be explained by the lower threshold of the degenerated ones. When the DROPO is tuned along one resonance, the system switches from the non-degenerated regime to the degenerated mode. A more detailed analysis can be found in the work of R. Hamerly [68]. In that work, the detuning behaviour of single resonances is explained with a linear Eigenmode theory for synchronously pumped DROPOs.

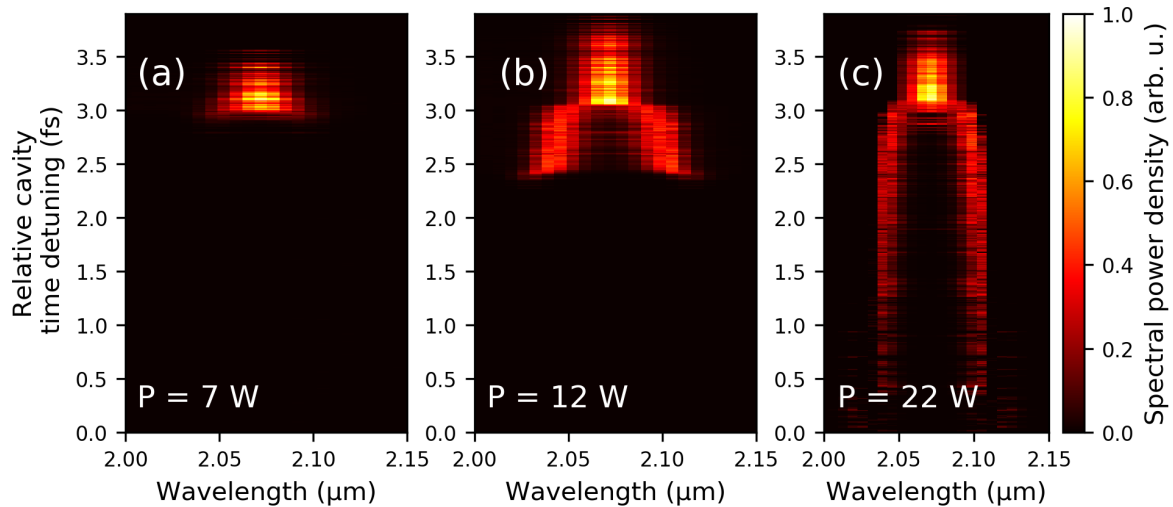


Figure 3.12: Single DROPO resonance at degeneracy for a cavity with negative GDD in dependence of the pump power. When the pump power is increased, the DROPO wavelength regions change. The DROPO can be tuned continuously on one resonance from the non-degenerated frequencies to the degeneracy.

### 3.4 Conclusion

In this chapter, the experimental DROPO setup was introduced and important parameters were described. The spectral dependency on the cavity length detuning and the influence of the higher-order dispersion were measured and simulated by the numerical model. The agreement between the theory and the experiment is remarkably strong. The detuning lines follow the predicted curves, which depend mostly on the GDD term. The X- and Y-shaped structures were observed and described well with the GD dependence. An increase of the tolerance against detuning of the degenerated regime with higher TOD values were measured and simulated. With the existing experimental setup, single detuning resonances can be resolved with high resolution. All in all, the detuning behaviour of the DROPO for different dispersion regimes are now well described and understood and can help in designing future systems.



# Chapter 4

## Resonant enhancement

### 4.1 Introduction

In this chapter, the DROPO's energetic balance at high pump powers and low losses are discussed. Motivated by passive enhancement cavities (EC) [97, 98, 99], which can store energies hundreds of times those of the pump, the exploration of the ability to generate high amplitude fields within a DROPO are presented here. They are suitable for experiments involving high harmonic generation in solid materials [100]. The DROPO's enhancement is expected to be lower than that of a passive EC, because of the intrinsic back conversion of the signal/idler frequencies to the pump, which is phase-matched in the crystal, too. Additional effects can play a role, like parasitic SHG of signal/idler, inefficiencies in the conversion process, like temporal/spatial mismatch between signal/idler and pump, and additional losses in the cavity. But with the recently developed high power pump oscillators [101, 102], allowing the delivery of high energies at MHz repetition rates, the breaking of the threshold of gas plasma generation with the intracavity down-converted light can be expected in the near future.

In the following section, a reduced analytical model for electric field amplitudes with pump depletion is used to describe the effects of down- and up-conversion of the pump and the signal/idler in the nonlinear medium in the DROPO. This model gives simpler insights on the system's dynamical effects than the split-step based method presented in previous chapter. It has the drawback of a reduced accuracy, as it does not include higher-order dispersion and effects such as birefringence or the temporal walk-off in



the crystal. Nevertheless, design principles for strong fields in the DROPO are derived and compared with experimental data. The derivations and results in this chapter have been published in [103, 104, 105].

## 4.2 Amplitude based model of the nonlinear interaction

When a DROPO has a high finesse cavity, similar to a passive enhancement cavity, the dynamical effects of pump and signal/idler in the crystal need to be taken into account. The coupled differential equations of the second order nonlinear process and the crystal phase-matching in the DROPO were introduced in Chapter 2. With the assumption that the DROPO operates at degeneracy, full phase-matching, neglecting dispersion and the temporal pulse shape, Eq. (2.14 - 2.16) in the crystal after a propagation length  $z$  can be simplified to [105, 61, 53]:

$$\frac{dA_s(z)}{dz} = -\kappa A_p(z)A_s(z) \quad (4.1)$$

$$\frac{dA_p(z)}{dz} = \kappa A_s^2(z), \quad (4.2)$$

where  $A_s$  and  $A_p$  are the real field amplitudes of the signal and pump field. The nonlinear interaction parameter is in the following defined as

$\kappa = 2\omega_s d_{\text{eff}}/cn \approx 3.4 \cdot 10^{-6} \text{ 1/V}$ . Using the normalized and dimensionless amplitude [105]:

$$a_p = \kappa A_p L_c \quad \text{and} \quad a_s = \kappa A_s L_c, \quad (4.3)$$

with the normalized length  $\xi = z/L_c$  and together with the Manley-Row relation [3]:

$$a_0^2 = a_p^2 + a_s^2, \quad (4.4)$$

where  $a_0$  is the total normalized amplitude, Eq. (4.2) can be transformed to [3]:

$$\frac{da_p}{d\xi} = a_0^2 - a_p(\xi)^2. \quad (4.5)$$

This differential equation has the solution [105]:

$$a_p(\xi) = a_0 \tanh(a_0(\xi - \xi_0)). \quad (4.6)$$

The parameter  $\xi_0$  is the constant of integration, which is defined later. The transformed form of Eq. (4.1), has in its turn, the solution [105]:

$$a_s(\xi) = a_0 \operatorname{sech}(a_0(\xi - \xi_0)). \quad (4.7)$$

### Single propagation through the crystal

In the following, the general behaviour of the two electric fields, when passing through the crystal once, is discussed. In Fig. 4.1, the square of the absolute values of these two functions for different crystal lengths are shown. The signal (red curve) builds up along the crystal and the pump (blue curve) decreases to zero at  $\xi = \xi_0$ . The dotted lines indicate the square of the absolute values of Eq. (4.6) and Eq. (4.7). For

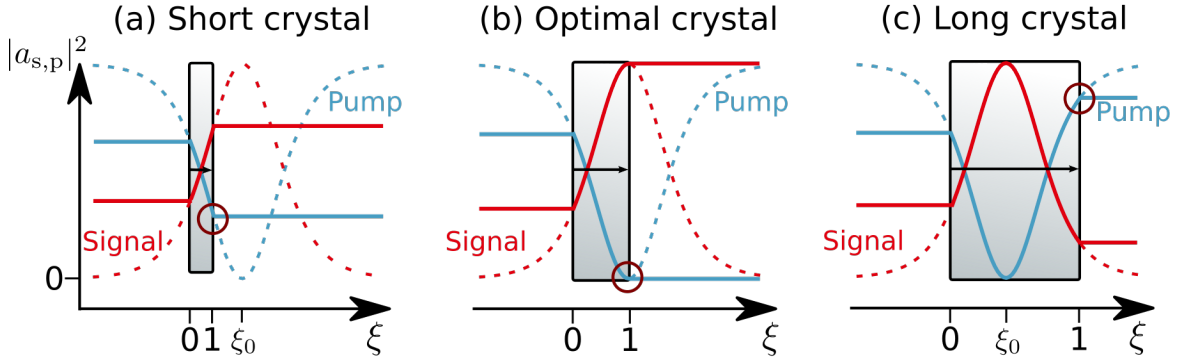


Figure 4.1: Change of pump  $|a_p|^2$  (blue) and signal  $|a_s|^2$  (red) when they propagate through the crystal. The dotted lines indicate the field amplitudes from Eq. (4.6) and (4.7) for infinite crystal lengths. The continuous line shows the transformation dynamics between an incident pump and signal for different crystal lengths (a-c). The state of the pump at the end of the crystal is shown in a red circle. (a) Conversion in the case when the crystal is too short, so that the pump is not fully converted to the signal. (b) The evolution for the optimal crystal length, where the pump is fully converted at the end of the crystal. (c) In a long crystal the pump is fully converted to the signal and significant back conversion takes place.

$\xi > \xi_0$  the nonlinear process converts the signal back into the pump. The fields exit the crystal at  $\xi = 1$ . For a given crystal length and the initial amplitudes  $|a_p|^2$  and  $|a_s|^2$ , a  $\xi_0$  can be defined [105]:

$$\xi_0 = \frac{1}{a_0} \operatorname{artanh} \left( \frac{a_p}{a_0} \right). \quad (4.8)$$

Depending on the initial  $a_p$ ,  $a_s$  and the length of the crystal, different situations can occur to the frequencies propagating through the crystal:

- **(a) short crystal length:** the pump has not been completely converted into the signal by the end of the crystal (see red circle in Fig. 4.1 (a)), but the signal is amplified.
- **(b) optimal length:** the pump is fully depleted at the end of the crystal. The signal leaves with maximum amplification.
- **(c) long crystal length:** the pump is fully depleted in the crystal and the signal begins to back convert into the pump. Depending on the initial conditions and the crystal length, the signal can be decreased or amplified.

### Steady state behaviour

The previous discussion is valid for a single propagation through the nonlinear media, but can be extended for a DROPO. Assuming the oscillator is running in a steady state, the gain of the nonlinear process is equal to the losses  $\alpha$  in the cavity [105]:

$$\operatorname{sech}(a_0(\xi - \xi_0)) = e^{-\alpha/2} \operatorname{sech}(a_0(1 - \xi_0)). \quad (4.9)$$

With Eq. (4.8), Eq. (4.9) can be rewritten as [105]:

$$\cosh a_0 - \frac{a_p}{a_0} \sinh a_0 - e^{-\alpha/2} = 0. \quad (4.10)$$

In this equation, the only unknown parameter is  $a_0$ , which can be solved numerically. Figure 4.2 shows an example solution of Eq. (4.10) for  $\alpha = 0.5$  and different  $a_p$ . On the ordinate, the resonant enhancement is presented, which is being defined as  $\eta = P_s/P_p = a_s^2/a_p^2$ , where  $P_s$  is the intracavity power of the DROPO and  $P_p$  is the

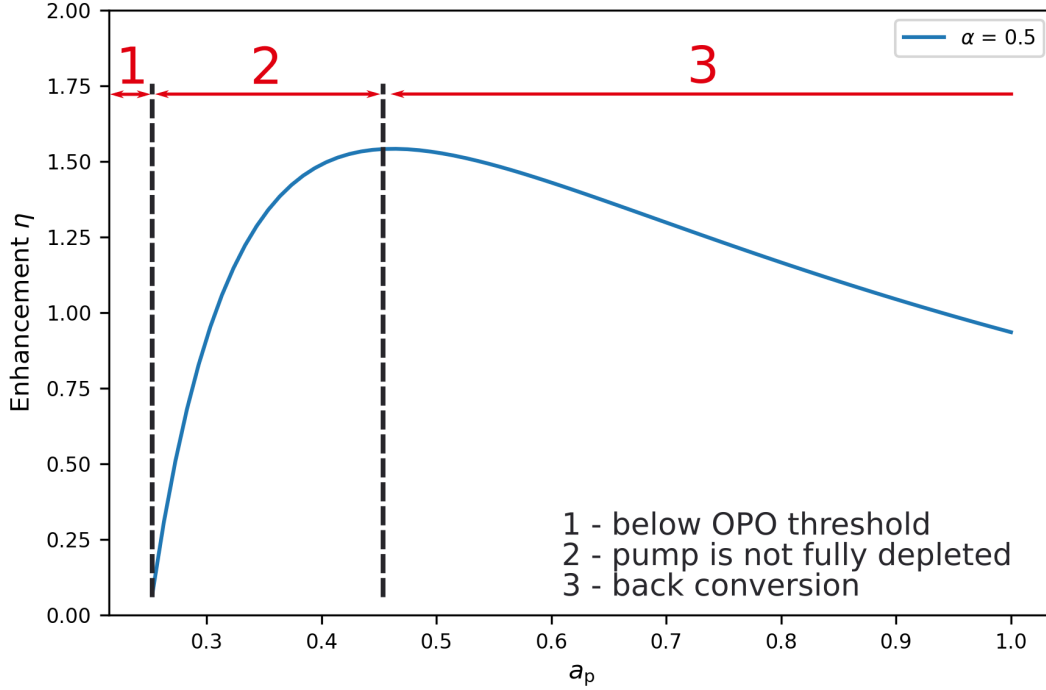


Figure 4.2: Solution of Eq. (4.10) for  $\alpha = 0.5$ . The enhancement  $\eta = a_s^2/a_p^2$  is nonlinear to the pump power. Three situations can be recognized: (1) below OPO threshold, (2) pump is not fully depleted and (3) back conversion takes place.

pump power. When  $a_p$  is increased, the enhancement shows a nonlinear behaviour. Three regimes can be recognized:

- (1) **below threshold:** The pump power is not high enough to get sufficient amplification
- (2) **pump is not fully depleted:** Similarly to the discussion for a single pass, the crystal size is too short, and the provided pump is not fully depleted in the crystal.
- (3) **back conversion:** for higher pump fields back conversion takes place, which limits the enhancement.

It can be seen that the enhancement can be higher than a factor of one, which shows that higher powers than the pump can be sustained in the DROPO.

For maximum enhancement  $\eta_{\max}$  an optimal  $a_{p,\max}$  can be found. Equation (4.10)

can be further simplified by expanding it into a power series up to the second order of  $a_0$ , which approximates the full description quite well around the maximum of enhancement. An analytical solution of  $a_0$  can then be found [105]:

$$a_0 = \sqrt{\frac{6(1 - a_p - e^{-\alpha/2})}{a_p - 3}}. \quad (4.11)$$

With  $e^{-\alpha/2} \approx 1 - \alpha/2$  and  $\partial\eta/\partial a_p = 0$  parameters can be calculated for the highest enhancement [105]:

$$a_{p,\max} = \kappa A_{p,\max} L = \alpha \quad (4.12)$$

$$a_{s,\max} = \kappa A_{s,\max} L = \sqrt{\alpha}, \quad (4.13)$$

which leads to [105]:

$$\eta_{\max} = a_{s,\max}^2 / a_{p,\max}^2 = 1/\alpha. \quad (4.14)$$

The equation means that by carefully balancing of the parameters, high enhancement factors in a DROPO are possible, similar to passive enhancement cavities.

### Inefficiencies due to spatial overlap of Gaussian beams

The theoretical model can be extended for Gaussian beams. The Rayleigh length for the beams ( $\approx 7$  mm) in the experimental setup of this thesis are longer than the crystal length, so that only the radial Gaussian spatial distribution in the crystal of the field can be taken into account, while the divergence of the beams is neglected. The parameter  $r$  is the radial coordinate of the beam and  $w_{p,s}$  the beam width. Analogous to the previous discussion, an  $a_{pr}$ ,  $a_{sr}$  and  $a_{0r}$  can be defined [106]:

$$a_{pr}(r) = a_p e^{-r^2/w_p^2} \quad (4.15)$$

$$a_{sr}(r) = a_s e^{-r^2/w_s^2} \quad (4.16)$$

$$a_{0r}(r) = \sqrt{a_p^2 \exp(-2r^2/w_p^2) + a_s^2 \exp(-2r^2/w_s^2)} \quad (4.17)$$

with  $r_{p,s} = r/\sqrt{2}/w_{p,s}$ . The beam radius  $w_{p,s}$  is the  $1/e$  radius and the factor of  $\sqrt{2}$  is the normalization of the mode. Equation (4.10) can be written as [106]:

$$f(a_{0r}(r)) = \cosh a_{0r} - \frac{a_{pr}}{a_{0r}} \sinh a_{0r} - e^{-\alpha/2}. \quad (4.18)$$

Since the DROPO cavity acts as a spatial filter, only the mode of the cavity will not be suppressed. This behaviour can be described by a projector  $P_c$  acting on Equation (4.18) [105]:

$$P_c(f(a_{0r}(r))) = \int_0^\infty r f(a_{0r}(r)) \exp(-r_s^2) = 0. \quad (4.19)$$

The function  $P_c(f(a_{0r}(r)))$  can be solved numerically for a given  $a_p$ ,  $w_p$ ,  $w_s$  and  $\alpha$ .

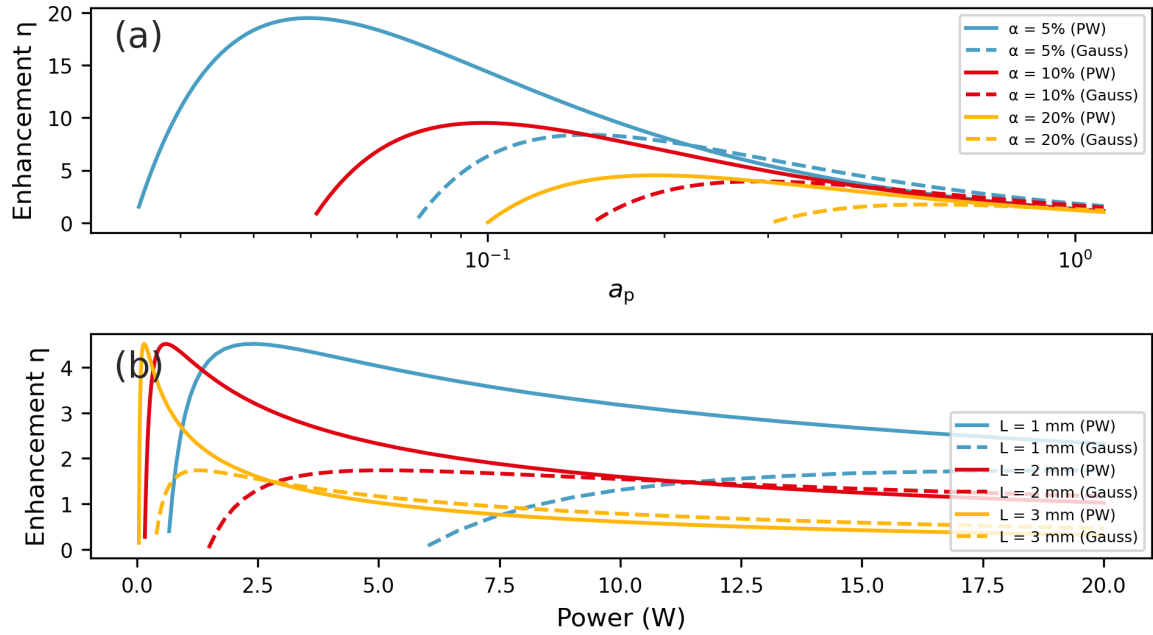


Figure 4.3: Results of the model for the plane wave (PW) and Gaussian approximation. (a) Dependence of the enhancement on the pump power for different losses. The maximum enhancement decreases and shifts to higher pump values in the case of higher losses. The dashed lines show the Gaussian approximation with  $w_s/w_p = 1/\sqrt{2}$ . The inefficiencies due to spatial overlap further reduce the enhancement. (b) The crystal length determines at which pump power the enhancement is the highest. For short crystals, this point shifts to higher pump powers.

In Fig. 4.3 the scaling of the enhancement is presented without (continuous lines) and with the spatial inefficiency (dotted lines), where  $w_s = 1/\sqrt{2}w_p$ . The two cases are called in the following the plane wave and Gaussian approximation. In Fig. 4.3 (a) the enhancement is presented for different overall losses of the cavity. For low pump amplitudes  $a_p$  no emission appears at all, because the DROPO is pumped below threshold. Above threshold, the enhancement factor increases strongly until it reaches a maximum. After this maximum, back conversion takes place and the enhancement is reduced. For higher losses, the magnitude of the maximum decreases and the location shifts to a higher  $a_p$ . The spatial mismatch, which is approximated by the Gaussian pump and signal distribution, lowers the total enhancement and shifts the maximum to higher pump power values. Figure 4.3 (a) illustrates that the total performance of the enhancement is mainly dependent on the losses, the spatial overlap mismatch of the pump and signal modes and  $a_p$ . When the losses and spatial mismatch are kept constant, the influence of different crystal lengths can be analysed. In Fig. 4.3 (b) it can be recognized that the maximum enhancement for all three calculated crystal lengths are equal. The curves reach their maximum at higher pump powers<sup>1</sup> for shorter crystal lengths. The shift indicates that the operation point of an experimental system can be tuned by the crystal length and the pump power. It shows that the pump intensity and the square of the crystal length are "exchangeable". For lower pump powers a longer crystal can be chosen in order to reach the highest possible enhancement.

### Pump depletion and efficiency

Besides the DROPO's output signal, the depleted pump is also insightful. To calculate the pump depletion  $D = P_D/P_0 = a_p^2(\xi = 1)/a_p^2(\xi = 0)$  for the linear case the Equations (4.9) and (4.6) can be used to determine the depleted pump in the steady state of the DROPO. The parameter  $P_0$  is the initial and  $P_D$  is the depleted pump. To calculate the inefficiencies of the Gaussian beams, Eq. (4.6) can be rewritten as [106]:

$$a_{pr}(\xi) = a_{0r} \tanh(a_{0r}(\xi - \xi_{0r})) \quad (4.20)$$

with

---

<sup>1</sup>In comparison to Fig. 4.3 (a), the abscissa is in the unit of power. Would it be scaled in  $a_p$  all PW (Gaussian) curves would overlap.

$$\xi_{0r} = \frac{1}{a_{0r}} \operatorname{artanh} \frac{a_{\text{pr}}(0)}{a_{0r}}. \quad (4.21)$$

The pump depletion can be then calculated by [106]:

$$D = \left| \frac{\int_0^{+\infty} r a_{\text{pr}}^2(\xi = 1) dr}{\int_0^{+\infty} r a_{\text{pr}}^2(0) dr} \right|. \quad (4.22)$$

With the depletion, the efficiency  $N = 1 - D$  of the conversion process from pump to signal can be defined. In Fig. 4.4 (a) the pump depletion and conversion efficiency  $N = 1 - D$  are shown for the  $\alpha = 10\%$  case of Fig. 4.3 (a) for the plane wave and Gaussian approximation. The efficiency is maximum (the depletion is zero) at the point, where the enhancement in Fig. 4.3 (a) is maximum. For the Gaussian beam model, the efficiency drops to lower maximum values and the maximum shifts to higher pump values. In Fig. 4.4 (b) the blue line shows that in the Gaussian beam approximation the efficiency drops or increases depending on the ratio of pump and signal mode. Here, the maximum of the efficiency is reached for roughly  $w_s/w_p > \sqrt{2}$ , similar to second harmonic generation [4]. It should be noted that [95] shows that for a more exact determination of the optimal focus ratio the birefringence has an influence on the performance of the nonlinear process, which is not included in the model here.

In summary, it was shown via a simple model that enhancement inside a DROPO similar to a passive cavity is possible. The model can be extended for Gaussian beams to show their impact on the system. Experimental measurements should be explainable by the model. The question here is how the different spatial and temporal effects in a DROPO affect the performance of such systems. The experimental performance will be shown in the next chapter.



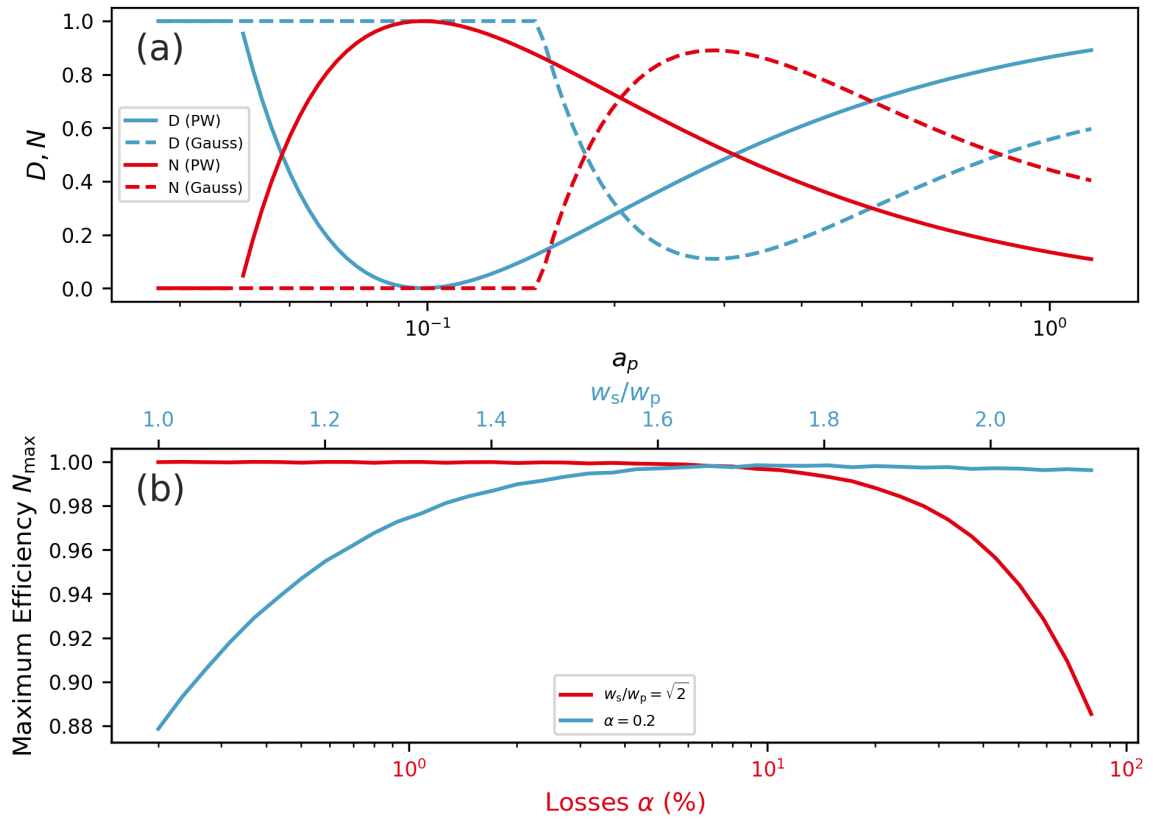


Figure 4.4: Results of the model for the plane wave (PW) and Gaussian approximation. (a) Pump depletion  $D$  and conversion efficiency  $N$  for the 10% loss case. The dashed line shows the Gaussian approximation for  $w_p = w_s$ . Here, the pump beam is not fully converted. (b) The maximum efficiency (blue line) for the Gaussian approximation in dependence of the mode size ratio (top x-axis) between signal and pump for a calculated loss of the cavity of  $\alpha = 0.2$ . The red line shows the dependence of the maximum efficiency in relation to the losses (bottom x-axis) for  $w_p/w_s = \sqrt{2}$ .

### 4.3 Experimental setup for enhancement measurements

For measuring the cavity enhancement factor, several parameters need to be controlled. In Fig. 4.5 the measurement setup is presented. Since the enhancement has a nonlinear dependence on the pump power, the pump is controlled by a motorized wave plate in combination with a thin-film polarizer. The resulting pump power is monitored with a calibrated photodiode, which is positioned behind an HR mirror. The intracavity signal is measured with a 0.5% OC. The parasitic SHG and any remaining pump light are filtered from the DROPO's output signal with a long pass filter (Thorlabs FEL1500).

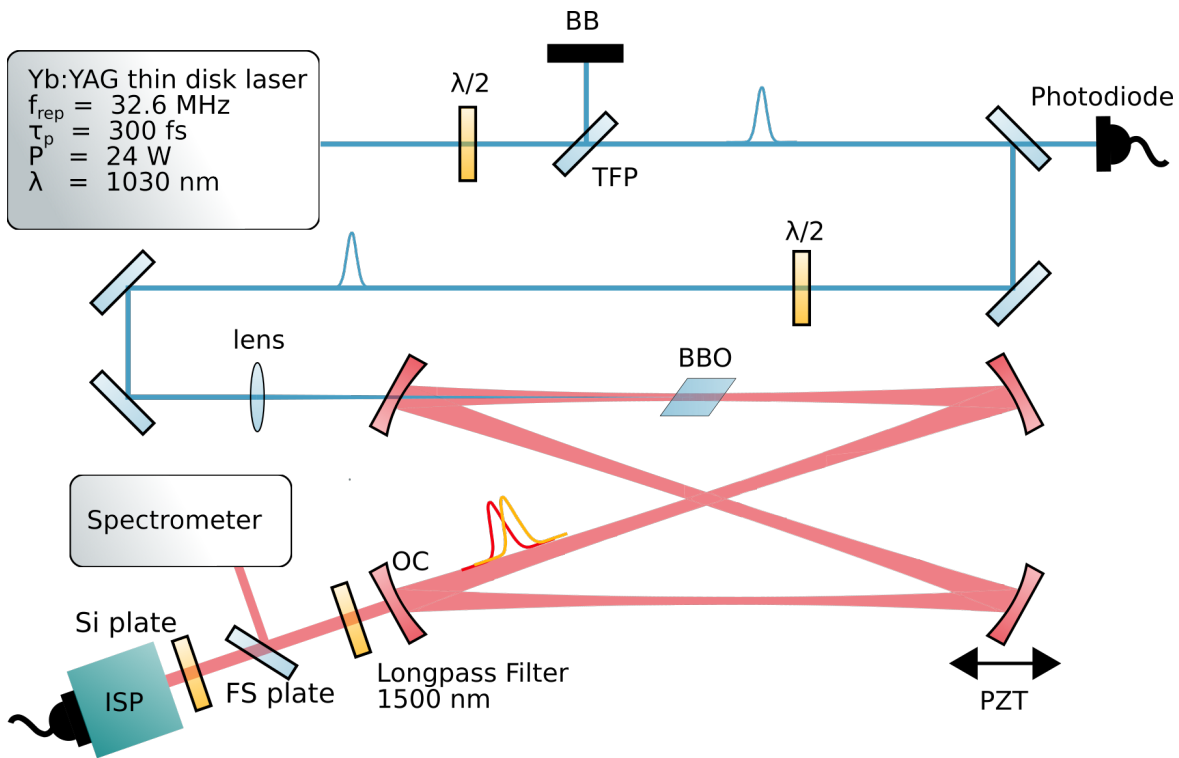


Figure 4.5: Experimental setup for measurements of the intracavity power in a DROPO. The output power is detected by a fast integrating sphere power meter (ISP) and the pump power is measured from the leakage behind an HR mirror. The pump power can be tuned by a motorized wave plate in combination with a thin film polarizer (TFP). The cavity length is controlled with a piezo translation stage (PZT).

A small part of the light is reflected by a fused silica plate and coupled into a spectrometer. The remaining light is measured by an integrating sphere power sensor (ISP), which is a calibrated combination of a FOIS-1 Ocean Optics Integrating Sphere and a fast extended InGaAs photodiode. The Fresnel reflections of silicon plates are used to block light away from the ISP so that it does not saturate. Since the full power no longer hits the detector, the transmissions of the optical substrates must be taken into account. It must be noted that the full pump power is not available for the nonlinear interaction, since there is a reflection of the s-polarized pump at the first surface of the BBO crystal. The transmission of all used optical substrates and surfaces is described in Tab. 4.1. For the validation of the theoretical considerations, additional losses in the

Table 4.1: Transmission of optical elements in the enhancement measurement setup.

Optical element	Transmission
BBO crystal (first surface)	84%
FEL1500	83%
FS plate	95%
Silicon plate	48%

cavity should be avoided. The dispersive optical plates which compensate the GDD are removed from the cavity for these measurements. The DROPO runs near to the zero GDD point, but with smaller losses. In Tab. 4.2, the intracavity GDD and TOD values for the DROPO cavity are presented for the different crystal sizes.

Table 4.2: Intracavity GDD and TOD of the DROPO cavity for different crystal lengths.

Crystal length (mm)	GDD (fs <sup>2</sup> )	TOD (fs <sup>3</sup> )
1	-131	+2088
2	-269	+3115
3	-406	+4142

## 4.4 Interplay of the crystal length and pump power

In Fig. 4.6 (a-c) the experimental results of the enhancement for 1 mm, 2 mm and 3 mm crystal length and an output coupler of 0.5% are shown. Their corresponding spectra are presented in Fig. 4.6 (d-f). The pump power is increased stepwise (ordinate) and several cavity lengths detuning resonances are measured (abscissa), where the DROPO runs with the highest efficiency, near the degenerated resonances. In the post-processing, the reflection on crystals, plates and filters are taken into account and the enhancement is calculated. It can be seen that  $\eta$  depends nonlinearly on the pump power. In Fig. 4.6 (a) for example, the enhancement first increases to a factor

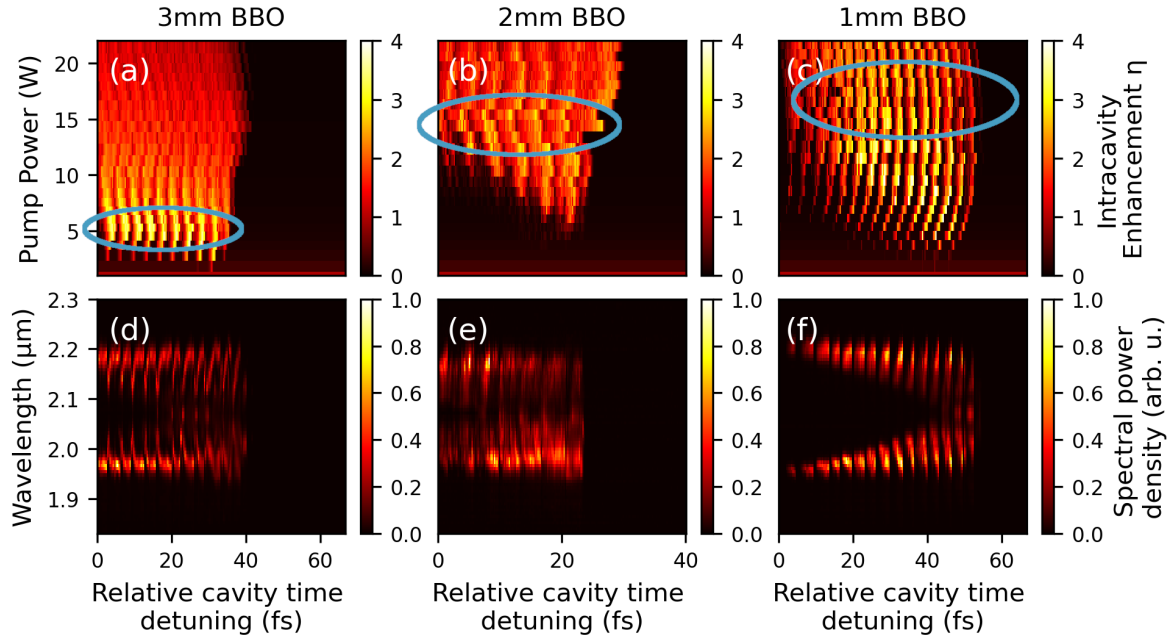


Figure 4.6: (a-c) Experimental measurements of the enhancement in the DROPO cavity for different crystal lengths (see also in [105]). The enhancement is measured with different pump powers and relative cavity length detunings with an OC of 0.5%. Depending on the pump power, the enhancement first increases to a maximum value and then decreases again. The thinner the crystal, the higher the intracavity powers that can be achieved. The maximum of enhancement is circled in blue. (d-e) Corresponding spectral behaviour when the cavity length is detuned. The spectrum is measured at a pump power of 12.5 W. Due to the non-compensated GDD, the resonances are slightly curved, defined by Eq. (3.4).

of four at 5 W and then decreases. In Fig. 4.6 (b-c)  $\eta$  is at the same magnitude even if the crystal length is reduced. However, the maximum enhancement (circled in blue) is moving to higher pump power values, as the crystal length decreases. It should be noted that the ISP detector of the DROPO radiation had a slight offset. As a consequence, the enhancement factor is higher than expected at pump powers below the DROPO threshold. The measurements show that the DROPO behaves similar to the previous discussed theoretical model. It can be seen that  $\eta_{\max}$  does not depend on the crystal length. With shorter crystals, higher powers can be confined in the cavity, as the point of highest enhancement shifts to higher pump powers (see Fig. 4.3 (b)). The highest measured intracavity power is around 75 W pumped by 20 W with the 1 mm crystal.

The experimental measurements can be examined more closely with Eq. (4.10) and (4.19). In the analysis of the experimental and simulated results it is necessary, to calculate back and forth between power, the normalized amplitude  $a_{p,s}$  and the intensity in the crystal  $I_{p,s}$ . The following equations are used [52]:

$$A_{p,s} = \frac{a_{p,s}}{\kappa L} \quad (4.23)$$

$$I_{p,s} = \frac{1}{2} cn\epsilon_0 A_{p,s}^2 \quad (4.24)$$

$$P_{\text{peak } p,s} = \frac{I_{p,s} \pi w_{p,s}^2}{2} \quad (4.25)$$

$$P_{p,s} = \frac{P_{\text{peak } p,s} \tau_{p,s} f_{\text{rep}}}{0.88}, \quad (4.26)$$

where  $n = 1.64$  the refractive index of the crystal,  $A_{p,s}$  is the real field amplitude,  $I_{p,s}$  the intensity,  $P_{\text{peak } p,s}$  the peak power and  $P_{p,s}$  the average power of pump and signal. The results in Fig. 4.6 can be reduced to a one dimensional array by determine the peak enhancement of each resonance and calculate the mean of them for different pump powers. The theoretically predicted enhancement for the three crystals is presented in Fig. 4.7 for the Gaussian and plane wave approximation (PW) (see Eq. (4.10) and (4.19)). The reduced model with a Gaussian spatial distribution can be fitted to the experimental data, when large beam waists radii are presumed. In Fig. 4.7, radii with around  $200 \mu\text{m} - 250 \mu\text{m}$  are chosen. The crystal's refractive index for pump and signal is  $n = 1.64$ . In Tab. 4.3 the other fitting parameters are presented. The plane wave approximation uses the same losses as the Gaussian model. In total, it can be seen

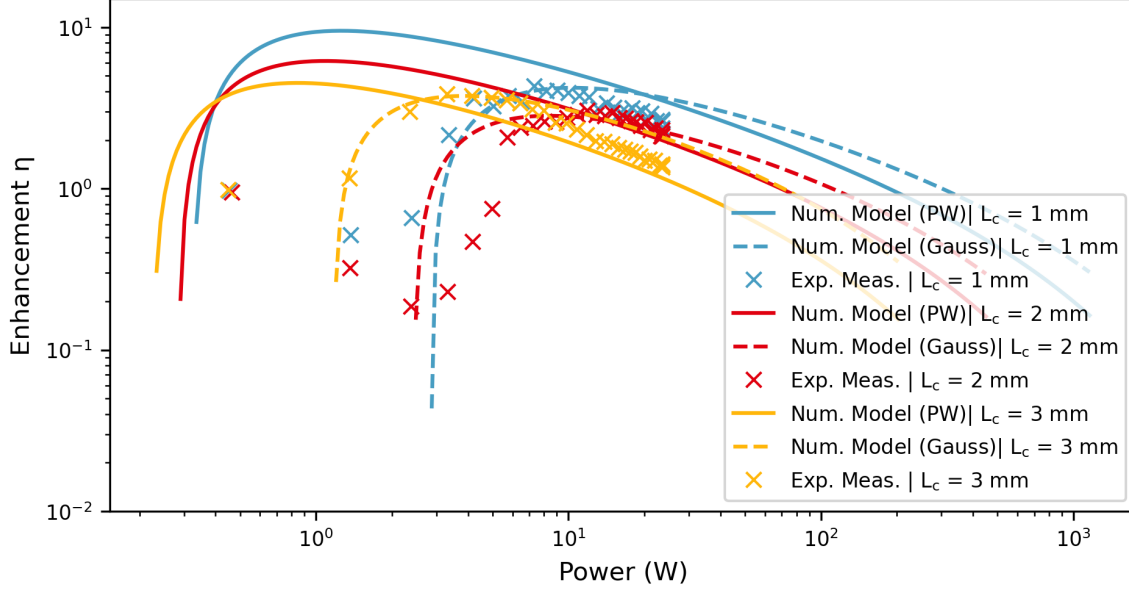


Figure 4.7: Fit of the reduced experimental measurements from Fig. 4.6 (crosses) with the iterative model, described in Section 4.2 (lines).

Table 4.3: Fitting parameters in Fig. 4.7

Crystal length (mm)	Pump beam radius ( $\mu\text{m}$ )	Mode ratio $w_s/w_p$	Losses $\alpha$
1	200	0.95	0.10
2	250	0.9	0.15
3	250	0.4	0.20

that the Gaussian approximation can be fitted quite well to the experimental data in comparison to the plane wave model. However, the mode ratio is altering strongly for the three measurements. The Gaussian model takes the losses and the possible mode mismatch into account but is not considering additional aspects in the crystal like temporal, spatial walk-offs and other dynamics. For thicker crystals, losses with  $\approx 5\%/mm$  (absolute value) need to be assumed, which also include the inefficiencies of the spatial and temporal mismatches. Additional losses can be explained by misalignment, the mirrors, humidity in the cavity and the output coupler. The quality of the nonlinear crystals can play a role, too. Since for every change of the crystal length, the cavity needs to be realigned, losses and mode diameters can vary for each mea-

surement. The high deviations from the model for small pump intensities are caused by the noise and a small offset of the detector.

With the split-step based numerical model, which is discussed in the previous chapters, enhancement tuning curves can be calculated, too. In comparison to the amplitude model, temporal effects and dispersion are taken into account, whereas spatial effects are neglected. With the model, the enhancement factor  $\eta$  can be calculated for different pump powers, cavity length detunings and dispersion configurations. In Fig. 4.8, the results for the split-step based model are presented. The cavity length detuning in these simulations is fixed to the strongest degenerated signal detuning resonance and the higher-order dispersion terms are adapted to the experimental values. In this model, large beam waists radii need to be presumed, and the losses are comparable to the previous reduced model. Pump beam waist radii of  $200\ \mu\text{m} - 450\ \mu\text{m}$  and losses around 15% are chosen to fit the model to the experimental values. The corresponding fit parameters are shown in Tab. 4.4. In comparison to the amplitude based model, the

Table 4.4: Fitting parameters in Fig. 4.8

Crystal length (mm)	Pump radius ( $\mu\text{m}$ )	$w_s/w_p$	$\alpha$
1	230	1.04	0.15
2	450	0.88	0.14
3	300	1.0	0.17

decrease of the enhancement in the back conversion regime is not so strong. Possible reasons are the temporal broadening of the signal pulses due to dispersion and the temporal walk-off in the crystal. Both models can be used for a first estimation of the possible experimental enhancement and can help in understanding the underlying scaling laws. For more accurate predictions, a temporal/spatial split-step based model like in [107] should be considered.

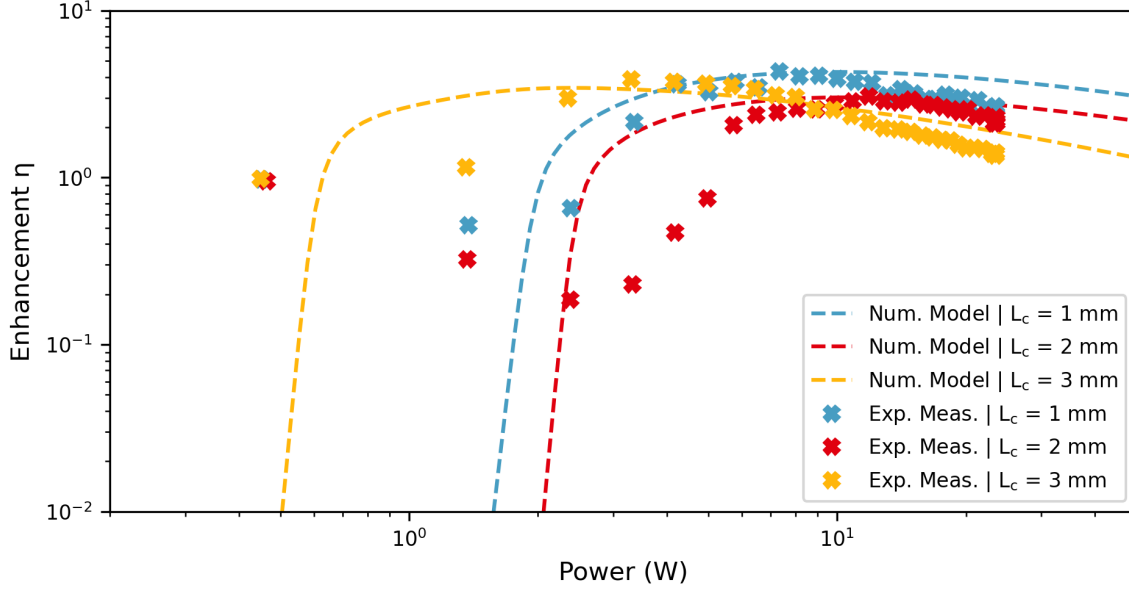


Figure 4.8: Fit of the reduced experimental measurements from Fig. 4.6 (crosses) with the split-step model, described in Chapter 2.6 (dotted lines). The fit parameters are presented in Tab. 4.4.

## 4.5 Influence of the GDD and TOD on the enhancement

The split-step based model can give additional insights on how the cavity dispersion affects the enhancement in the DROPO. In Fig. 4.9 (a) the spectral behaviour is simulated, when the cavity length is detuned. The parameters  $L_c = 1$  mm,  $\alpha = 20\%$ ,  $OC = 0.5\%$ ,  $w_{p,s} = 110$   $\mu\text{m}$ ,  $GDD = 0$   $\text{fs}^2$ ,  $P_{\text{pump}} = 20$  W and  $TOD = 12000$   $\text{fs}^3$  are used. To discuss different GDD and TOD values, the first degenerate resonance at zero GDD, after the non-degenerated ones is taken as the reference value (red circle in Fig. 4.9 (a)), which shows in general the highest enhancement values of the DROPO. The change of the temporal overlap between pump and signal can be here neglected, because only the GDD / TOD is altered, not the GD. In Fig. 4.9 (b) the maximum enhancement in dependence of the GDD with losses of  $\alpha = 10\%$  and  $20\%$  and a fixed TOD of  $12000$   $\text{fs}^3$  is presented. The maximum enhancement factor is relatively robust against GDD changes. At zero GDD the enhancement is the lowest and increases for non-zero values. The increase can be expected, since the pulses broaden in the



simulation due to the dispersion. It lowers the peak power, which results in less back conversion. Since the enhancement is defined in terms of power, it increases. Interesting is the steep rise of the enhancement near the zero GDD point. A possible explanation could be effects like solitons, which can appear in a DROPO [41]. In Fig. 4.9 (c) the GDD is fixed to zero and the TOD is increased. Here, the enhancement is robust to changes of the TOD. There is a slight increase for higher TOD, which can be explained with the broadening of the pulses for higher TOD values, too.

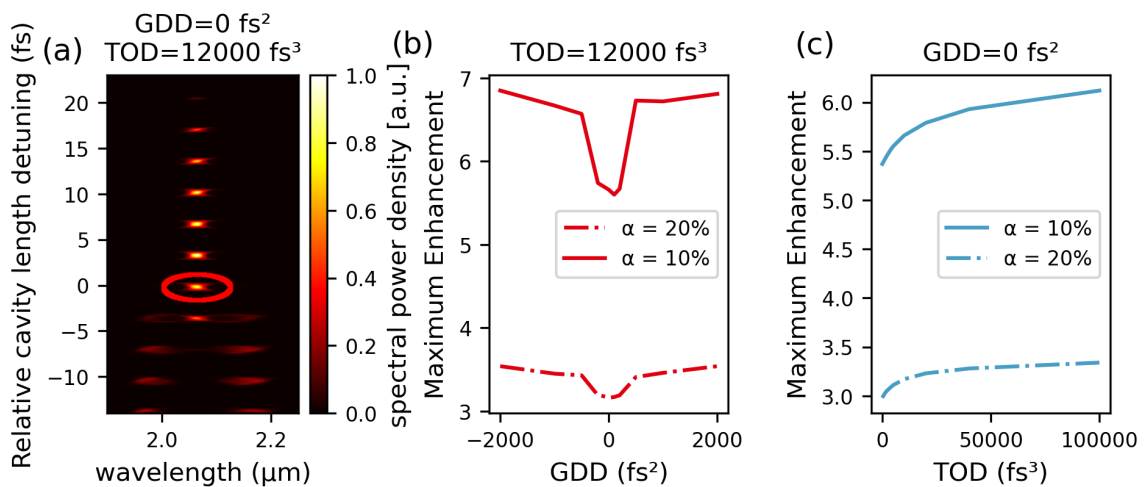


Figure 4.9: (a) Simulation of the split-step model from Chapter 2 with  $L_c = 1$  mm,  $\alpha = 20\%$ ,  $\text{OC} = 0.5\%$ ,  $w_{p,s} = 110$   $\mu\text{m}$ ,  $\text{GDD} = 0$   $\text{fs}^2$  and  $\text{TOD} = 12000$   $\text{fs}^3$ . For the discussion of the dependence of the GDD and TOD in (b) and (c), the circled resonance is chosen as an reference. (b) Dependence of the maximum enhancement on the GDD. When the GDD (red curves) is tuned, the TOD is fixed to 12000  $\text{fs}^3$ . At zero GDD, the enhancement slightly decreases, due to shorter pulses. (c) When the TOD is varied, the GDD is set to zero. The enhancement increases slightly for higher TOD values.

## 4.6 DROPO detuning resonance width in dependence of the losses

When a DROPO runs with low losses, the width of the DROPO detuning resonances is decreased. This can have an impact on the stability of the system, when high

enhancement should be achieved. In Chapter 2.5 the sensitivity of the nonlinear process to cavity length changes is derived:

$$\Delta L = \frac{\lambda_s(\alpha + \alpha_{OC})}{4\pi} \sqrt{r_p - 1}. \quad (4.27)$$

The maximum detuning length on one resonance  $\Delta L$  and the pump parameter  $r_p = P/P_{th}$  for a known  $\alpha_{OC}$  can be measured experimentally, while the losses  $\alpha$  can be used as a fitting parameter.  $P$  is the pump power and  $P_{th}$  is the pump power at threshold.

To examine the detuning length  $\Delta L$ , the DROPO is used in the zero GDD configuration with a 3 mm crystal and 2 mm ZnSe. The output power with a 0.5% and 30% OC is measured with a photodiode in combination with a 15 MHz low pass filter. To vary the DROPO's cavity length, the PT130.20 piezo tube is used in combination with an electric function generator. A  $U = 20$  V sawtooth signal with a frequency of 200 Hz is applied to the piezo. The power of the first degenerated detuning resonance next to the non-degenerated ones is measured on the oscilloscope. With the theoretical piezo length change of  $L = 18 \frac{\text{nm}}{\text{V}} \cdot U$  the cavity detuning can be calculated. The pump power is measured by a power meter before the crystal. With the DROPO threshold of 3.3 W and 0.7 W for a 30% and 0.5% OC, respectively, the change of the detuning FWHM can be observed and is presented in Fig. 4.10. The dependence of the resonance width from the losses of the cavity is clearly visible. Also, the increase of the width with higher pump powers can be shown. Since the DROPO is unstabilized strong fluctuation of the peaks in terms of width and position are appearing, which increases the uncertainty of the measured data. Equation (4.27) has been fitted to the resonance widths and the internal losses  $\alpha$  are used as the only fitting parameter. As a result internal losses of 8% and 13% are found, which corresponds to the expectations. The difference between the two values can be explained by alignment errors, when the OC is changed. This kind of error is difficult to quantify, but can be estimated at 5% to 10%. It can be noted, if the DROPO runs with high finesse factors for reaching high intracavity enhancements that more effort and attention must be paid to the stabilization scheme of the system. An example for a stabilization is presented in the next chapter.

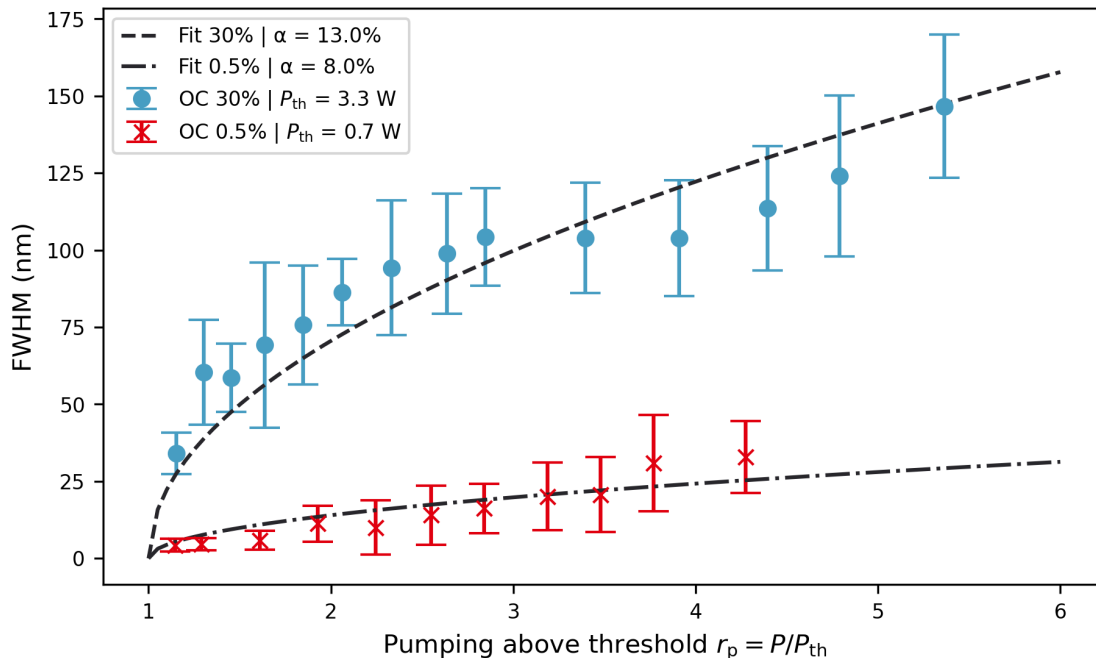


Figure 4.10: Experimental measurements of the detuning resonance width in dependence of the pumping above threshold  $P/P_{th}$ . With higher output coupling and pumping the width of the detuning resonances increases. Equation (4.27) has been fitted to the data. The internal losses of the cavity add up to around 8% and 13%.

## 4.7 Conclusion

In this chapter, the enhancement of strong fields inside a DROPO was analyzed. An analytical model of the DROPO was introduced and the main limiting factors, namely losses and back conversion were discussed. Measurements with different crystal lengths are presented and the back conversion effects at high pump powers were compared to the numerical models. The split-step model from Chapter 2.6 was used to estimate possible effects from the GDD and TOD. Lastly, the detuning resonance width in dependence of the pump power and output coupler was shown.

The experimental measurements and theoretical models show that high enhancement factors are possible in DROPOs and the upper limit is mainly given by the losses in the system and insufficient pump/signal spatial overlap. With the presented models, possible working points for future DROPO systems can be calculated. The small line

---

width of a couple of 10 nm of the DROPO's resonances leads to the necessity of an active stabilization scheme, which locks the DROPO on one of its resonances.



# Chapter 5

## Dither free stabilization

The previous chapters showed that the DROPO only emits light, when the cavity length is aligned by a few hundreds of nanometers. To stabilize this system, a dither free locking scheme for the DROPO in this thesis is presented. In the first part, theoretical and technical aspects of the stabilization are shown. The performance of the stabilized system is examined and the self-phase locking is presented. Parts of the experimental results have been published in [108, 75, 109].

### 5.1 Introduction

The DROPO shows strong changes in its output power and optical spectrum, when the cavity length is detuned (see Chapter 3). Due to environmental disturbances, which effect the cavity length, one can observe fluctuations of the output power and output spectrum. In this state, the system is nearly unusable for applications. To have a stable system in its output characteristics, an active stabilization scheme has to be applied. Often dither locked methods are used [65, 110, 111]. For this locking technique, the cavity length of the DROPO is periodically altered close to a detuning resonance. The output power is measured and then is multiplied with the dither frequency, followed by a low-pass filter. The resulting feedback function can be used for the stabilization with a PI (**P**roportional, **I**ntegration) controller. By modulating the cavity length with the dither frequency, additional resonances can occur, which limit the performance. On the other hand, dither free stabilization schemes, which use the parasitic SHG

or sum frequency (SF) mixing of the signal and pump were recently demonstrated [112, 44]. The publications indicate that the performance of these schemes are similar or even better than dither locked systems. During operation, in DROPO systems, often parasitic SFG is generated. When the cavity length of DROPO is slightly changed, differences of the optical spectrum of the SFG can be observed. The SFG signal can be filtered with a spectral filter and be used as a feedback function for an active stabilization. For the thin disk pumped DROPO presented in this thesis it was not exactly clear, if the SF signal can be used for this type of stabilization scheme. This chapter answers this open questions, and inspired by [44] a locking scheme based on the parasitic SFG is presented for the thin disk pumped DROPO.

## 5.2 Proportional-integral controller

A proportional-integral (PI) controller can actively stabilizes a system, based on a feedback signal. The controller influences the system with the controlled signal  $c(t)$  in such a way that a specified set point  $r_s$  of the controlled signal is maintained. The feedback or error function can be defined as  $e(t) = c(t) - r_s$  [113, 114]. The PI controller can be mathematically described by [113]:

$$u(t) = K_P e(t) + K_I \int e(t) dt. \quad (5.1)$$

Here,  $u(t)$  is the manipulated or control variable [114], which affects the system. The variable  $K_P$  and  $K_I$  are the characteristic parameters of the controller. The equation can be split into a P-part  $m_P$  and I-part  $m_I$ :

$$m_P(t) = K_P e(t) \quad (5.2)$$

$$m_I(t) = K_I \int e(t) dt \quad (5.3)$$

The P part works in general as an amplifier of  $e(t)$  with the amplification of  $K_P$ . It counteracts changes away from the set point. The P-part cannot stabilize the system exactly on the set point and an offset remains [113]. To overcome this issue, the I part is necessary, which integrates the error function with respect to the time. The I-part, with the constant  $K_I$ , stabilize the system to the absolute set point  $r_s$ .

A derivative part (D-part) could also be realised. From experience, the D-part is not always necessary and a P- and I-part is usually sufficient for common laser systems. However, the D-part can increase slightly the performance, but can amplify unwanted higher frequencies. The D-part is not used in this system to decrease possible noise induced by the controller, with the drawback that the system is more sensitive to shocks or sudden changes. A more detailed introduction for PI(D) controller is given in [113, 114].

The concept of the PI controller can be applied to the DROPO system. In Figure 5.1 a DROPO resonance is shown schematically (blue line). To generate maximum output power, the cavity length needs to be stabilized with the PI controller over time. The cavity length can be seen as the manipulated variable  $u(t)$ . The SF signal can be used to stabilize the system, if the overall SF signal power has a gradient where the DROPO signal power is maximum, when the cavity length is detuned. The SFG signal can then be used as a controlled signal  $c(t)$ . With the set point  $r_s$ , the DROPO can be adjusted to its maximum. The PI controller corrects fluctuations away from the set point and changes the cavity length so that  $e(t) = c(t) - r_s = 0$ .

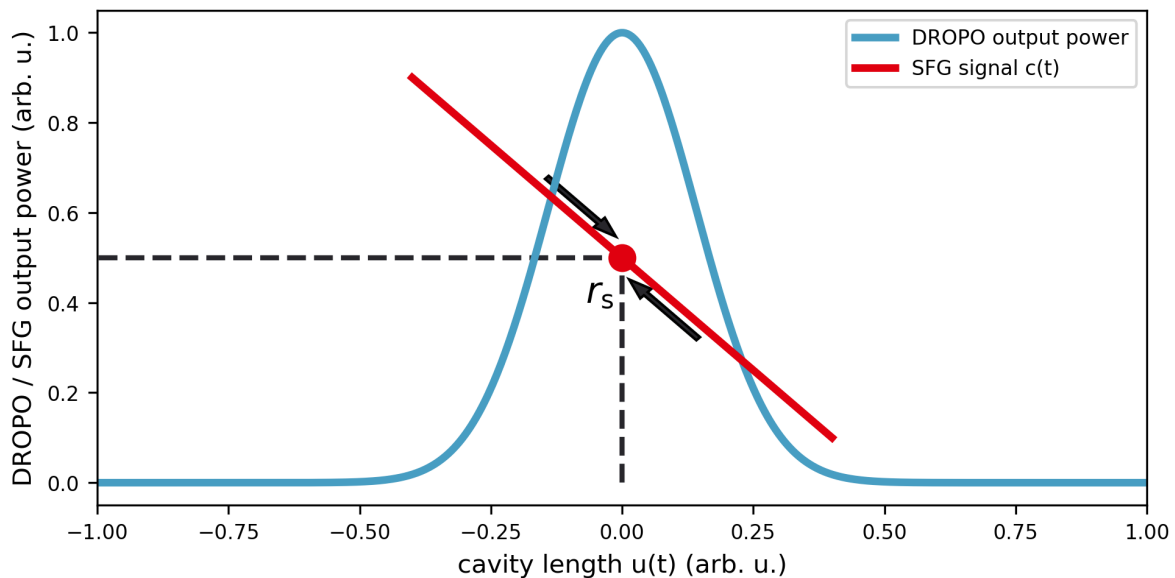


Figure 5.1: Schematic explanation of the connection of the DROPO resonance (blue) and the SFG output (red). The PI controller alters the cavity length, so that  $e(t) = 0$ . Here, the set point is chosen so that the DROPOs output power is maximum.



### 5.3 Numerical simulation of sum frequency generation

In reference [44], it has been shown that by correctly filtering the spectral components of the SF signal between the pump and the DROPO's signal wavelength, a feedback signal suitable for a PI controller, as described in the previous chapter, can be generated. For a first examination, the filtered SF signal can be simulated with the split-step based numerical model from Chapter 2.6. After the signal passed several roundtrips in the simulated cavity, it is multiplied by a non-depleted pump pulse at the end of the nonlinear crystal:

$$A_{\text{SFG}}(z, t) \propto A_{\text{s,i}}(z, t)A_{\text{p}}(z, t), \quad (5.4)$$

where  $A_{\text{SFG}}$ ,  $A_{\text{s,i}}$ ,  $A_{\text{p}}$  are the complex field amplitudes of the SF signal, the DROPO's signal/idler and pump. The result is an approximation of a fully simulated SF signal, but without the SF signal's dispersive and dynamical effects of the crystal propagation. The absolute amplitude can be not given, due to lack of inclusion of phase-matching and non-linearity, but it can be compared with the DROPO's signal power. In Fig. 5.2 (a) the simulation of the spectral response of the SF signal is shown in dependence of the cavity length detuning. A small shift to longer wavelengths and a spectral broadening for higher cavity length detunings can be recognized in the SF signal. In Appendix A.3 another example with a 4 mm crystal is presented, where this effect is stronger visible. It is caused by the different temporal overlap between the DROPO signal and pump pulse in the crystal, depending on the cavity length and the pump power. The asymmetry in the simulation is robust against changes of the cavity and crystal dispersion. The shift and broadening of the SF signal spectrum can be simulated, however an intuitive explanation of the origin of the DROPO's behaviour is not found yet. A rectangular filter function can be used to simulate the influence of the bandpass filter in the experiment. With the filter, only specific optical frequencies of the SF light can be transmitted, which allow altering the final shape of the SF power detuning response. The applied bandpass filter borders for an optimal configuration are indicated as blue lines. Figure 5.2 (b) shows the resulting detuning behaviour of the DROPO signal power and filtered SF signal power when the cavity is detuned. A slope (yellow line) of the SF signal, where the DROPO signal is maximum, can be recognized. The SF signal can be used as the controlled signal  $c(t)$ . It can be stabilized

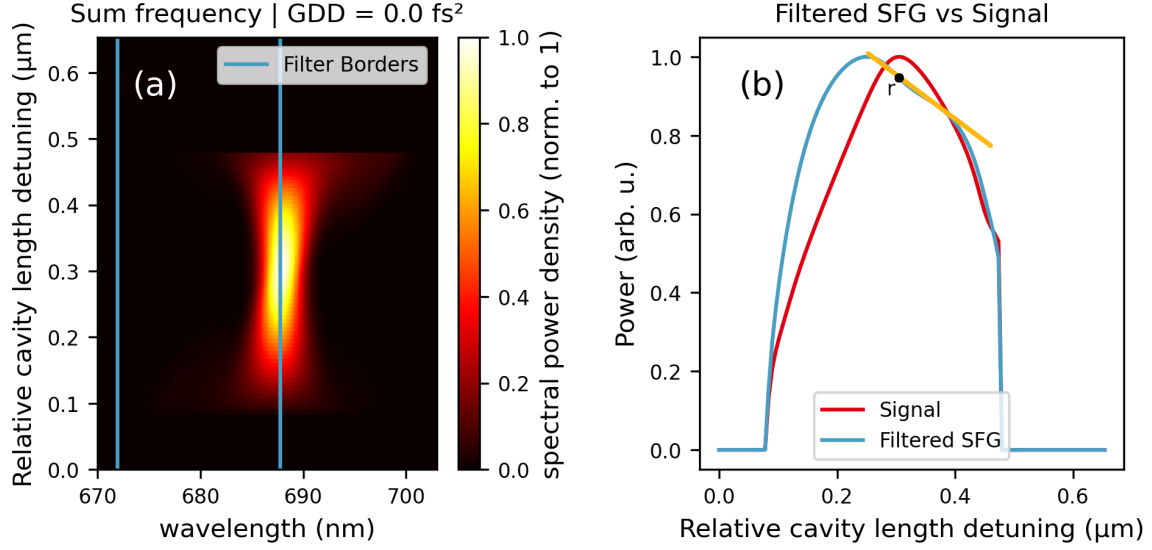


Figure 5.2: Simulation of the SF signal of one detuning resonance at the zero GDD point and a crystal length of 3 mm. (a) Spectral behaviour in dependence of the SF signal. The simulated bandpass filter is indicated by the two blue lines, which show the borders of the filter. (b) Simulated filtered SF signal and DROPO signal power in dependence of the cavity length detuning. The slope (yellow line) of the SF signal can be used as the feedback signal.

to a specific set point  $r$  with a PI controller. In this example, the GDD is set to zero. In Appendix A.4 examples for positive, zero and negative GDD are presented. It can be recognized that the GDD does not have a significant impact on the resulting slopes in the simulations.

## 5.4 Stabilization setup

In the following, the experimental setup is presented. The SFG is generated as a parasitic process in the nonlinear crystal between pump and signal of the DROPO with the wavelengths

$$2060 \text{ nm} + 1030 \text{ nm} \hat{=} 686.7 \text{ nm}. \quad (5.5)$$

The SFG phase-matching angle of  $20^\circ$  is near to the DFG at degeneracy ( $21.4^\circ$ ), but the acceptance bandwidth is too narrow for efficient phase-matching. The SF signal which is generated, is poorly phase-matched. In Fig. 5.3, the experimental setup for the stabilization scheme is displayed. The DROPO is configured to operate in the zero dispersion point with a 1 mm ZnSe plate and a 20% OC. A 2 mm BBO crystal is

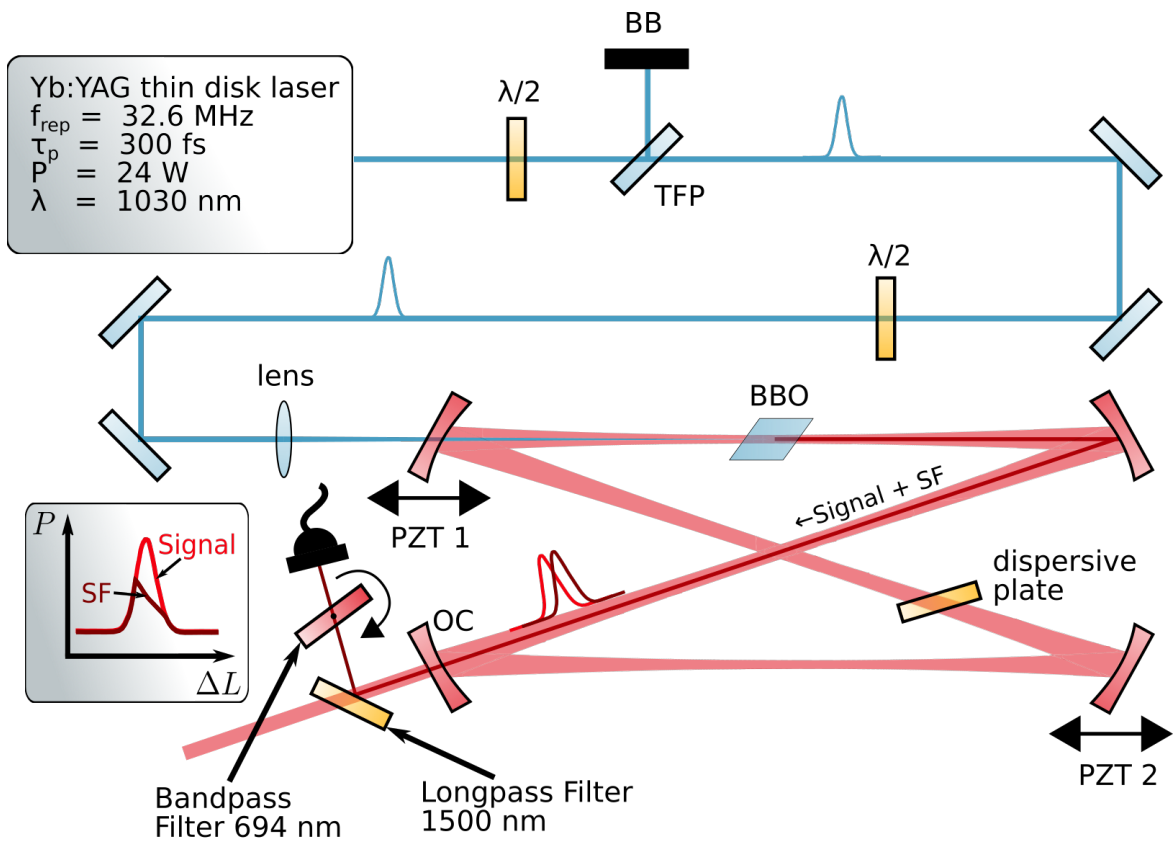


Figure 5.3: Experimental setup: Measurement of the SF signal (dark red) for the active stabilization of the system. The SF signal is generated in the crystal and partly reflected by the HR mirrors. It is separated from the signal by a long pass filter. By rotating a bandpass filter to transmit the spectral components around 695 nm a suitable error signal can be obtained. The transmitted power of this SFG signal shows a slope when the cavity length  $\Delta L$  is detuned (see inset scheme). A silicon photodiode detects the filtered SF light as input for the PI controller. The controller stabilizes the cavity with two piezo actuators inside the DROPO (PZT 1 and 2).

positioned in the 70  $\mu\text{m}$  cavity focus and is pumped by the thin disk laser. The sum frequency signal (dark red line in Fig. 5.3), which is generated in the nonlinear crystal, is partly reflected by the 2  $\mu\text{m}$  HR mirrors and is detected behind the OC. A Thorlabs FEL1500 long pass filter with a cut-on wavelength of 1500 nm is used to separate the SF signal and DROPO's signal wavelength. The reflected sum frequency is filtered by a bandpass filter (Thorlabs FB700-10) with a central wavelength of  $(700 \pm 2)$  nm and a FWHM of  $(10 \pm 2)$  nm. The transmission wavelength of a dichroic filter with an angle of incidence  $\delta$  can be approximately described by [115]:

$$\lambda = \lambda_0 \sqrt{1 - \alpha_d \sin^2(\delta)}, \quad (5.6)$$

where  $\lambda_0$  is the given central wavelength and  $\alpha_d$  is a type specific constant. The spectrum of the SFG can be filtered continuously by rotating the filter. In Fig. 5.4 the transmission of the used optical filter (Thorlabs FB700-10) is presented for different filter angles. The filter is irradiated with a white light source (NKT Photonics SuperK EVO) and the transmitted light is coupled in a spectrometer (Ocean Optics HR2000). It can be seen that the central wavelength is around  $\lambda_0 = 709$  nm at zero AOI and that the transmission shifts to smaller wavelengths, when the filter is rotated. Equation 5.6 is shown as a dotted blue line. The optimal overlap can be found, when  $\alpha_d = 0.9$ . The angle of incidence  $\delta$  is set in a way that the SF signal detuning resonance has a slope, similar it is simulated in Fig. 5.2, while the DROPO signal/idler resonance has at this cavity length its maximum. The SF signal is detected by a silicon photo diode and coupled in the electrical circuit of the PI-Controller as the controlled signal. The circuit diagram of the PI controller can be found in the Appendix B.

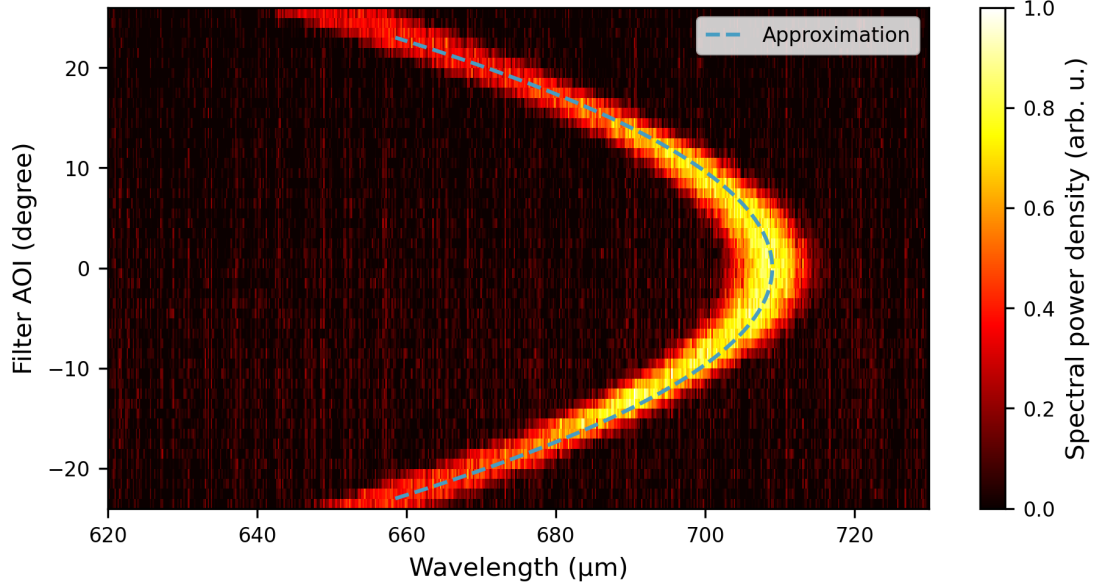


Figure 5.4: Spectral transmission of the Thorlabs FB700-10 bandpass filter, when the filter is tilted. The spectrum is measured with a white light source (NKT Photonics SuperK EVO) and a spectrometer (Ocean Optics HR2000). A change of the central transmission wavelength to lower wavelengths for higher filter AOI is visible.

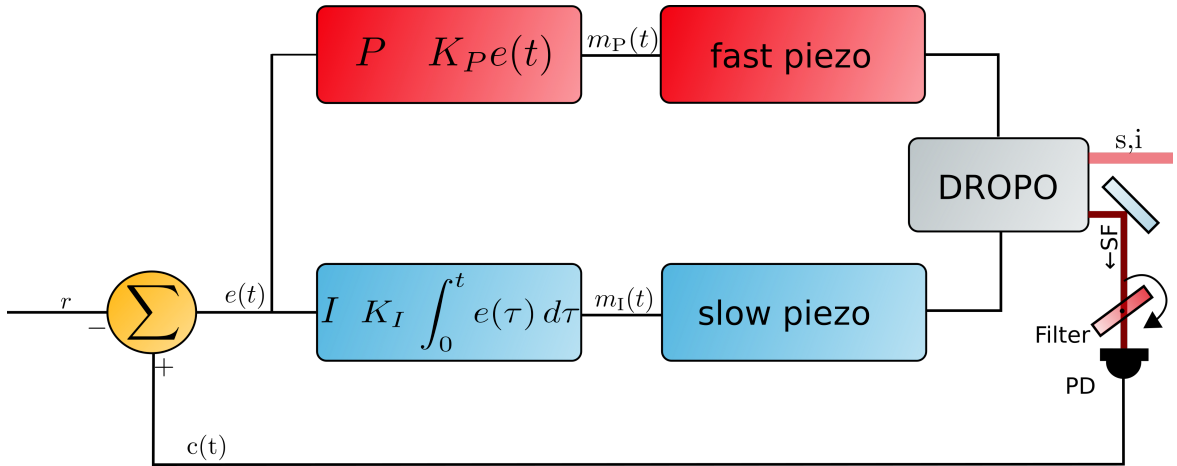


Figure 5.5: Stabilization scheme of the PI controller. After amplification of the error signal  $e(t)$  the signal is split in two electronic branches, one for the P-part and one for the I-part. The P-part moves a fast piezo ceramic tube, while the I part is controlling a slower piezo system (piezosystem jena TRITOR 100), which can cover a larger detuning range. The DROPO output can be tuned with the setpoint  $r$  in power.

In 5.5 a schematic overview of the PI controller is shown. For the stabilization, two piezo systems were used separately for the I- and P-part. A slow piezo actuator (piezosystem jena TRITOR 100) has a tuning range up to 160  $\mu\text{m}$ , but can only be modulated with a frequency up to approximately 20 Hz. This piezo system is controlled by the I-part, which can correct long term drifts of the cavity. For fast modulation up to 10 kHz, a piezo tube (PT130.20 Physik Instrumente (PI) GmbH & Co. KG) is used. This piezo is connected to the P-part. The piezo can support a maximum axial contraction of 360 nm in this setup. The upper limit of the modulation frequencies is given by its internal resonances, which are around 10 kHz. The resonances depend on the mechanical parameters, how the mirror is attached to the piezo tube, the weight of the HR mirror etc.

## 5.5 Experimental characterization of the sum frequency generation

The resulting SF signal needs to be characterized if it is suitable for the stabilization scheme. Similar to the simulation, the filtered SF signal needs to show an asymmetric spectral shift, or broadening, when the cavity length is changed. In Fig. 5.6, the optical spectrum of the unfiltered SF signal and the DROPO signal are measured simultaneously, in dependence of the cavity length. The SF signal spectral response is similar to the signal spectrum, only in a different wavelength regime. In Fig. 5.7 the degenerated resonance at 0  $\mu\text{m}$  cavity length detuning of Fig. 5.6 is closer examined. The DROPOs signal (a,d,g,j), the filtered SF signal for different filter AOI (b,e,h,k) and the measured power of the two (c,f,i,l) are presented. The DROPO's signal spectrum and the filtered SF signal are measured simultaneously with two spectrometer (Ocean Optics NIRQUEST256 and Ocean Optics HR2000). By modulating the cavity length with an electric function generator and the fast piezo actuator (PT130.20), the DROPOs output power and the SF signal is measured by fast photodiodes (extended InGaAs and silicon). In Fig. 5.7 (a,d,g,j) it can be seen that the measurements of the signal resonance slightly alters, because of fluctuations of the DROPO. In Fig. 5.7 (b) the filtered SF signal is presented, when the filter is in the position to transmit the maximum of SF power. Here, the influence of the filter is the lowest. The dotted blue lines show the estimated FWHM of the filter, which has approximately a Gaussian-shaped

transmission characteristic. It is clearly visible that the optical spectrum widens towards higher cavity length detunings, similar to the presented simulation. However, the spectral shift of the central frequency is not recognisable, due to the low resolution of the spectrometer. It can be seen in Fig. 5.7 (c) that the maximum of output power of the DROPO is approximately in the middle of the resonance for the DROPO's and SF signal. Small differences between the two signals are visible, which are caused by the interplay of pump and signal in the nonlinear crystal, when the SF signal is generated. In Fig. 5.7 (e,h,k) the filter is rotated that it blocks the lower wavelengths of the spectrum. Due to the asymmetry of the spectral detuning behaviour, the length detunings with a broader optical spectrum (around  $0.1\ \mu\text{m}$  cavity detuning) are clipped lesser. This results in a shift of the maximum filtered SF power to longer cavity length detunings, which can be seen in Fig. 5.7 (f,i,l). Especially in Fig. 5.7 (i) at a filter AOI of  $8^\circ$  the SF signal shows the expected slope (yellow line), where the DROPO's signal is maximum. The SF signal can be used as a controlled signal  $c(t)$  for the feedback loop. In this setup for smaller filter AOI below  $8^\circ$  the SF signal power is getting weaker and discontinuous, which limits the usability for stabilization in this filter configuration.

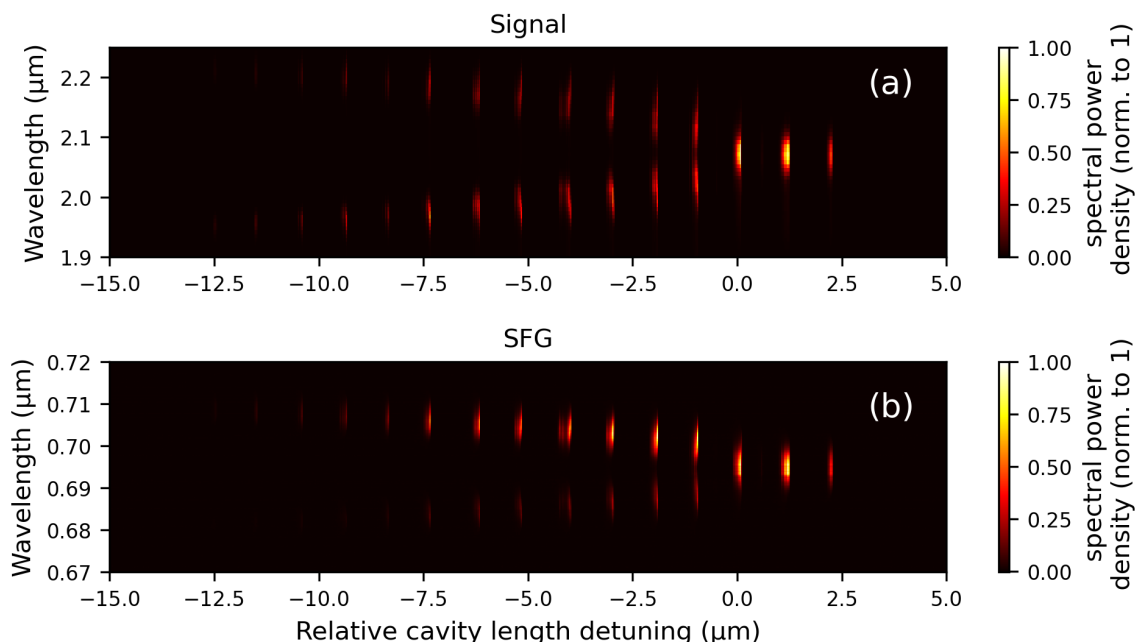


Figure 5.6: (a) Optical spectrum of the DROPO around the degeneracy when the cavity length is detuned. (b) SFG optical spectrum.

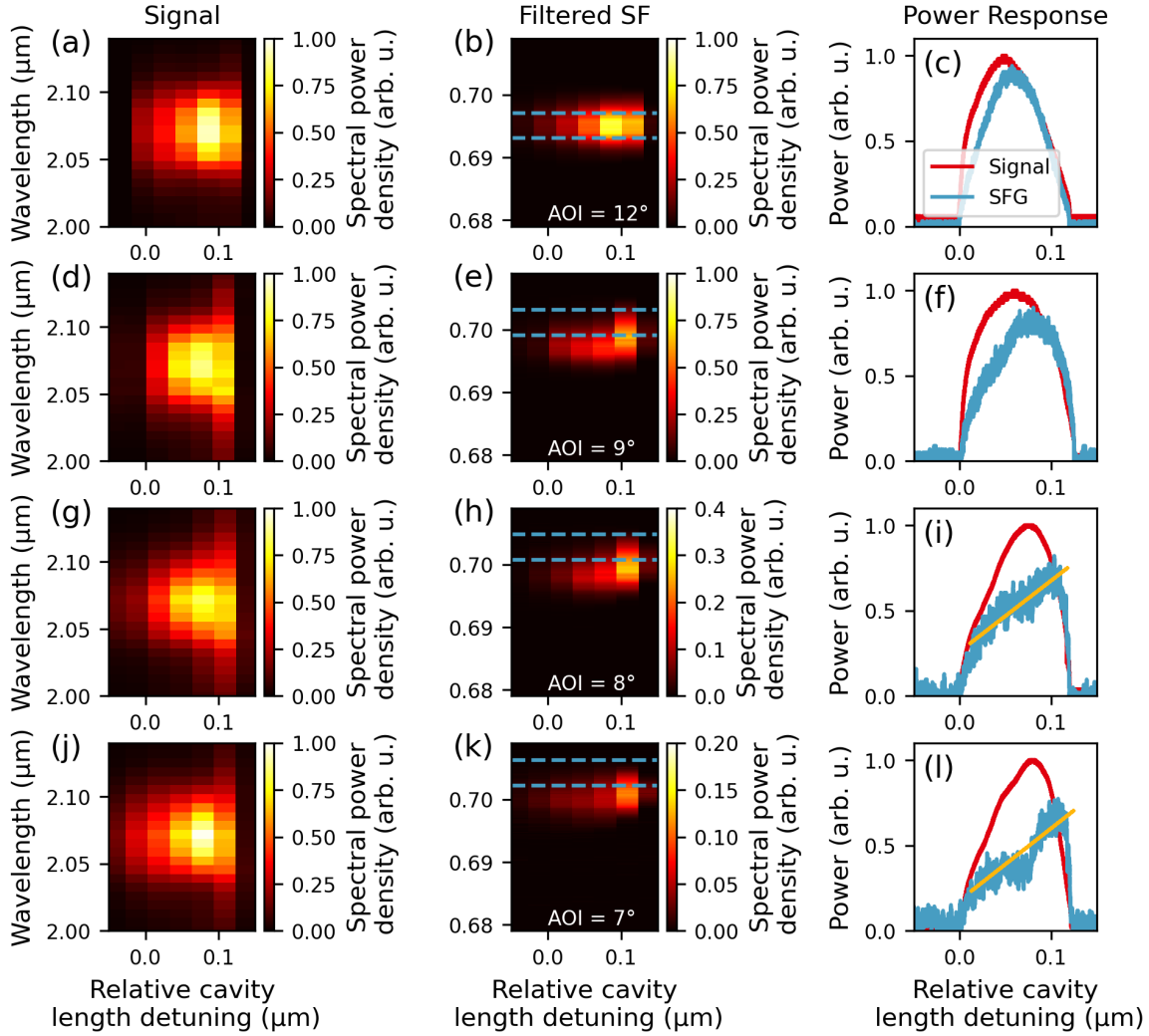


Figure 5.7: (a,d,g,j) Optical spectrum of the DROPO resonance in Fig. 5.6 at  $0 \mu\text{m}$  cavity length detuning. (b,e,h,k) Corresponding filtered SF signal for different filter AOI. The borders of the bandpass filter are marked in dotted blue lines. (c,f,i,l) Measured output power of the DROPO's signal (red) and the SF signal (blue). With optimal filtering, the SF signal shows a slope (yellow line), which can be used as a feedback signal (i,l).



## 5.6 Performance of the Stabilization

First, various passive stabilization measures were carried out, such as checking electrical noise, as well as reducing vibrations. These are explained in more detail in C.2.

For alignment of the active PI stabilization, different possibilities can be used. In order to increase the stability, the factors  $K_P$  and  $K_I$  in Eq. (5.1) need to be adapted, which can be done in the PI electrical circuit. The influence can be checked by the noise characteristics of the DROPO. When the two parameters are increased, at some point, the PI controller begins to overshoot the set point. Oscillations in the DROPO's signal take place. Experience shows that a stable condition is obtained if the parameters are then reduced to 75% of the value, when first oscillations occur.

For a better analysis, the experimental results are scaled in relative intensity noise (RIN) and the cumulative RIN, which is given in percent. A noisy signal  $P(t)$  can be described by [116]:

$$P(t) = \langle P \rangle + \delta P(t) \quad (5.7)$$

where  $\langle P \rangle$  is the mean of the signal and  $\delta P(t)$  is the noise part with  $\langle \delta P(t) \rangle = 0$ . The RIN is defined by [116]:

$$\text{RIN}(t) = \frac{\langle \delta P(t)^2 \rangle}{\langle P \rangle^2} \quad (5.8)$$

in the time domain, and in the frequency domain with [116]:

$$\text{RIN}(f) = \frac{\int_{-\infty}^{\infty} \langle \delta P(t)^2 \rangle e^{i2\pi ft} dt}{\langle P \rangle^2}. \quad (5.9)$$

The cumulative RIN is the integration function of the  $\text{RIN}(f)$  [116]:

$$\text{RIN}_{\text{cum}}(f) = \int_{f_0}^f \text{RIN}(F) dF \quad (5.10)$$

In this thesis a backward cumulative RIN is used, so the integration is starting at a frequency  $f_0$  (normally the Nyquist frequency) and integrates then towards zero Hertz.

In Fig. 5.8, final stabilization results are presented. For this, the signal output power at degeneracy is measured with a fast photodiode (Thorlabs FD05D with 1.2V

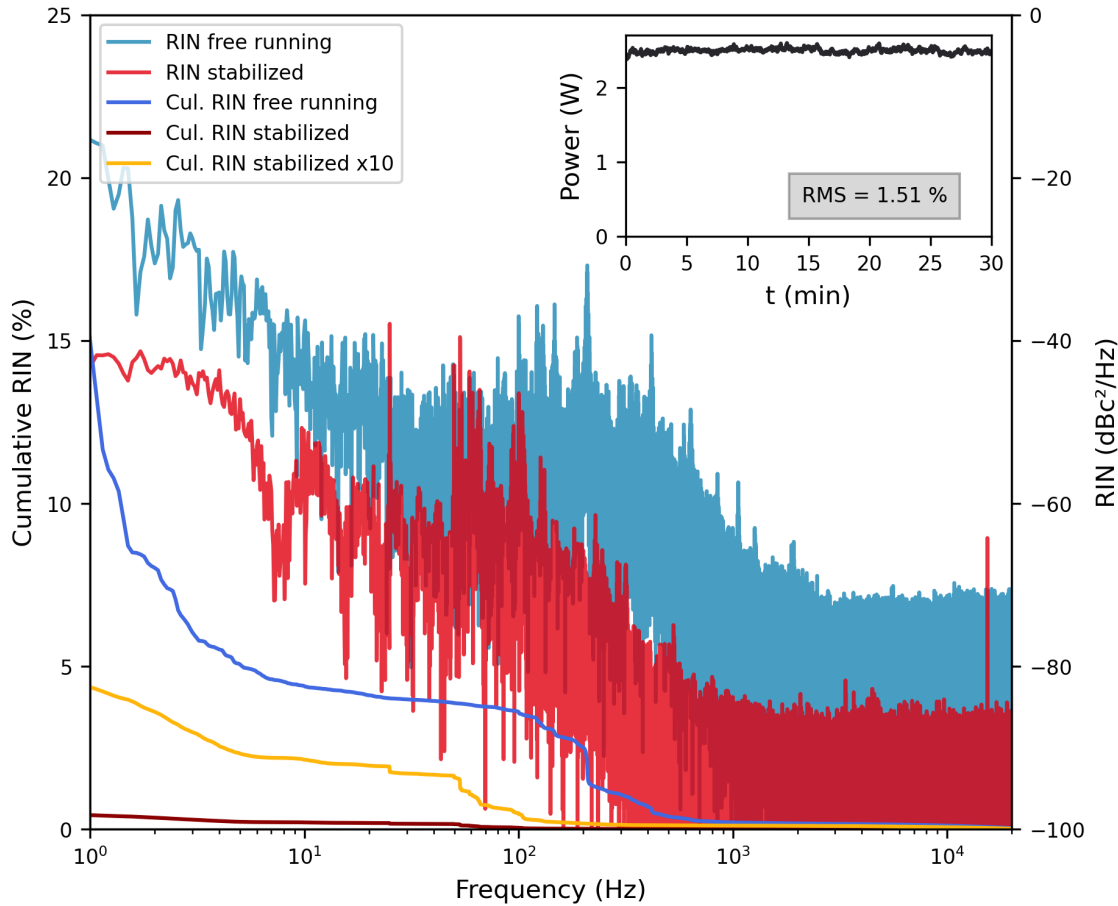


Figure 5.8: RIN of the signal output of the DROPO for the non-stabilized case (blue) and active PI stabilization (red) (see also [108]). A strong reduction of the noise can be recognized. Small peaks remain, which can be possibly corrected by a redesign of the PI controller in the future. The cumulative RIN for the stabilized system is 0.44%, which is comparable with [44]. In the long time measurement, an output power of  $(2.48 \pm 0.04)$  W is achieved.

reverse voltage) for 7 seconds and transformed to RIN. In blue, an example of the non-stabilized system is presented. The DROPO shows strong fluctuation, especially in the frequency range below 10 Hz. With an active PI controller (red), the noise is drastically reduced and is below  $-40$  dBc<sup>2</sup>/Hz. The cumulative RIN is 0.44%, which is comparable to the results in [44]. Peaks around 50, 120, 145, 200 and 350 Hz can be still recognized, which can be possibly attributed by electromagnetic radiation from devices in the laboratory. The 15 Hz and 15 kHz can be explained by possible over-

shooting of the I- and P-part of the controller. However, finding the optimal values of  $K_P$  and  $K_I$  is difficult and requires an experienced experimentalist. Different alignment methods can be tried out, such as the Ziegler-Nichols model [117]. In the future, the PI controller itself can be further improved by using more stable power supplies, electromagnetic shielding and electrical frequency filters in the PI circuit to block resonances of the piezo crystals.

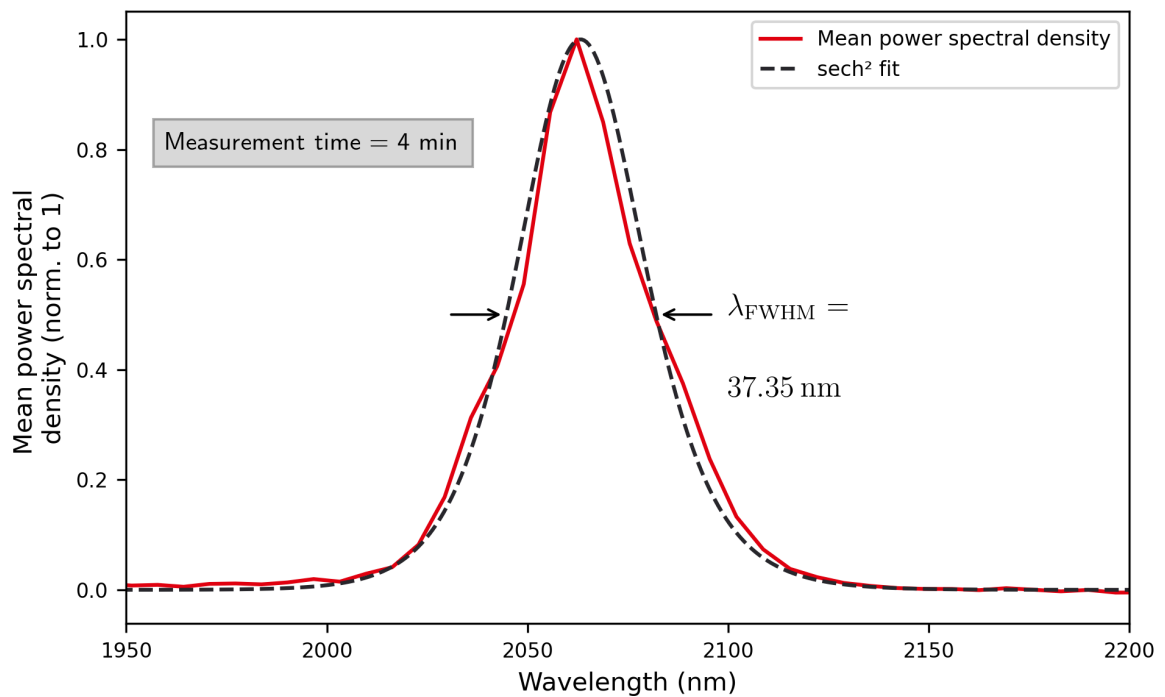


Figure 5.9: Optical spectrum of the DROPO at degeneracy. The spectrum is the mean value of a 4 min long measurement with a spectrometer integration time of 100 ms. The spectral width is around 37 nm. For Fourier-transform limited pulses a pulse duration around 120 fs can be calculated.

The long term stability in terms of the power, measured by a Thorlabs S425C-L Power meter for 30 minutes, is shown in the inset in Fig. 5.8. A stable output of  $(2.48 \pm 0.04)$  W at degeneracy is observed. The required pump power is 9.6 W, which results in a conversion efficiency of 26%. The root-mean-square (RMS) deviation for the long term measurement in Fig. 5.8 is 1.5%. It needs to be noted that the detector has a response time of 0.6 s and frequencies higher than approximately 1.2 Hz are not

taken into account, so that the RMS deviation of 1.51% is only valid for the long time performance.

When the power of the system is stabilized, also the optical spectrum is stable. It is measured with an integration time of 100 ms with a spectrometer (NIRQUEST-256) for four minutes. The mean of the spectra is calculated, which can be seen in Fig. 5.9. The DROPO runs the whole time at degeneracy. From the mean value, a spectral width of 37 nm with a  $\text{sech}^2$  fit can be examined. The Fourier-transform limited pulse duration would be 120 fs in this case, which is shorter than the duration of the pump pulse of 300 fs. Shorter pulses than the pump pulse are also observed in [8]. The presented SF-based stabilization scheme can hold the DROPO effectively on the degenerated resonances, which allows running the DROPO stably in the self-phase locking regime.

## 5.7 Self-phase locking

For generation of a phase stable two-color electrical field, the DROPO phase needs to be phase-locked to the pump. In Chapter 2.4, the self-phase locking was already introduced, which occurs at degeneracy. A well known routine to validate the presence of self-phase locking, is to frequency double the DROPOs output and overlap it spatially and temporally with the pump pulses [118, 8]. On a CCD chip, a stable interference pattern can be measured, when the DROPO is phase-locked. To measure this pattern in our case, the DROPO output is frequency doubled at degeneracy by a 2 mm BBO crystal with a phase-matching angle of  $21.3^\circ$ . A delay line for the pump is built to temporarily overlap the beams. The resulting pattern can be measured with a CCD camera and the temporal dynamics can be observed with a photodiode connected to an RF spectral analyser. In Fig. 5.10, the results are shown for the non-degenerated (a) and degenerated (b) case. In the inset in the upper right, the camera image is illustrated. In the degenerated self-locked case, small interference lines are visible. They vanish when the DROPO is tuned to non-degeneracy. The strong lines in the non-degenerated case are artefacts from a not fully stabilized cavity. In the RF trace for the non-degenerated case, beating notes between the frequency doubled signal/idler and pump can be recognized. In the degenerated case, they are approximately 20 dB suppressed. With this simple measurement, the DROPOs phase coherence can

be quite easily checked for future applications. The self-locking effect is stable in time and no changes could be observed, when the pump power is altered. It can be stabilized on longer timescales ( $> 30$  minutes) with the presented stabilization setup. The effect can be observed in all degenerated resonances. However, it is not clear whether this also applies to the additional resonances, which are presented in Section 3.3. A more comprehensive discussion about the self-locking effect and the role of the additional resonances can be found in [61, 8].

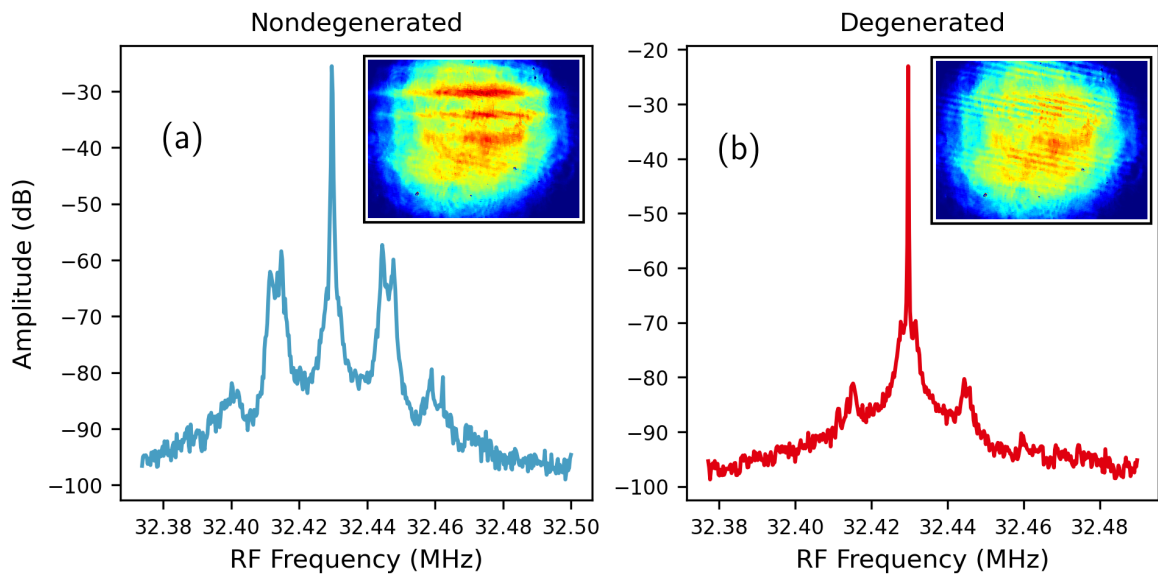


Figure 5.10: Self-phase locking of the DROPO. The second harmonic of the DROPO and pump are overlapped and measured with a photodiode connected to an RF spectrometer and with a CCD chip. (a) In the non-degenerated mode no interference can be measured and beating notes appear. (b) Self-locking mode: a stable interference can be measured and the beating notes are suppressed.

## 5.8 Conclusion

In this chapter, a dither free method for the stabilization of a DROPO was presented. Measurements of the filtered SF signal and its slope to the DROPO signal resonance were shown. The PI controller setup was illustrated and noise characteristics, when the system is actively stabilized, were measured. The stability of the spectrum at degeneracy was presented, and the coherence properties were examined. It was shown that the dither free approach can be used to stabilize the thin-disk laser pumped DROPOs. With the scalability of the DROPO the door is opened for  $> 10\text{ W}$  output power DROPO systems in the  $2\text{ }\mu\text{m}$  regime pumped by a  $1\text{ }\mu\text{m}$  laser. Further improvements on the setup can increase the possible output power and stability.



# Chapter 6

## Summary and outlook

In this thesis, an Yb:YAG thin-disk laser pumped doubly resonant optical parametric oscillator (DROPO) was introduced. Theoretical models and experimental measurements of the DROPO were discussed. The impact of higher-order dispersion terms on the spectral behaviour, when the cavity length is detuned, was measured and compared with a numerical model. Also, a way to achieve high intracavity peak powers in a DROPO was revealed and the dynamic effects in the nonlinear crystal were discussed. At last, a stabilization scheme which uses the sum frequency generation mechanism between pump and signal as an feedback function, was presented. Measurements of the performance of the stabilized DROPO were examined in more detail and the self-locking between pump and signal was verified.

One main goal was achieved, to investigate the influence of higher-order dispersion terms on the DROPOs spectral detuning properties. An oscillator with a BBO crystal as a nonlinear medium in the two micrometer wavelength range was realized. Different materials with positive and negative group velocity dispersion were used to tune the dispersion inside the cavity. Starting from the phase dependent amplification condition of the down-conversion process, analytical equations were derived to describe the impact of the group delay dispersion (GDD) on the detuning resonances of the DROPO. The global emission behaviour was defined by the group delay curve, which depends on the GDD and third-order dispersion (TOD). The expected detuning behaviour was measured and verified with a numerical model, solved by the split-step method. A strong coincidence between theory and experiment could be demonstrated.



The group delay curve depends quadratically on the TOD. It allows to increase the number of degenerated detuning resonances. More available resonances can help to stabilize these systems. Also, explanations for the additional detuning resonances which are located between the main resonances were found. These resonances were caused by spatial effects of the cavity mode, by higher-order transverse modes or non-collinear phase matching. The dependency of the global behaviour of the output spectra on the higher-order dispersion term is systematically described in this thesis and [67] to my knowledge for the first time.

Another achievement was to generate a strong resonant enhancement of the down-converted signal in the cavity. Before, it was not absolutely clear, if high enhancement factor can be archived in a DROPO. An amplitude-based model was presented, which intuitively explains the underlying dynamical effects of conversion and back-conversion. The results of the model were compared with measurements. The scaling behaviour between crystal length, intensity and pump power could be determined and the results were presented in [105]. Furthermore, only a weak impact of higher-order dispersion terms were observed with the split-step based numerical model. High finesses of the cavity also affect the line width of the detuning resonances. The line width was measured for different losses and pump factors and show a good agreement to the predicted assumptions.

The final aim was to stabilize the system. Similar to [44], a stabilization scheme was set up, which is based on a dither-free solution. The required asymmetry between the sum frequency signal and the DROPO's resonance was successfully demonstrated for a thin disk pumped system and measurements of the stabilized system were presented. With this method, the system could be kept stable at degeneracy for more than half an hour. The highest measured output power was 5.1 W with a pump power of 20 W. Due to the Fourier transform limit a theoretical pulse duration of 120 fs could be calculated. The results were comparable with already known systems [8].

## Outlook

A goal for the future of the presented system is the generation of THz radiation with an asymmetric field of the combined DROPO's signal and pump wavelengths. When electrons are ionized by an asymmetric electric field, the so called Brunel harmonics appear [13]. In contrast to the excitation with a single colour electric field, also even

---

harmonics are generated. Especially, the zeroth order of this harmonics is of interest. These frequencies are in the THz regime [119, 14] and have different applications in security [120], spectroscopy [121], but also in fundamental research [122]. In contrast to previous gas based experiments, the THz radiation will be generated in semiconductor materials. It can be expected that, due to the higher electron density, the absolute THz electric field increases by several orders of magnitude in comparison to gas plasmas. To generate free carriers in these materials, the light needs to be absorbed nonlinearly, which depends on the band-gap. Only few materials like gallium phosphide (2.24 eV) are suitable for two photon absorption of the fundamental light (1030 nm  $\rightarrow$  1.2 eV). A new approach of two dimensional nanosheets will be attempted [123, 124]. Depending on the size of these particles, their band-gap alters. For the used two colour field, specific nanosheet parameters can be found for maximum Brunel radiation. The dispersion of the semiconductors must be considered. The overlap between the three colours in the material limits the total efficiency. Using layers of nanoparticles with different band gaps, a quasi phase-matching can be possibly realised to overcome this limitation. With the strong enhanced intracavity fields that were shown in this thesis, the efficiency can be increased even more. In comparison to kHz based CPA systems, the DROPO and the laser run at MHz repetition rate, which has the advantage of better measurement statistics. With this high repetition rate, it can be possible to measure fine structures in the THz spectrum, which give new insights about transitions of high Rydberg states and the continuum [125, 126]. The Brunel radiation can possibly reveal information about ionization delays of electrons in the future [127, 16], too. The future experiments can give rise to new compact, tunable THz sources in the MHz regime.

In [128, 69] a new OPO working regime is presented, where single-cycle pulses in an OPO possibly can be generated by using intracavity Kerr-lens mode-locking. The broadband amplification in the crystal is provided by the magic angle in the non-collinear case. The transfer to the doubly resonant case, where a similar broadband amplification at degeneracy is possible, appears very promising. First simulations at the zero GDD and TOD point, with the split-step based numerical model and a fast saturable absorber, are shown in Fig. 6.1. Pulses of 20 fs duration (blue) for the modulated system could be observed, which are shorter than the non-modulated case (red). To avoid multi-pulses, a proper dispersion management needs to be installed.

DROPOs in this working regime can possibly generate single cycle 2  $\mu\text{m}$  pulses in the future.

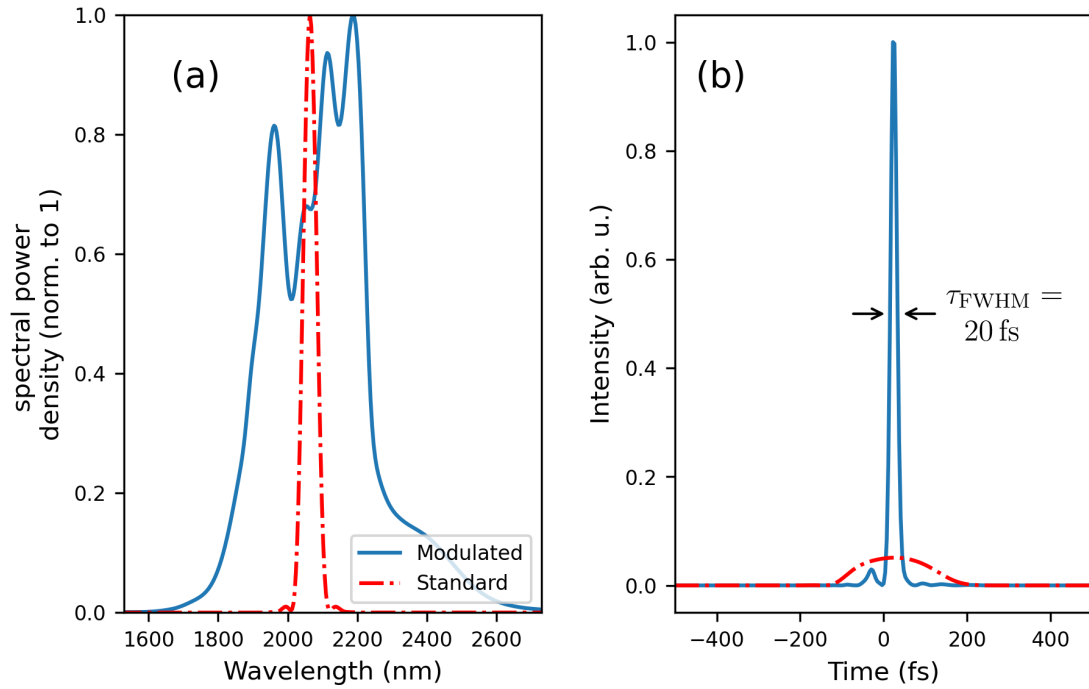


Figure 6.1: Results of the simulation of a DROPO system with a fast saturable absorber (blue) and without one (red). (a) Optical spectrum of the DROPO. The mirrors are highly reflective between 1950 nm – 2150 nm. (b) Temporal shape of both cases.

# Appendices



# Appendix A

## Split-step method based model

In the following, an example of the python code of the used numerical model is shown. This code was developed with several persons. Uwe Morgner, Ihar Babushkin and Ayhan Demircan program the main framework. It was extended at the group workshop 2018 by several persons including Sven Kleinert and is then adapted to the DROPO setup by the author of this thesis. The program is separated in different parts. At first, helper functions are implemented, such as basic variables, Sellmeier equations or reflectivity. In the class "SimuPara" all important parameter for the model can be set. Then the main routine is defined.

```
"""Doubly resonant optical parametric oscillator simulation
    2018-2020
"""

import os
import pickle
import time
import matplotlib.pyplot as plt
import mkl_fft as mkl
import scipy.fftpack as fft
from sellmeiereq import *
from scipy import interpolate
import numpy as np
import scipy.constants as const

# including all packages
```

```

## Defining the refractive indices of the nonlinear crystal
def BBO_no(lam): return sellm("bboo", lam)

def BBO_ne(lam): return sellm("bboe", lam)

def BBO_ni(lam, theta): return 1.0 / np.sqrt(
    np.cos(theta) ** 2 / BBO_no(lam) ** 2 + np.sin(theta) ** 2 /
        BBO_ne(lam) ** 2)

class NonlinearOperator:
    """Class in which the nonlinear interaction and the euler method
        is included"""

    def __init__(self, kappa_o, kappa_e, eeo=False, ooe=True, oeo=False,
                 oee=False, eee=False,
                 ooo=False,
                 solver='euler'):
        self.kappa_o = kappa_o
        self.kappa_e = kappa_e
        self.eeo = eeo
        self.ooe = ooe
        self.oeo = oeo
        self.oee = oee
        self.solver = solver

    def _apply_euler(self, E_o, E_e, dz):
        dE_o = np.zeros(E_o.shape, dtype='int64') + 0j
        dE_e = np.zeros(E_e.shape, dtype='int64') + 0j
        if self.ooe:
            dE_o += E_e * np.conjugate(E_o)
            dE_e += E_o * E_o
        return E_o - 1j * dz * dE_o * self.kappa_o, E_e - 1j * dz *
            dE_e * self.kappa_e

    def apply(self, E_o, E_e, dz, transform=False):

```

```

        return self._apply_euler(E_o, E_e, dz)

def EnergySI(ATa, N, dtAeff): #
    """Energy from an electric field amplitude array in air"""
    return 0.5 * dtAeff * const.c * const.epsilon_0 * np.sum(np.abs(
        ATa) ** 2);

def mirrofct_poly(csvfile='curves/reflexion_new.dat'):
    ''' Function for linear interpolation of a mirror curve (also
        other curves are possible
        :return a function object (good question how you call it :-))
        '''
    mirror_absorption = np.genfromtxt(csvfile, delimiter=',',
        skip_header=0) # reading of
        mirror curve data sample
    a = interpolate.interp1d(mirror_absorption[:, 0],
        mirror_absorption[:, 1]) #
        interpolating data

    return a

class SimuPara:
    """Class of all simulation parameter"""

    def __init__(self):
        self.simname = "2020-07-20 - sim01" # name of measurement
        self.sfolder = "data/" + self.simname
        self.pfolder = "plots/" + self.simname

        self.N = 512 # Number of points in the time/frequency frame
        self.Nz = 80 # Number of steps trough the crystal 80
        self.Nu = 300 # Maximum number of roundtrips
        self.L = 2.0e-3 # xtal thickness
        self.T = 12.0e-12 # time window

        self.plotting = 0 # 0 - no plotting #1 - gif like plotting #
            2 - pcolormesh of signal

```



```
# Crystal parameter
self.deff = 1.8e-12 # BBO chi2 [m/V]
self.Aeff = np.pi * (80.0e-6) ** 2 # Beam area in the
                                     crystal
self.theta = 21.325 # angle for 2 micrometer ooe phase
                                     matching for sip

# OPO Characteristics
self.tau_p = 300.0e-15 # pump pulse duration

self.lambda_p = 1030.0e-9
self.Ppump = 8 # v Aaverage pump power [W]
self.OutputCouplingLoss = 0.02 # Output coupling
                                     transmission
self.OtherLoss = 0.30 # All other roundtrip losses
self.frep = 32.6e6 # OPO rep rate
self.RT_GDD = 0e-30 # dispersion outside the bbo xtal #-
                                     3785e-30 #

self.GDD_crystal = 250E-30
self.RT_TOD = 26700e-45
# self.RT_TOD = 400000E-45

# GD Managment
self.gd1 = -200e-15 # GD range
self.gd2 = 100e-15
self.dgd = 0.4e-15 # gd step
self.gda = np.arange(self.gd1, self.gd2, self.dgd)
self.Ng = len(self.gda) # steps of gd change

# Mirrorparameter
self.N_mirror = 12
self.mirrorstart = 1.95E-6
self.mirrorend = 2.2E-6
self.mirrorloss = 1 - (1 - 0.0006) ** 12
# print(mirrorloss)
self.mirrorstiffness = 5
self.calc_time = 0
```

```
class TemporaryData:
    """Temporary variables of the simulation"""

    def __init__(self):
        self.A0 = np.nan # electric pump field
        self.IO = np.nan # pump intensity
        self.t0 = np.nan
        self.kappa_p = np.nan
        self.kappa_si = np.nan
        self.w0 = np.nan

        self.Ap0a = np.nan # pump field envelope, tau_p: FWHM
        self.Apa = np.nan
        self.Apa_ = np.nan
        self.Asia_ = np.nan # loss, phase, GD, GDD of the whole
                             roundtrip

        self.df = np.nan # frequency incremental
        self.dt = np.nan # time incremental
        self.dz = np.nan # space incremental
        self.ia = np.nan

        self.eiRTa = np.nan
        self.eikpa = np.nan
        self.eiksia = np.nan

        self.phase_a = np.nan
        self.gd = np.nan

        self.asia_array_plot = np.nan
        self.apa_array_plot = np.nan

        self.asia_spec_array_plot = np.nan

class CalculatedData:
    """Calculated Data by the simulation"""

    def __init__(self):
        self.fpa = np.nan # Pump frequency vector
```

```
self.fsia = np.nan # Signal frequency vector
self.kpa = np.nan # Pump wave number vector
self.ksia = np.nan # Signal wave number vector
self.wsia = np.nan # Signal angular frequency vector

self.lam_pa = np.nan # array for used/calculated pump
                    # wavelenghts
self.lam_sia = np.nan # array for used/calculated signal
                    # wavelenghts

self.SpecOut = np.nan ## big outout array for contour plot
self.SpecOutp = np.nan ## big outout array for contour plot

self.P = np.nan # Power array

self.mirror_loss = np.nan
self.mirror_curve = np.nan

def main():
    # Initializing classes and generation of the necessary folders
    parameter = SimuPara()
    data = CalculatedData()
    temp = TemporaryData()

    if not os.path.exists(parameter.sfolder):
        os.makedirs(parameter.sfolder)
    if not os.path.exists(parameter.pfolder):
        os.makedirs(parameter.pfolder)

    # Defining of various variables and arrays
    data.SpecOut = np.zeros(shape=(parameter.Ng, parameter.N)) ##
                        # big outout array for contour
                        # plot
    data.SpecOutp = np.zeros(shape=(parameter.Ng, parameter.N)) ##
                    # big outout array for contour
                    # plot

    # define time/frequency windows
    temp.dt = parameter.T / float(parameter.N)
```

```

temp.df = 1.0 / parameter.T
temp.dz = parameter.L / float(parameter.Nz)
temp.ia = np.arange(parameter.N) - parameter.N / 2
temp.ta = (np.arange(parameter.N) - 3 * parameter.N / 4) * temp.
           dt # time axis with off
           center zero

# to be used later
temp.fpa = temp.ia * temp.df + const.c / parameter.lambda_p #
           pump wavelength in the center
           of the frequency window

data.lam_pa = const.c / temp.fpa
data.kpa = 2.0 * np.pi / data.lam_pa * BBO_ni(data.lam_pa,
        parameter.theta * np.pi / 180.
        0) # ooe type I for sip

data.fsia = temp.ia * temp.df + const.c / (
        2.0 * parameter.lambda_p) # pump wavelength in the
        center of the
        frequency window

data.lam_sia = const.c / data.fsia
data.wsia = 2.0 * np.pi * data.fsia # omega
temp.w0 = data.wsia[int(parameter.N / 2)] # central omega
data.ksia = 2.0 * np.pi / data.lam_sia * BBO_no(data.lam_sia) #
        ooe type I for sip

temp.eikpa = np.exp(1.j * data.kpa * temp.dz)
temp.eiksia = np.exp(1.j * data.ksia * temp.dz)
temp.eikpa = fft.fftshift(temp.eikpa)
temp.eiksia = fft.fftshift(temp.eiksia)
temp.kappa_p = np.pi / parameter.lambda_p * parameter.deff /
        BBO_ni(parameter.lambda_p,
        parameter.theta * np.pi / 180)
temp.kappa_si = np.pi / parameter.lambda_p * parameter.deff /
        BBO_no(2 * parameter.lambda_p)

# Initializing of nonlinear operator
NLop = NonlinearOperator(temp.kappa_si, temp.kappa_p)

# Mirror losses
data.mirror_curve = mirrofct_poly() # generating mirror fct out
        of sample curve

```

```

mirroloss_lambda_0 = data.mirror_curve(data.lam_sia) #
                                     generating datavec for
                                     calculations
mirroloss_lambda = 1 - mirroloss_lambda_0 ** parameter.N_mirror
                                     # with amount of mirrors

# Simulation
g = 0
temp.t0 = time.time()
losses = parameter.OutputCouplingLoss + parameter.OtherLoss +
        mirroloss_lambda

for temp.gd in parameter.gda: # gd loop
    temp.asia_array_plot = np.zeros([parameter.Nu, parameter.N])
    temp.apa_array_plot = np.zeros([parameter.Nu, parameter.N])
    temp.asia_spec_array_plot = np.zeros([parameter.Nu, parameter
        .N])

    temp.phase_a = (temp.gd - 5.5875315724323488e-9 * parameter.L
        ) * data.wsia + 0.5 * (
        parameter.RT_GDD +
        parameter.GDD_crystal) * (
        data.wsia - temp.w0) ** 2
        + 0.166 * parameter.RT_TOD
        * (data.wsia - temp.w0)
        ** 3;

    temp.eiRTa = np.exp(
        1.j * temp.phase_a - 0.5 * losses - 0.5 * (parameter.
            OutputCouplingLoss +
            parameter.OtherLoss))
        # +mirroloss_lambda

    temp.eiRTa = fft.fftshift(temp.eiRTa)

    data.P = np.zeros(parameter.Nu)

    temp.I0 = parameter.Ppump / parameter.frep / parameter.tau_p
        / parameter.Aeff # pump
        intensity

```

```

temp.A0 = np.sqrt(2.0 * temp.I0 / const.epsilon_0 / const.c /
                 1.6) # electric pump
                        field
temp.Ap0a = 0j + temp.A0 / np.cosh(temp.ta / parameter.tau_p
                                   * 1.762747173) # pump
                                                field envelope, tau_p:
                                                FWHM

temp.Asia = temp.Ap0a * 0.2
temp.Asia_ = fft.fft(temp.Asia)
temp.ft_AP0a = fft.fft(temp.Ap0a)

##### OPO roundtrips
for r in np.arange(parameter.Nu):
    temp.Apa_ = temp.ft_AP0a # fresh pump pulse
    ##### propagation through the crystal
    for z in np.arange(parameter.Nz):
        temp.Asia = mkl.ifft(temp.Asia_)
        temp.Apa = mkl.ifft(temp.Apa_)
        temp.Asia, temp.Apa = Nlop.apply(temp.Asia, temp.Apa,
                                         temp.dz)

        temp.Asia_ = mkl.fft(temp.Asia)
        temp.Apa_ = mkl.fft(temp.Apa)
        temp.Asia_ *= temp.eiksia
        temp.Apa_ *= temp.eikpa # linear propagation in
                                spectral domain

    ##### roundtrip outside the crystal
    temp.Asia_ *= temp.eiRTa # phase, GD, GDD of the whole
                                roundtrip

    temp.Asia = mkl.ifft(temp.Asia_)

data.P[r] = EnergySI(temp.Asia, parameter.N, temp.dt *
                    parameter.Aeff) *
                    parameter.frep *
                    parameter.
                    OutputCouplingLoss #
                    average output power

if (r == 100 or r == 200) and data.P[r] < 0.01: break #
                    quick break of the
                    roundtrip loop when no

```

```

                                                    power

temp.asia_array_plot[r, :] = np.abs(temp.Asia)

spec_temp = fft.fftshift(temp.Asia_)
temp.asia_spec_array_plot[r, :] = abs(
    spec_temp) ** 2 * temp.dt * parameter.Aeff * 0.5 *
                                                    const.c * const.
                                                    epsilon_0 /
                                                    parameter.frep *
                                                    parameter.
                                                    OutputCouplingLoss

if parameter.plotting == 1: # Starting Plot Show
    if np.mod(r, 5) == 0:
        # print(r)
        fig1 = plt.figure(20)
        fig1.clear()
        plt.subplot(2, 1, 1)
        plt.plot(temp.ta * 1E12, np.abs(temp.Asia))
        plt.plot(temp.ta * 1E12, np.abs(temp.Apa))
        plt.xlabel('time (ps)')
        plt.ylabel('power (W)')

        plt.subplot(2, 1, 2)
        plt.plot(data.lam_sia * 1E6, abs(fft.fftshift(
            temp.Asia_)) ** 2 * temp.dt * parameter.Aeff
            * 0.5 *
            const.c *
            const.
            epsilon_0
            /
            parameter.
            frep)
        # plt.plot(data.lam_sia * 1E6, np.abs(temp.Apa))
        plt.xlabel('wavelength (micrometer)')
        plt.ylabel('spectral power density (W/lambda)')

    plt.ion()
    plt.pause(0.2)

```

```

plt.show()

if parameter.plotting == 2: # Starting Plot Show

    # print(r)
    fig1 = plt.figure(20)
    fig1.clear()

    plt.subplot(2, 1, 1)
    plt.pcolormesh(data.lam_sia * 1.0e9, np.arange(parameter.
                                                    Nu), temp.
                  asia_array_plot, cmap=
                  "hot")

    # plt.plot(temp.ta * 1E12, np.abs(temp.Asia))
    # plt.plot(temp.ta * 1E12, np.abs(temp.Apa))
    plt.xlabel('time (ps)')
    plt.ylabel('Roundtrip (N)')

    plt.subplot(2, 1, 2)
    plt.pcolormesh(data.lam_sia * 1.0e9, np.arange(parameter.
                                                    Nu), temp.
                  asia_spec_array_plot,
                  cmap="hot")

    # plt.plot(data.lam_sia * 1E6, np.abs(temp.Apa))
    plt.ylabel("Roundtrip (N)")
    plt.xlabel('spectral power density (W/lambda)')
    plt.savefig(parameter.pfolder + "/" + parameter.simname +
                "_" + str(g), dpi=300
                )

    # plt.ion()
    # plt.pause(0.5)
    # plt.show()

temp.Asia_ = fft.fftshift(temp.Asia_)
data.SpecOut[g] = abs(
    temp.Asia_) ** 2 * temp.dt * parameter.Aeff * 0.5 * const
    .c * const.epsilon_0 /
    parameter.frep *
    parameter.
    OutputCouplingLoss

```



```

temp.Apa_ = fft.fftshift(temp.Apa_)
data.SpecOutp[g] = abs(
    temp.Apa_) ** 2 * temp.dt * parameter.Aeff * 0.5 * const.
        c * const.epsilon_0 /
        parameter.frep #
        output spectrum
print(parameter.Ng - g, 'gd=', temp.gd * 1.0e15, 'fs', '-->P=
        ', data.P[r - 1])

g += 1

parameter.calc_time = time.time() - temp.t0
print("Calculation time: ", parameter.calc_time / 60, " min")

## Plotting
plt.figure(1)
plt.title('GDD = ' + str(parameter.RT_GDD * 1e30) + " fs^2 | " +
        "TOD = " + str(
        parameter.RT_TOD * 1e45 + 1027 * parameter.L * 1E3) + " fs^3"
        )
plt.pcolormesh(data.lam_sia * 1.0e9, parameter.gda * 1.0e15, data
        .SpecOut, cmap=plt.cm.jet)

# plt.grid('on')
plt.colorbar()
plt.xlabel('wavelength (nm)')
plt.ylabel('net gd (fs)')
plt.savefig(parameter.pfolder + "/spectrum_vs_length.png", dpi=
        150)

plt.xlim(1830, 2330)
plt.show()

# Saving data
savedat = open(parameter.sfolder + "/parameter.pkl", "bw")
pickle.dump(parameter, savedat)
savedat.close()

savedat = open(parameter.sfolder + "/data.pkl", "bw")
pickle.dump(data, savedat)
savedat.close()

```

```

if __name__ == "__main__":
    main()

```

## Additional simulations of the spectral detuning

In this section additional simulation of the numerical model are shown, which cannot be verified by the used experimental system in this thesis, but can be explained with the principles presented in Chapter 3.

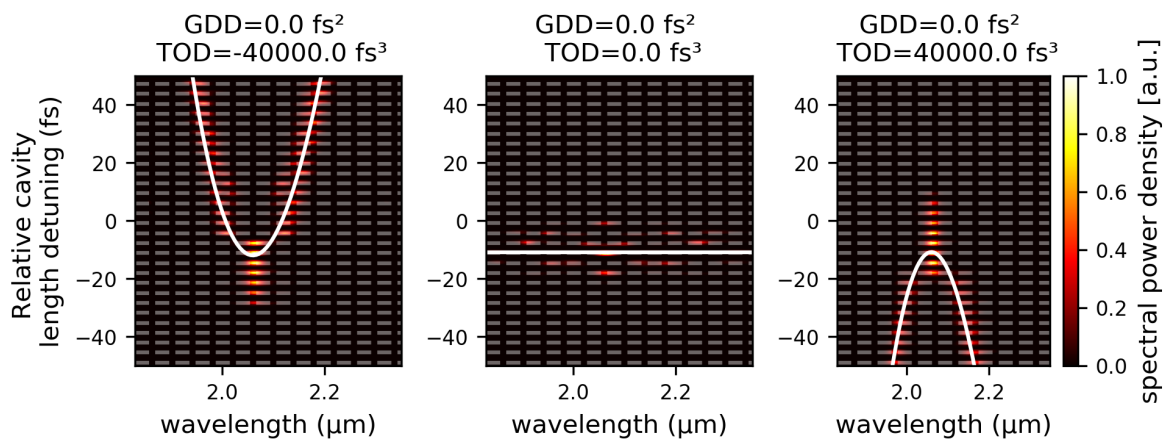


Figure A.1: Spectral behaviour if the cavity length is detuned. The GDD is set to zero. The TOD is is tuned from the negative to positive region.

## Sum frequency asymmetry for different group delay dispersion

In Chapter 5 the stabilization with the sum frequency signal of pump and signal is described. In the following, simulations, based on the split-step method, of the signal in dependence of different parameters are presented.

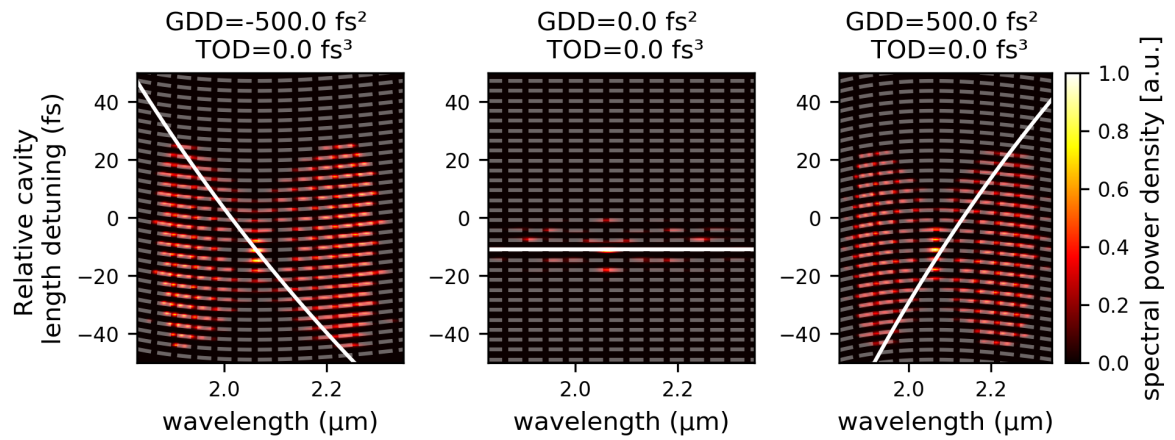


Figure A.2: Spectral behaviour if the cavity length is detuned. The TOD is set to zero. The GDD is is tuned from the negative to positive region.

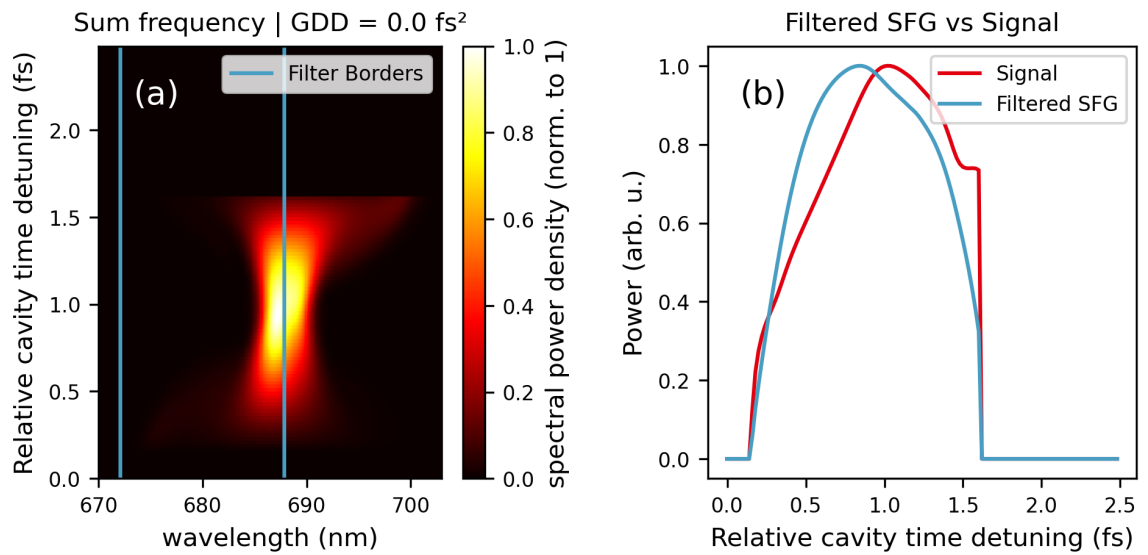


Figure A.3: Simulation of the filtered SF signal for 4 mm BBO crystal and at the zero GDD point. The asymmetric shape of the spectral response when the cavity length is detuned is clearly visible.

In the following, the filtered SFG for different GDD regimes is shown. The spectral filtering is not altered, so that the simulations can be compared.

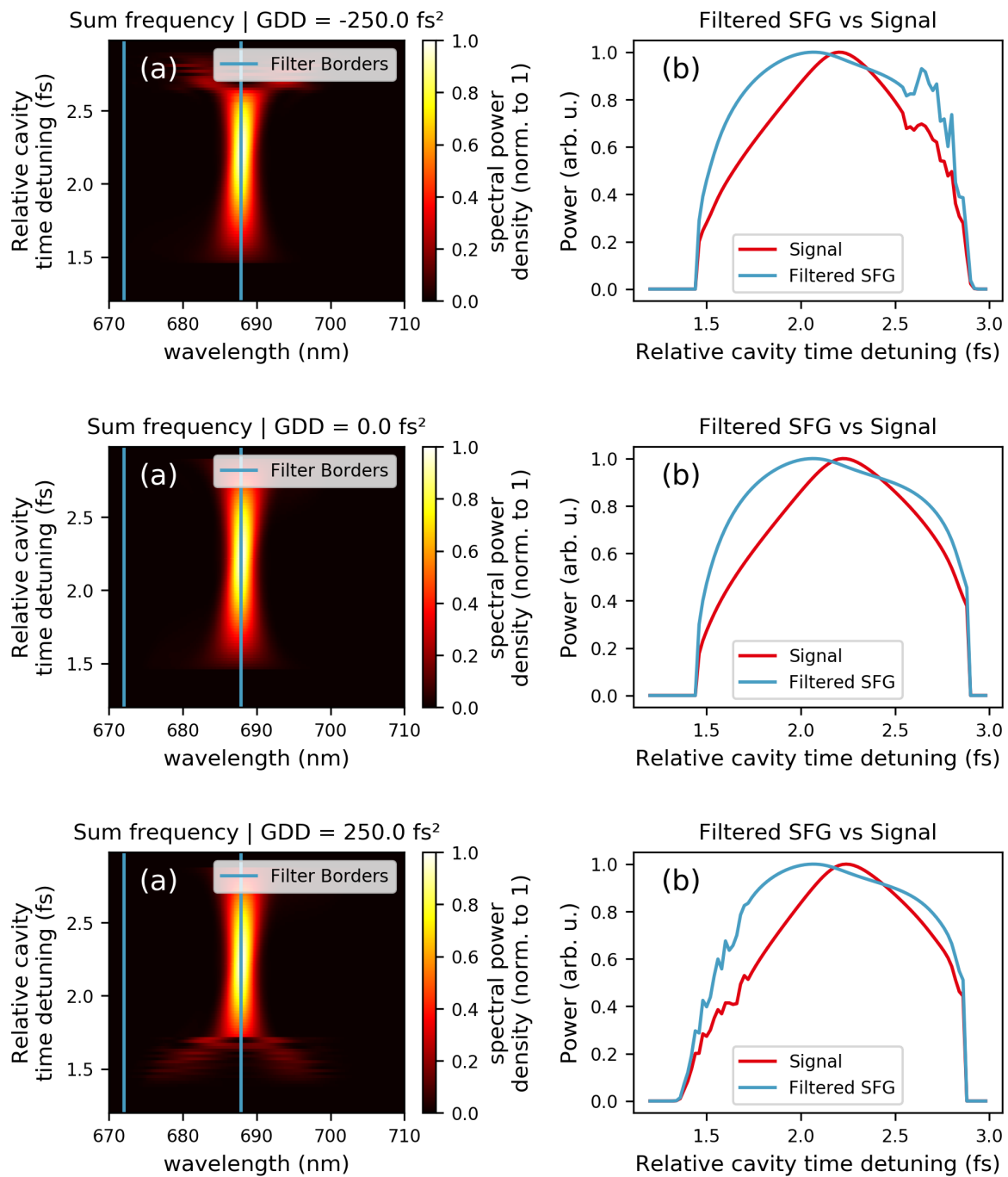


Figure A.4: Simulation of the filtered SF signal for negative, zero and positive GDD (2 mm BBO crystal).



# Appendix B

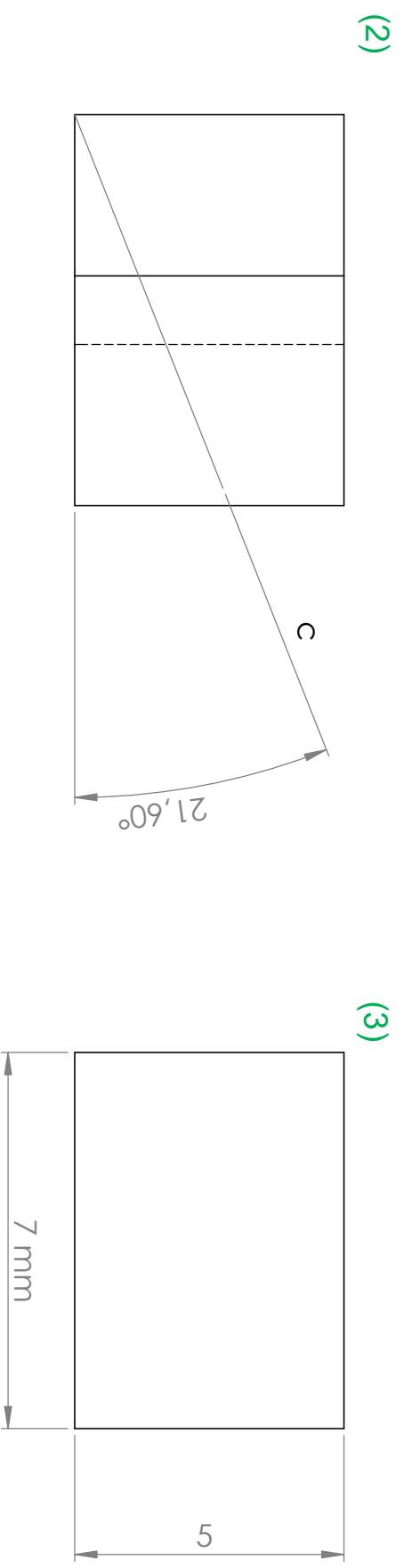
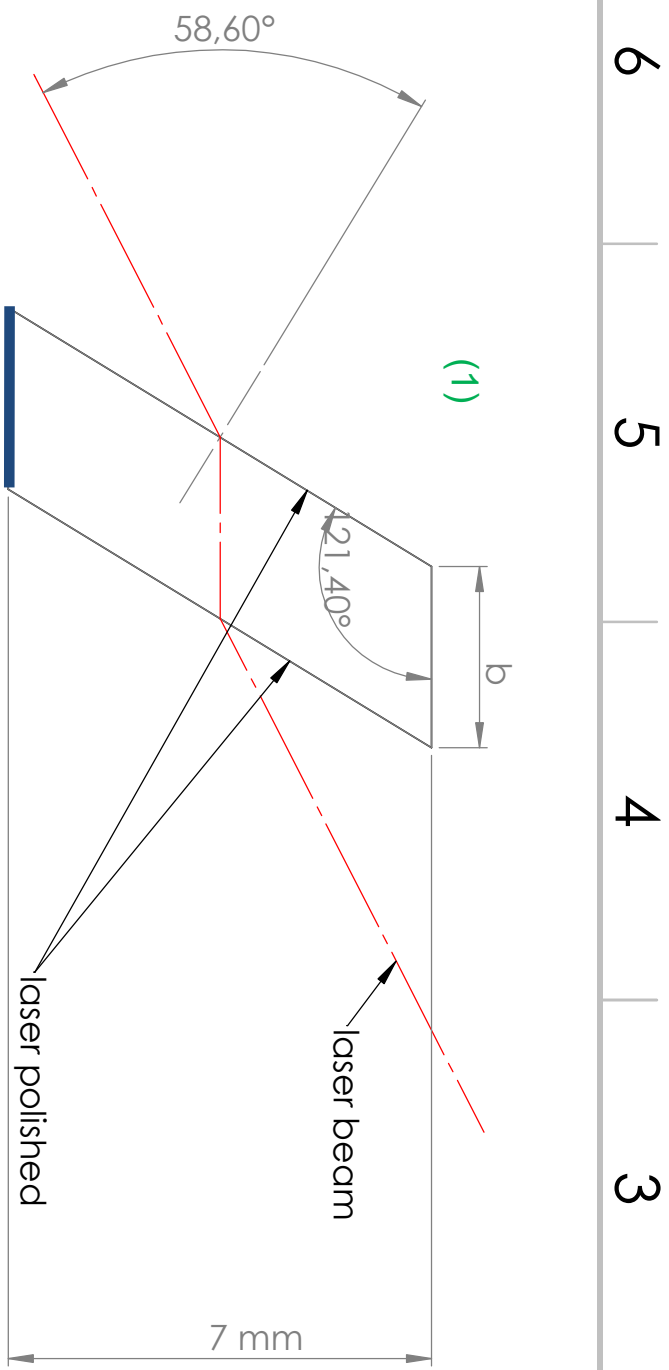
## Design of optical and electric elements

### BBO crystal

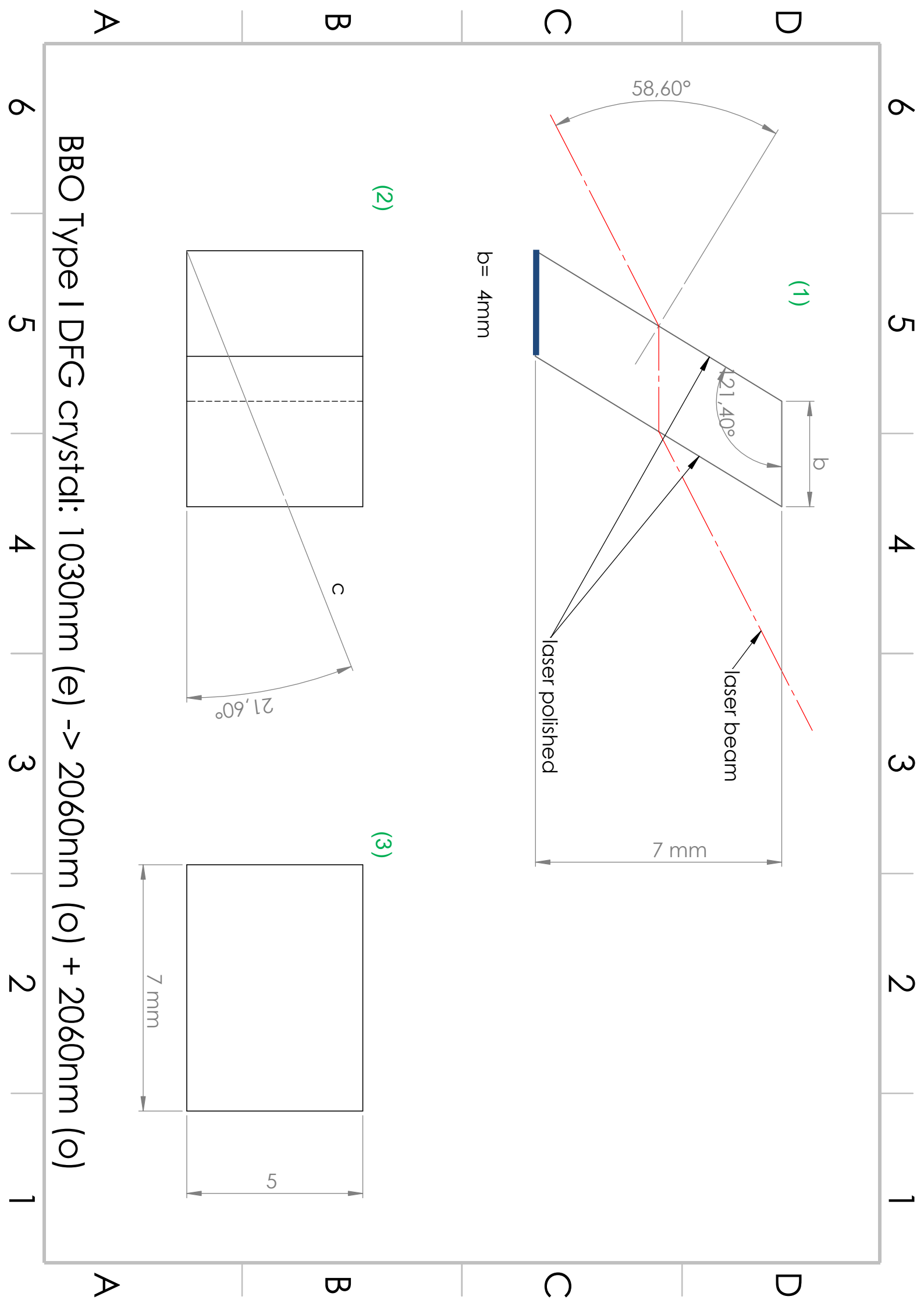
For the DROPO, type I BBO crystals in the collinear geometry were used. In the following the correct cutting of this uniaxial crystal is explained more in detail and also design consideration for proper manufacturing are shown. The two important parameters are the phase-matching which can be calculated by 2.7 and the brewster angle. The phase-matching of the crystal was here chosen to  $21.6^\circ$ , but can be tuned over the whole phase-matching regime in Fig. 3.3 by mounting the crystal on a goniometer and add an additional tilt. The brewster angle  $\arctan(n) = 58.60^\circ$  is relatively wavelength insensitive and here chosen for the degenerated waves in the cavity. On the next page the typical drawing which was send to the manufactures is shown. Important in this design is that the red o-beam propagate parallel to the cutting edge (thick blue line) in the base area of the nonlinear crystal (1). In the plane which spanned by this line and side view (2) the crystal axis is defined. From experience the manufactures need this parallelism between the cutting edge of the crystal and the crystal axis for proper alignment of the cuts and manufacturing. In (3) the front view of the crystal is shown. Here the height is defined. In (1) is the effective length for the Brewster-cut crystal.

## **Solidworks design on the cavity**

The design of the crystal cavity are shown on the next two pages. The mirrors distances and angles can be used to rebuild this system. All not named mirrors are plane.

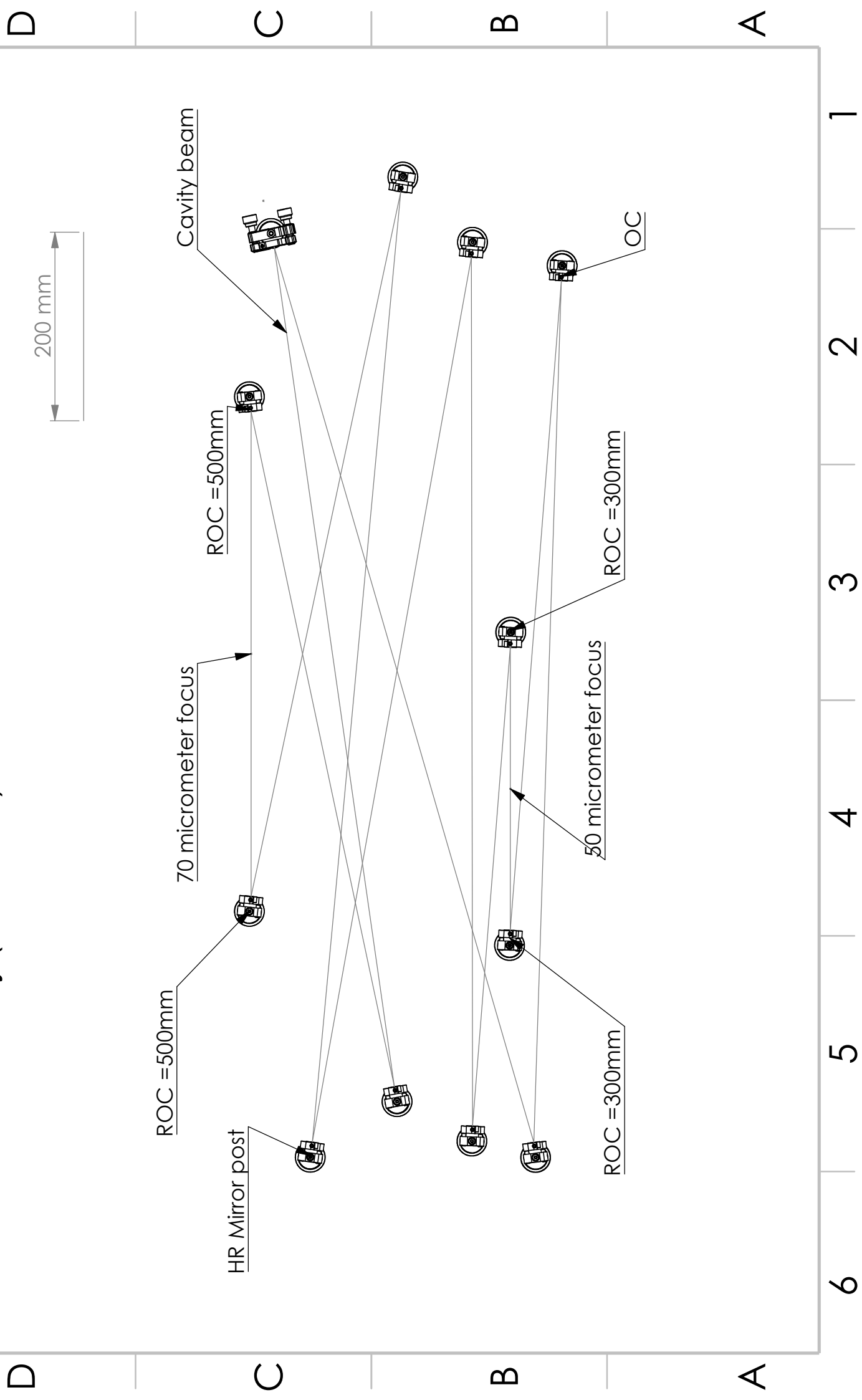


BBO Type I DFG crystal: 1030nm (e) -> 2060nm (o) + 2060nm (o)





# Bow-tie DROPO cavity (Scale: 1:5)



## Circuit diagram of the PI controller

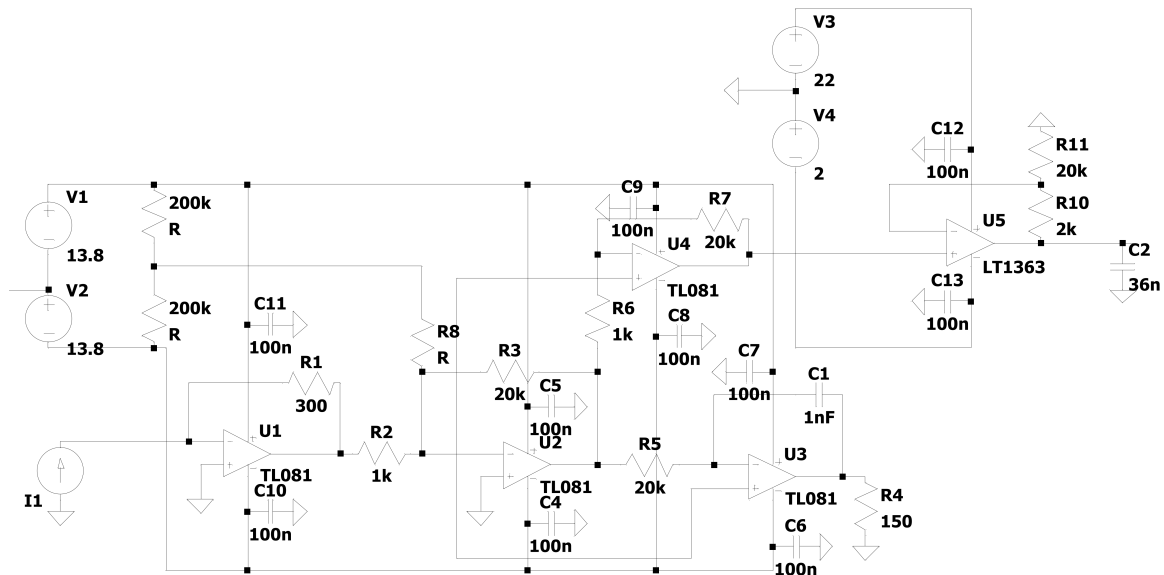


Figure B.1: LT SPICE circuit diagram of the PI controller

The PI controller was built on a small printed circuit board. Basically it is a cascade of operational amplifier (OPamp). In the circuit diagram Fig. B.1 TL081 OPamp models are illustrated. Actually in the final circuit U1, U2 and U3 are upgraded to OPA134 which have lesser voltage noise. For the P-part the current from the photodiode I1 is amplified by negative feedback Opamp circuits U1, U2, U4. For the last OPamp U5 a LT1363 model is used because it can handle better the capacity of the piezo crystal. The OPamp is installed as a noninverting one to keep the same sign as the I-part. For the integration part the output voltage of U2 is split up and U3 is used as an integrator. The output of this OPamp is then fed in the modulation input of the piezosystemsjena piezo driver. The OPamps U1-U4 are supplied by a symmetric  $\pm 13.8\text{V}$  voltage. U5 is in comparison supplied with  $-2$  and  $22\text{V}$ , because the piezo can only work in the positive range. For proper operation two power supplies are necessary. One is provide the symmetric voltage and ground. The other give a voltage between  $0$  and  $24\text{V}$ . All OPamps share the same ground. The set point is induced in the system by an potentiometer (R8) from the symmetric supply voltage to U2. An additional offset is added to U4 (not shown in the figure) for keeping the voltage in the positive regime.



# Appendix C

## Additional alignment routines and measurements

### Alignment routines

During the operation of the DROPO, additional alignment is often necessary. A CCD camera can be placed behind the output coupler. Two photon absorption on the silicon chip can help to observe possible higher transversal modes, which can be corrected. For further analysis, the spectrum can be measured, when the cavity length is detuned. However, in some cases the system is running in the single resonant state (Fig. C.5 (a)). In this case the oscillator shows continuous tuning abilities and moderate output power. In general, a full readjustment is necessary. For a well aligned system, the detuning behaviour in the spectral domain for the zero GDD case is shown in Fig. C.5 (b).

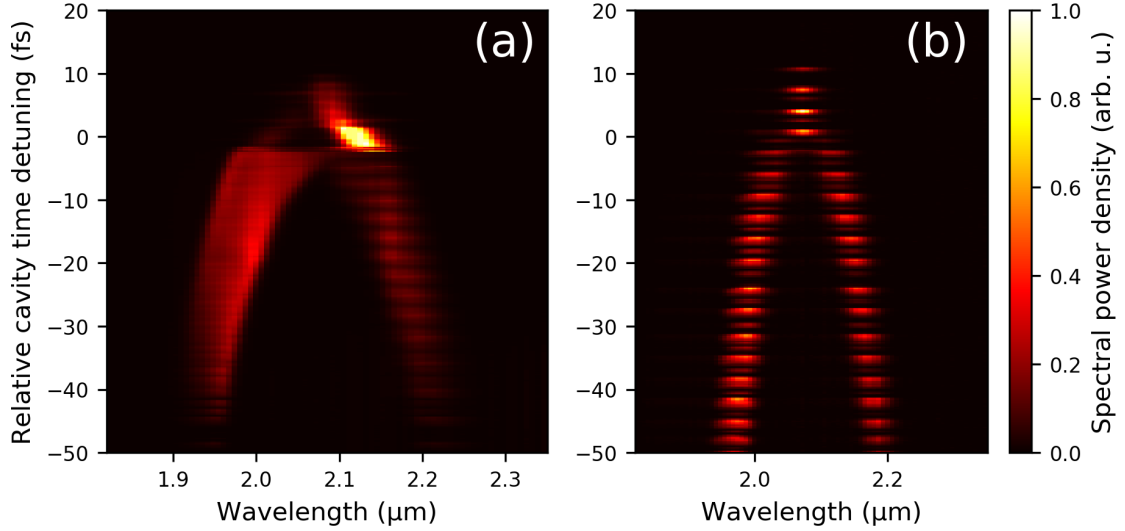


Figure C.1: Spectral behavior when the cavity length of the OPO is detuned, depending on the alignment. (a) Singly resonant mode. Due to clipping on mirrors or other misalignments, only signal or idler is fully resonant in the cavity. The output power and performance of this system is relatively stable, but this state should be avoided due to bad spectral and spatial performance. (b) Example of a well aligned system. The detuning resonances of the doubly resonant operation are well recognizable. Also, the distinct degeneracy regime is accessible.

## C.1 Alignment procedures

Routines need to be found to align the DROPO system to its optimum. The difficulty lies in the fact that for DFG emission nearly all components, especially the cavity length and mirrors, need to be aligned with high precision. In the following the alignment procedures for the DROPO are presented.

### Nonlinear crystal

Due to the long Rayleigh lengths around 7 mm of the signal/idler mode in the cavity, the crystal can be positioned in the middle of the focussing mirrors with the precision provided by a measuring tape. Then, the Brewster's angle of the crystal is found by minimizing the pump beam reflection in p polarization.

The phase-matching in the crystal is sensitive to minutes of arc of the crystal axis. For

alignment the optical parametric fluorescence is tracked. For the detection, the electrical signal of an photodiode (extended InGaAs) is amplified by an ADA4530-1 amplifier from Analog Devices. This detector can measure power levels in the femtowatt range and is suitable to detect the parametric fluorescence. A germanium filter is installed to prevent the detection of pump light. When the crystal is pumped, the fluorescence can be focused on the detector and the signal can be measured with a combination of a lock-in amplifier and an optical chopper. The crystal angle is then tuned for maximum fluorescence.

## Cavity mirrors

The cavity was planned with a 3D-CAD software (SolidWorks) and the mirrors are positioned on the breadboard by hand with an accuracy of  $\pm 3$  mm. As the stability of the cavity is also in this range, no more precise alignment of the curved mirrors is necessary. Since the mirrors are reflective at 700 nm, a beam from another OPO with the same repetition rate is coupled into the cavity to adjust the mirrors. In the DROPO cavity, a provisory fused silica plate is set to reflect a small fraction of the incoupled beam on a CCD chip. The first and second passage of the alignment beam in the cavity can be monitored. If the length is matched to the correct repetition rate, interference lines appear on the chip. While the nonlinear crystal is pumped, a small fraction of the fundamental beam is transformed to the second harmonic (SHG) at 515 nm. It can be used to superimpose the pump with the cavity mode. By altering the cavity length around hundreds of micrometer and angle tuning one mirror, the accurate configuration can be found, and down-converted light is observable.

A faster alignment procedure can be used if the correct cavity length is adjusted. The cavity is aligned directly by the parasitic SHG signal of the pump. With the two end mirrors, the green light is overlapped in the second round-trip with itself. The advantage of this method is the simultaneous alignment of the cavity mirrors and the pump beam. The DROPO begins to generate light, when all mirrors are carefully aligned and the length is correctly adapted.

## C.2 Passive Stabilization

Different noise sources contribute to the instabilities of the DROPO performance. It is advantageous to recognise these first and eliminate them if necessary. For this purpose, the DROPO is operated in the negative dispersion regime (3 mm BBO, 30% OC,  $-2070 \text{ fs}^2$ ,  $11700 \text{ fs}^3$ ). Here, the resonances are bended (see Fig. 3.7), so that the system can run free on one resonance on a longer timescale. The SF signal is measured with an amplified photodiode and an oscilloscope. The time series and its Fourier transform is displayed in in Fig. C.2. It can be recognized that the main noise source

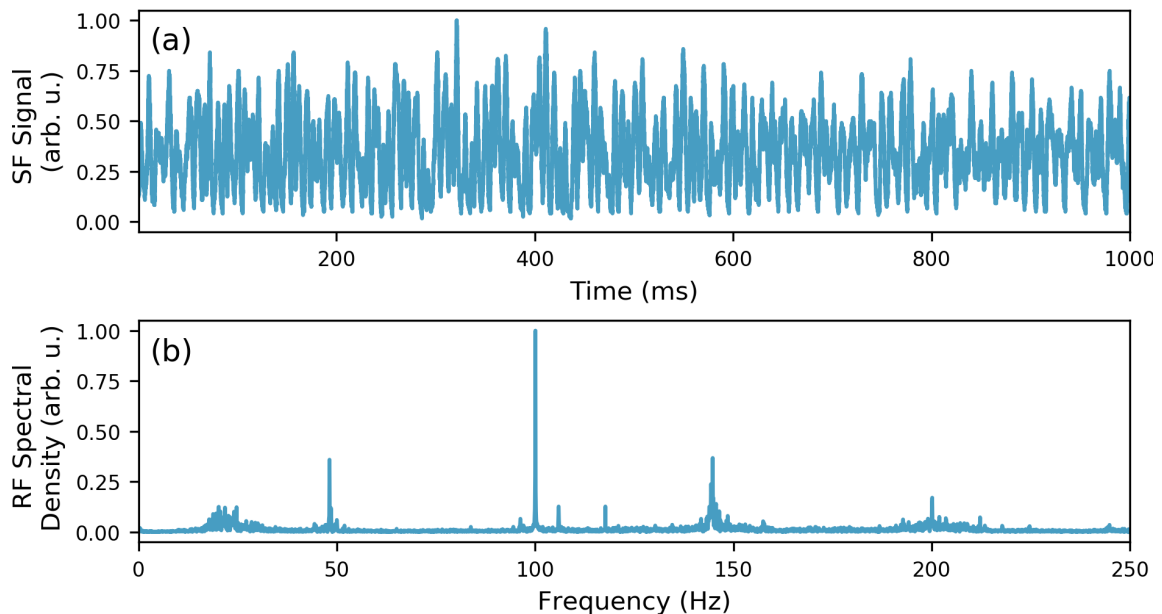


Figure C.2: Measurement of the SF signal of the free running DROPO. (a) The SF signal is measured with a photodiode and an oscilloscope for 10 seconds. (b) The Fourier transform of (a) is calculated. Peaks around the mains frequency (50 Hz) and its higher harmonics can be recognized.

of the system are frequency peaks around 50 Hz and higher harmonics of this frequency, which is the power grid frequency in Germany. Finding the source of this noise can be difficult, because near the optical table there are several electrical devices, which can be sources of disturbance. The frequencies can influence the DROPO mechanically, like in Fig. C.2, and due to electrical disturbances the stabilization feedback loop.

## Electrical isolation and precautions

To reduce noise in the system, various measures have been taken. Insignificant electrical devices were turned off and disconnected from the power grid. Care is taken to ensure that all the equipment is connected to only one wall plug to avoid ground loops or other electrical disturbances. Also, the mirror mounts, with the piezo actuators, and the PI controller are isolated from the optical table with ceramic and plastic posts.

## Reduction of acoustic noise sources

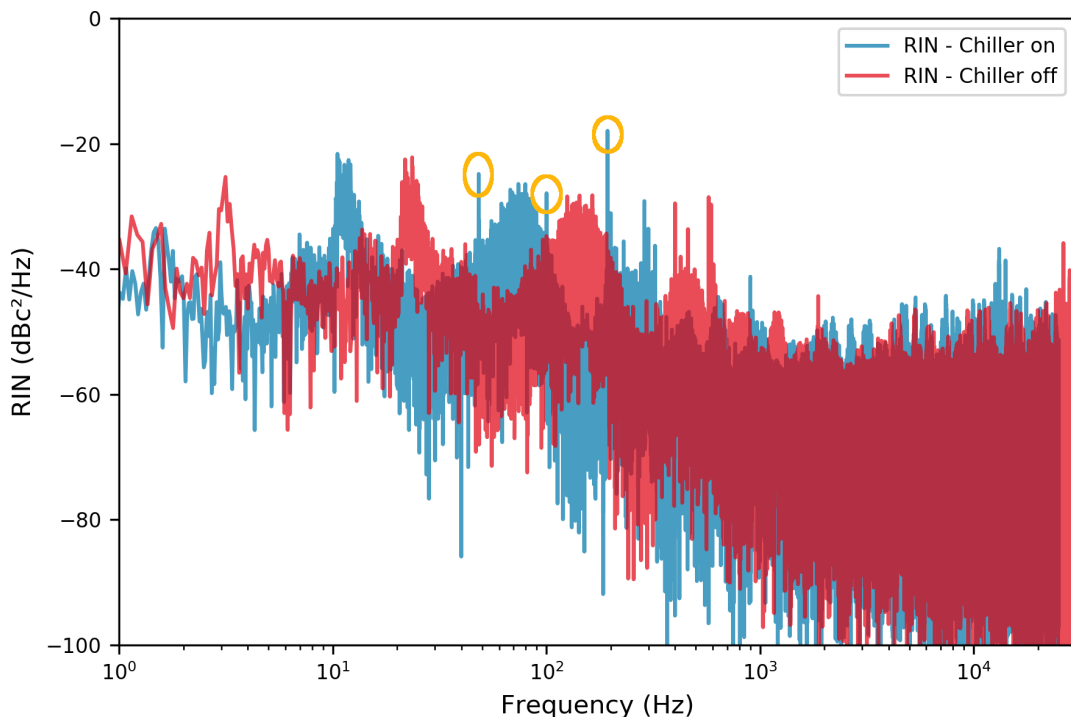


Figure C.3: Acoustic noise on the optical table with activated and turned off water chillers for the laser cooling. It can be seen that in the range of 50 until 300 Hz strong peaks appear (yellow circles) in the case where the chillers turned on. A solution is to relocate the chillers to suppress their influence. The broadband noise peaks at 3 Hz, 10 Hz and 200 Hz and their shift to higher frequencies are not necessary correlated to the chillers and are caused by unknown influences or effects.



Besides the electrical insulation, acoustic measurements are done on the optical table. For this, a piezo pickup plate for acoustic instruments is mounted between two glass substrates as dielectrics, which are compressed by a weight. The plate is positioned in the middle of the breadboard of the DROPO, to examine possible acoustic influences. The resulting electric voltage is then measured by an oscilloscope. Typically mean voltages of 1.5 mV were observed. It appears that strong 50 Hz noise and higher harmonics are generated by the water chillers, which is shown in the RIN measurements in Fig. C.3 (yellow circles). A measurement is taken with turned on (blue) and turned off (red) chillers. It can be seen that the mains frequency peaks vanish without running chillers. It needs to be noted that the intensity of the power grid frequencies can be much higher (or lower) on different positions of the table, which was not quantitatively examined. However, to reduce the noise, the chillers were positioned in a side room. In Fig. C.4 the measurement in Fig. C.3 is repeated. Here, the chiller

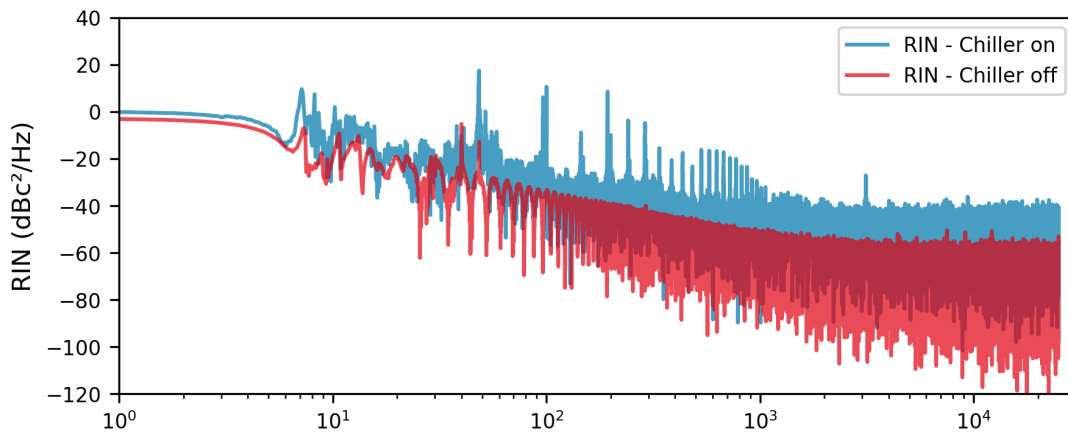


Figure C.4: Measurement of the acoustic noise of directly laser chiller had moved to another room. The strong 50 Hz peak is generated by a second optical and electrical system, which is located on the optical table. It could not be switched off at the time of the measurement. It can be seen that the peaks do not increase, when the chillers turned on, in contrast to the measurement in Fig. C.3.

do not contribute relevant noise to the optical table anymore. The broadband noise peaks around 10 Hz and 200 Hz are possibly caused by different effects, their origin is unknown. The peaks are possibly time dependent, which explains, why they appear at different frequencies. All actions together help for a significant improvement of the passive stability of the DROPO. The active stabilization in the next chapter loop is

able to reduce the noise even further.

## Additional measurements

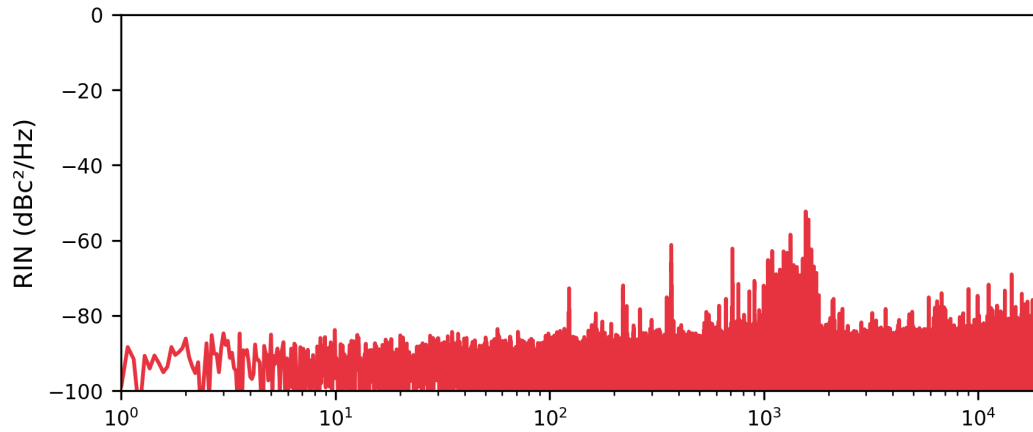


Figure C.5: Measurement of the noise of the used extended InGaAs photodiode of the measurement in Fig. 5.8. As the carrier of the RIN, the mean power of the stabilized system in Fig. 5.8 is used.



# List of Figures

2.1	Energy conservation and phase-matching in a nonlinear crystal. The energy level $E_0$ is the ground state, while the dotted lines denote virtual levels. (a) Down-conversion process: a frequency $\omega_1$ is split up in two frequencies with lower energy. (b) Sum frequency process: the inverse of the down-conversion process. (c) Phase-matching: the interacting frequencies have different wave numbers $k_{1,2,3}$ , due to their frequencies and refractive indices. The phase mismatch $\Delta k$ needs to be zero for efficient frequency mixing. . . . .	7
2.2	Examples of the analytic solution of equations (2.14) - (2.16) at degeneracy. The expected conversion of the pump (blue) to the signal wave (red) and the back conversion is displayed. (a) For $\gamma = \pm\pi/2$ , the solution shows only one cycle of nonlinear interaction. (b) When $\gamma$ is unequal to $\pm\pi/2$ , oscillation occurs in the crystal. Because of this sensitivity on the phase and input power, in a realistic OPO, virtually no stable output power is possible. . . . .	11
2.3	Longitudinal modes of a cw-DROPO. Signal (yellow) an idler (red) modes need to be simultaneously resonant in the cavity. In the top and middle panel, the signal and idler longitudinal modes are illustrated. Additionally, their free spectral range and the FWHM of the corresponding resonance $\Delta\nu_{s,i}$ are shown. Their multiplied function defines the DROPO frequency modes and the possible performance at that working point. Depending on the finesse and the pump laser frequency, the signal and idler modes need to coincide well in the cavity (dotted lines), for efficient conversion. . . . .	14

- 2.4 Crosstalk of modes in a DROPO. For example the  $n^{\text{th}}$  and  $n^{\text{th}} + 1$  pump mode of a mode-locked laser can both split in the  $l^{\text{th}}$  signal mode and separate in the  $m^{\text{th}}$  and  $m^{\text{th}} + 1$  idler mode to fulfil the energy conservation. With the amplification phase condition Eq. (2.18), a phase relation between the pump, signal and idler is made. . . . . 15
- 2.5 Scheme of the numerical model. The differential equations are solved by the split-step method. The nonlinear part is solved in the time and the impact of dispersion is calculated in the spectral domain. To complete the roundtrip, the cavity dispersion (without crystal), losses, the time and phase delays are included. Also, the high reflectivity (HR) mirrors are simulated to have optimal conditions at the borders of the high reflective wavelength region. Approximately 300 roundtrips are necessary to reach the steady state. At the end, the outcoupled power is calculated. . . . . 20
- 2.6 Simulation of the emission structure of the DROPO obtained with the split-step based model. The cavity is detuned by a couple of micrometers. Here, a crystal length of 1 mm and an OC of 0.05% is chosen. The GDD is set to  $0 \text{ fs}^2$  and the TOD to  $20000 \text{ fs}^3$ . Detuning resonances with a typical width of a few tens of nanometers appear. (a) Emission behaviour when the pump power is increased. Depending on the threshold of every detuning resonance, individual slopes can be observed. (b) Spectrum near degeneracy with 20 W pump power. At exactly one half of the pump frequency, several peaks appear. The DROPO is switching from the non-degenerated regime to the self-phase locking state. . . . 22
- 3.1 Properties of the Yb:YAG pump laser for the DROPO. (a)  $\text{sech}^2$ -shaped optical output spectrum of the laser. The recalculated spectral width is around 3.9 nm (FWHM). (b) Autocorrelation of the pulse. The pulse duration for a sech pulse is 306 fs (FWHM). (c) RF spectrum of the pump laser. (d) Gaussian beam profile of the pump. . . . . 26

- 3.2 Scheme of the DROPO setup. The power of the thin-disk laser (blue) is controlled by a thin-film polarizer (TFP) in combination with a  $\lambda/2$  - wave plate and a beam block (BB). A second wave plate rotates the polarization for efficient pumping and a lens ( $f = 400$  mm) is focussing the pump into the BBO crystal. The crystal has a thickness between 1 mm and 3 mm. The DROPO cavity (red) has two focussing mirror pairs with radii of curvature (ROC) of 300 mm and 500 mm. Positive and negative dispersive material can be inserted into the DROPO cavity to control the higher-order dispersion terms. The length can be tuned by a piezo translation stage (PZT). The light is coupled out by an output coupling mirror (OC). . . . . 27
- 3.3 Phase-matching of a BBO crystal for difference frequency generation in dependency of the crystal angle  $\theta$  and the wavelength of the down-converted light. The pump wavelength is 1030 nm. The crystal length in this simulation is  $L_c = 2$  mm. At  $\theta = 21.3^\circ$ , the degeneracy point is phase-matched. At this point, the phase-matching is relatively broadband and allows a wide tuneability of the system. . . . . 29
- 3.4 Calculated beam waist radius in sagittal and tangential direction for different mode parameters in the used bow-tie cavity. (a-c) The tuning of the curved mirror distance  $l$  of one focal spot can be compensated by the other mirror set by maintaining the maximum of stability in the cavity. In Tab. 3.1, the distances  $l$  and the corresponding beam waists  $w$  in the focus are presented. . . . . 30
- 3.5 Experimental measurements of discret detuning resonances at the degeneracy of the DROPO, when the cavity length is detuned. The parameters of the inserted optical plates, crystals and OC are presented in the small gray box. The theoretically predicted roundtrip phase-matching resonances are presented as gray dotted lines. (a-c) DROPO resonances, with negative, zero and positive intracavity GDD. The curvature of the resonances, which is described by Eq. (3.4), can be clearly seen. . . . . 35

- 3.6 Experimental measurements of the global spectral detuning characteristics of the DROPO (see also [67]). The gray bars left and right indicate the borders of the HR mirrors. The white continuous line is the group delay curve from Eq. (3.5), which describes the synchronized wavelengths with the pump. The white dotted lines symbolize the non-group-matched colors in the non-zero GDD regime. (a,c) X-shaped structure with negative or positive GDD. (b) Inverse Y-shaped structure with self-phase locked regime at the top. The GDD is set to zero. . . . . 36
- 3.7 Experimental measurements with a 3 mm crystal, 16 W pump power and 0.5% output coupling for different values of intracavity dispersion. Even when the DROPO is detuned on large scales, DROPO resonances can be measured. The consistency between Eq. (3.4 - 3.5) and the experiment can be seen, too. . . . . 39
- 3.8 Split-Step based simulation of the DROPO (see also in [67]) with the numerical model of Sec. 2.6. The influence of the round-trip phase condition and the group delay matching can be recognized. The simulations are in good agreement with the experimental measurements, presented in Fig. 3.6. . . . . 41
- 3.9 (a-b) Experimental measurements with  $GDD = 0 \text{ fs}^2$  and different TODs (see also in [67]). (c-d) Corresponding simulations. (e) Sum of relative cavity time detuning of all degenerated resonances in dependence of the TOD. . . . . 42
- 3.10 Left: detuning resonances of a DROPO. The beam profile and optical spectrum is measured simultaneously when the cavity length is detuned. A 2 mm crystal with an OC of 2% is used. Right: beam profile measured with a CCD camera. The theoretically predicted detuning resonances (b,d) and extraordinary ones (a,c) correspond to  $TEM_{00}$  and  $TEM_{10}$  transversal modes. . . . . 44

- 3.11 Detuning of the nonlinear crystal angle  $\theta$ . In the top row slices of the phase-matching curve in Fig. 3.3 for different crystal thicknesses are presented. In the bottom row the experimental results are shown. With the optimal phase-matching angle the degenerated and non-degenerated regime of the DROPO can be measured (b,e). Small detuning of the angle can lead to emission at degeneracy only (a,d) or outside in the non-degenerated regime (c,f). . . . . 45
- 3.12 Single DROPO resonance at degeneracy for a cavity with negative GDD in dependence of the pump power. When the pump power is increased, the DROPO wavelength regions change. The DROPO can be tuned continuously on one resonance from the non-degenerated frequencies to the degeneracy. . . . . 47
- 4.1 Change of pump  $|a_p|^2$  (blue) and signal  $|a_s|^2$  (red) when they propagate through the crystal. The dotted lines indicate the field amplitudes from Eq. (4.6) and (4.7) for infinite crystal lengths. The continuous line shows the transformation dynamics between an incident pump and signal for different crystal lengths (a-c). The state of the pump at the end of the crystal is shown in a red circle. (a) Conversion in the case when the crystal is too short, so that the pump is not fully converted to the signal. (b) The evolution for the optimal crystal length, where the pump is fully converted at the end of the crystal. (c) In a long crystal the pump is fully converted to the signal and significant back conversion takes place. 51
- 4.2 Solution of Eq. (4.10) for  $\alpha = 0.5$ . The enhancement  $\eta = a_s^2/a_p^2$  is nonlinear to the pump power. Three situations can be recognized: (1) below OPO threshold, (2) pump is not fully depleted and (3) back conversion takes place. . . . . 53



- 4.3 Results of the model for the plane wave (PW) and Gaussian approximation. (a) Dependence of the enhancement on the pump power for different losses. The maximum enhancement decreases and shifts to higher pump values in the case of higher losses. The dashed lines show the Gaussian approximation with  $w_s/w_p = 1/\sqrt{2}$ . The inefficiencies due to spatial overlap further reduce the enhancement. (b) The crystal length determines at which pump power the enhancement is the highest. For short crystals, this point shifts to higher pump powers. . . . . 55
- 4.4 Results of the model for the plane wave (PW) and Gaussian approximation. (a) Pump depletion  $D$  and conversion efficiency  $N$  for the 10% loss case. The dashed line shows the Gaussian approximation for  $w_p = w_s$ . Here, the pump beam is not fully converted. (b) The maximum efficiency (blue line) for the Gaussian approximation in dependence of the mode size ratio (top x-axis) between signal and pump for a calculated loss of the cavity of  $\alpha = 0.2$ . The red line shows the dependence of the maximum efficiency in relation to the losses (bottom x-axis) for  $w_p/w_s = \sqrt{2}$ . . . . . 58
- 4.5 Experimental setup for measurements of the intracavity power in a DROPO. The output power is detected by a fast integrating sphere power meter (ISP) and the pump power is measured from the leakage behind an HR mirror. The pump power can be tuned by a motorized wave plate in combination with a thin film polarizer (TFP). The cavity length is controlled with a piezo translation stage (PZT). . . . . 59
- 4.6 (a-c) Experimental measurements of the enhancement in the DROPO cavity for different crystal lengths (see also in [105]). The enhancement is measured with different pump powers and relative cavity length detunings with an OC of 0.5%. Depending on the pump power, the enhancement first increases to a maximum value and then decreases again. The thinner the crystal, the higher the intracavity powers that can be achieved. The maximum of enhancement is circled in blue. (d-e) Corresponding spectral behaviour when the cavity length is detuned. The spectrum is measured at a pump power of 12.5 W. Due to the non-compensated GDD, the resonances are slightly curved, defined by Eq. (3.4). . . . . 61

4.7	Fit of the reduced experimental measurements from Fig. 4.6 (crosses) with the iterative model, described in Section 4.2 (lines). . . . .	63
4.8	Fit of the reduced experimental measurements from Fig. 4.6 (crosses) with the split-step model, described in Chapter 2.6 (dotted lines). The fit parameters are presented in Tab. 4.4. . . . .	65
4.9	(a) Simulation of the split-step model from Chapter 2 with $L_c = 1$ mm, $\alpha = 20\%$ , $OC = 0.5\%$ , $w_{p,s} = 110$ $\mu\text{m}$ , $GDD = 0$ $\text{fs}^2$ and $TOD = 12000$ $\text{fs}^3$ . For the discussion of the dependence of the GDD and TOD in (b) and (c), the circled resonance is chosen as an reference. (b) Dependence of the maximum enhancement on the GDD. When the GDD (red curves) is tuned, the TOD is fixed to $12000$ $\text{fs}^3$ . At zero GDD, the enhancement slightly decreases, due to shorter pulses. (c) When the TOD is varied, the GDD is set to zero. The enhancement increases slightly for higher TOD values. . . . .	66
4.10	Experimental measurements of the detuning resonance width in dependence of the pumping above threshold $P/P_{th}$ . With higher output coupling and pumping the width of the detuning resonances increases. Equation (4.27) has been fitted to the data. The internal losses of the cavity add up to around 8% and 13%. . . . .	68
5.1	Schematic explanation of the connection of the DROPO resonance (blue) and the SFG output (red). The PI controller alters the cavity length, so that $e(t) = 0$ . Here, the set point is chosen so that the DROPOs output power is maximum. . . . .	73
5.2	Simulation of the SF signal of one detuning resonance at the zero GDD point and a crystal length of 3 mm. (a) Spectral behaviour in dependence of the SF signal. The simulated bandpass filter is indicated by the two blue lines, which show the borders of the filter. (b) Simulated filtered SF signal and DROPO signal power in dependence of the cavity length detuning. The slope (yellow line) of the SF signal can be used as the feedback signal. . . . .	75

- 5.3 Experimental setup: Measurement of the SF signal (dark red) for the active stabilization of the system. The SF signal is generated in the crystal and partly reflected by the HR mirrors. It is separated from the signal by a long pass filter. By rotating a bandpass filter to transmit the spectral components around 695 nm a suitable error signal can be obtained. The transmitted power of this SFG signal shows a slope when the cavity length  $\Delta L$  is detuned (see inset scheme). A silicon photodiode detects the filtered SF light as input for the PI controller. The controller stabilizes the cavity with two piezo actuators inside the DROPO (PZT 1 and 2). . . . . 76
- 5.4 Spectral transmission of the Thorlabs FB700-10 bandpass filter, when the filter is tilted. The spectrum is measured with a white light source (NKT Photonics SuperK EVO) and a spectrometer (Ocean Optics HR2000). A change of the central transmission wavelength to lower wavelengths for higher filter AOI is visible. . . . . 78
- 5.5 Stabilization scheme of the PI controller. After amplification of the error signal  $e(t)$  the signal is split in two electronic branches, one for the P-part and one for the I-part. The P-part moves a fast piezo ceramic tube, while the I part is controlling a slower piezo system (piezosystem jena TRITOR 100), which can cover a larger detuning range. The DROPO output can be tuned with the setpoint  $r$  in power. . . . . 78
- 5.6 (a) Optical spectrum of the DROPO around the degeneracy when the cavity length is detuned. (b) SFG optical spectrum. . . . . 80
- 5.7 (a,d,g,j) Optical spectrum of the DROPO resonance in Fig. 5.6 at 0  $\mu\text{m}$  cavity length detuning. (b,e,h,k) Corresponding filtered SF signal for different filter AOI. The borders of the bandpass filter are marked in dotted blue lines. (c,f,i,l) Measured output power of the DROPO's signal (red) and the SF signal (blue). With optimal filtering, the SF signal shows a slope (yellow line), which can be used as a feedback signal (i,l). . . . . 81

5.8	RIN of the signal output of the DROPO for the non-stabilized case (blue) and active PI stabilization (red) (see also [108]). A strong reduction of the noise can be recognized. Small peaks remain, which can be possibly corrected by a redesign of the PI controller in the future. The cumulative RIN for the stabilized system is 0.44%, which is comparable with [44]. In the long time measurement, an output power of $(2.48 \pm 0.04)$ W is achieved. . . . .	83
5.9	Optical spectrum of the DROPO at degeneracy. The spectrum is the mean value of a 4 min long measurement with a spectrometer integration time of 100 ms. The spectral width is around 37 nm. For Fourier-transform limited pulses a pulse duration around 120 fs can be calculated.	84
5.10	Self-phase locking of the DROPO. The second harmonic of the DROPO and pump are overlapped and measured with a photodiode connected to an RF spectrometer and with a CCD chip. (a) In the non-degenerated mode no interference can be measured and beating notes appear. (b) Self-locking mode: a stable interference can be measured and the beating notes are suppressed. . . . .	86
6.1	Results of the simulation of a DROPO system with a fast saturable absorber (blue) and without one (red). (a) Optical spectrum of the DROPO. The mirrors are highly reflective between 1950 nm – 2150 nm. (b) Temporal shape of both cases. . . . .	92
A.1	Spectral behaviour if the cavity length is detuned. The GDD is set to zero. The TOD is is tuned from the negative to positive region. . . . .	107
A.2	Spectral behaviour if the cavity length is detuned. The TOD is set to zero. The GDD is is tuned from the negative to positive region. . . . .	108
A.3	Simulation of the filtered SF signal for 4 mm BBO crystal and at the zero GDD point. The asymmetric shape of the spectral response when the cavity length is detuned is clearly visible. . . . .	108
A.4	Simulation of the filtered SF signal for negative, zero and positive GDD (2 mm BBO crystal). . . . .	109
B.1	LT SPICE circuit diagram of the PI controller . . . . .	115

- C.1 Spectral behavior when the cavity length of the OPO is detuned, depending on the alignment. (a) Singly resonant mode. Due to clipping on mirrors or other misalignments, only signal or idler is fully resonant in the cavity. The output power and performance of this system is relatively stable, but this state should be avoided due to bad spectral and spatial performance. (b) Example of a well aligned system. The detuning resonances of the doubly resonant operation are well recognizable. Also, the distinct degeneracy regime is accessible. . . . . 118
- C.2 Measurement of the SF signal of the free running DROPO. (a) The SF signal is measured with a photodiode and an oscilloscope for 10 seconds. (b) The Fourier transform of (a) is calculated. Peaks around the mains frequency (50 Hz) and its higher harmonics can be recognized. . . . . 120
- C.3 Acoustic noise on the optical table with activated and turned off water chillers for the laser cooling. It can be seen that in the range of 50 until 300 Hz strong peaks appear (yellow circles) in the case where the chillers turned on. A solution is to relocate the chillers to suppress their influence. The broadband noise peaks at 3 Hz, 10 Hz and 200 Hz and their shift to higher frequencies are not necessary correlated to the chillers and are caused by unknown influences or effects. . . . . 121
- C.4 Measurement of the acoustic noise of directly laser chiller had moved to another room. The strong 50 Hz peak is generated by a second optical and electrical system, which is located on the optical table. It could not be switched off at the time of the measurement. It can be seen that the peaks do not increase, when the chillers turned on, in contrast to the measurement in Fig. C.3. . . . . 122
- C.5 Measurement of the noise of the used extended InGaAs photodiode of the measurement in Fig. 5.8. As the carrier of the RIN, the mean power of the stabilized system in Fig. 5.8 is used. . . . . 123

# List of Tables

3.1	Focal beam waist radius $w_{1,2}$ in dependence of the mirror distances $l_{1,2}$ .	31
3.2	GVD and TOD for different materials with $\lambda_0 = 2064$ nm . . . . .	32
3.3	Constants and variables for the numerical model . . . . .	40
4.1	Transmission of optical elements in the enhancement measurement setup.	60
4.2	Intracavity GDD and TOD of the DROPO cavity for different crystal lengths. . . . .	60
4.3	Fitting parameters in Fig. 4.7 . . . . .	63
4.4	Fitting parameters in Fig. 4.8 . . . . .	64



# Bibliography

- [1] T. H. Maiman, “Stimulated optical radiation in ruby,” *Nature*, vol. 187, no. 4736, pp. 493–494, 1960.
- [2] P. A. Franken, A. E. Hill, C. W. Peters, and G. Weinreich, “Generation of optical harmonics,” *Phys. Rev. Lett.*, vol. 7, pp. 118–119, Aug 1961.
- [3] R. W. Boyd, *Nonlinear Optics, Third Edition*. USA: Academic Press, Inc., 3rd ed., 2008.
- [4] G. New, *Introduction to Nonlinear Optics*. Cambridge University Press, 2011.
- [5] P. Powers and J. Haus, *Fundamentals of Nonlinear Optics*. Boca Raton: Taylor & Francis Group, 2nd ed., 2017.
- [6] A. Berrou, M. Raybaut, A. Godard, and M. Lefebvre, “High-resolution photoacoustic and direct absorption spectroscopy of main greenhouse gases by use of a pulsed entangled cavity doubly resonant opo,” *Applied Physics B*, vol. 98, p. 217, Sep 2009.
- [7] A. Godard, G. Aoust, J. Armougom, E. Cadiou, D. Descloux, G. Walter, J.-B. Dherbecourt, G. Gorju, J.-M. Melkonian, M. Raybaut, and M. Lefebvre, “Optical parametric sources for gas sensing applications,” in *Quantum Sensing and Nano Electronics and Photonics XIV* (M. Razeghi, ed.), vol. 10111, pp. 445 – 463, International Society for Optics and Photonics, SPIE, 2017.
- [8] S. T. Wong, K. L. Vodopyanov, and R. L. Byer, “Self-phase-locked divide-by-2 optical parametric oscillator as a broadband frequency comb source,” *J. Opt. Soc. Am. B*, vol. 27, pp. 876–882, May 2010.



- [9] A. Khodabakhsh, L. Rutkowski, J. Morville, and A. Foltynowicz, “Mid-infrared continuous-filtering vernier spectroscopy using a doubly resonant optical parametric oscillator,” *Applied Physics B*, vol. 123, p. 210, Jul 2017.
- [10] Y. S. Cheng, D. Xiao, R. A. McCracken, and D. T. Reid, “Laser-frequency-comb calibration for the extremely large telescope: an opo-based infrared astrocomb covering the h and j bands,” *J. Opt. Soc. Am. B*, vol. 38, pp. A15–A20, Jul 2021.
- [11] M. Calvanese Strinati, D. Pierangeli, and C. Conti, “All-optical scalable spatial coherent ising machine,” *Phys. Rev. Applied*, vol. 16, p. 054022, Nov 2021.
- [12] Y. Yamamoto, K. Aihara, T. Leleu, K.-i. Kawarabayashi, S. Kako, M. Fejer, K. Inoue, and H. Takesue, “Coherent ising machines - optical neural networks operating at the quantum limit,” *npj Quantum Information*, vol. 3, p. 49, Dec 2017.
- [13] F. Brunel, “Harmonic generation due to plasma effects in a gas undergoing multiphoton ionization in the high-intensity limit,” *J. Opt. Soc. Am. B*, vol. 7, pp. 521–526, Apr 1990.
- [14] I. Babushkin, C. Brée, C. M. Dietrich, A. Demircan, U. Morgner, and A. Husakou, “Terahertz and higher-order brunel harmonics: from tunnel to multiphoton ionization regime in tailored fields,” *Journal of Modern Optics*, vol. 64, no. 10-11, pp. 1078–1087, 2017.
- [15] I. Babushkin, A. J. Galan, V. Vaičaitis, A. Husakou, F. Morales, A. Demircan, J. R. C. Andrade, U. Morgner, and M. Ivanov, “Optical attoclock using terahertz radiation,” in *2019 Conference on Lasers and Electro-Optics Europe European Quantum Electronics Conference (CLEO/Europe-EQEC)*, pp. 1–1, 2019.
- [16] D. Shafir, H. Soifer, B. D. Bruner, M. Dagan, Y. Mairesse, S. Patchkovskii, M. Y. Ivanov, O. Smirnova, and N. Dudovich, “Resolving the time when an electron exits a tunnelling barrier,” *Nature*, vol. 485, pp. 343–346, May 2012.
- [17] J. A. Giordmaine and R. C. Miller, “Tunable Coherent Parametric Oscillation in  $\text{LiNbO}_3$  at Optical Frequencies,” *Phys. Rev. Lett.*, vol. 14, pp. 973–976, Jun 1965.

- [18] H. Komine, “Beta-barium borate optical parametric oscillator,” in *International Conference on Quantum Electronics*, p. ThI3, Optical Society of America, 1988.
- [19] J. Q. YAO, J. T. LIN, N. DUE, and Z. LIU, “Analyses of bbo and ktp crystals for optical parametric oscillation,” in *Conference on Lasers and Electro-Optics*, p. TUJ5, Optical Society of America, 1988.
- [20] M. Yamada, N. Nada, M. Saitoh, and K. Watanabe, “First order quasi-phase matched linbo3 waveguide periodically poled by applying an external field for efficient blue second-harmonic generation,” *Applied Physics Letters*, vol. 62, no. 5, pp. 435–436, 1993.
- [21] L. A. Pomeranz, P. G. Schunemann, D. J. Magarrell, J. C. McCarthy, K. T. Zawilski, and D. E. Zelmon, “1  $\mu\text{m}$  OPO based on orientation-patterned GaP,” in *Nonlinear Frequency Generation and Conversion: Materials, Devices, and Applications XIV* (K. L. Vodopyanov, ed.), vol. 9347, pp. 129 – 135, International Society for Optics and Photonics, SPIE, 2015.
- [22] K. Burneika, M. Ignatavicius, V. Kabelka, A. Piskarskas, and A. Stabinis, “Parametric light amplification and oscillation in kdp with mode-locked pump,” *IEEE Journal of Quantum Electronics*, vol. 8, no. 6, pp. 574–574, 1972.
- [23] J. E. Bjorkholm, “Efficient optical parametric oscillation using doubly and singly resonant cavities,” *Applied Physics Letters*, vol. 13, no. 2, pp. 53–56, 1968.
- [24] G. M. Gale, M. Cavallari, T. J. Driscoll, and F. Hache, “Sub-20-fs tunable pulses in the visible from an 82-mhz optical parametric oscillator,” *Opt. Lett.*, vol. 20, pp. 1562–1564, Jul 1995.
- [25] S. Chaitanya Kumar, A. Esteban-Martin, T. Ideguchi, M. Yan, S. Holzner, T. W. Hänsch, N. Picqué, and M. Ebrahim-Zadeh, “Few-cycle, broadband, mid-infrared optical parametric oscillator pumped by a 20-fs ti:sapphire laser,” *Laser & Photonics Reviews*, vol. 8, no. 5, pp. L86–L91, 2014.
- [26] T. Lang, T. Binhammer, S. Rausch, G. Palmer, M. Emons, M. Schultze, A. Harth, and U. Morgner, “High power ultra-widely tuneable femtosecond pulses from a non-collinear optical parametric oscillator (nopo),” *Opt. Express*, vol. 20, pp. 912–917, Jan 2012.

- [27] R. Mevert, Y. Binhammer, C. M. Dietrich, L. Beichert, J. R. C. de Andrade, T. Binhammer, J. Fan, and U. Morgner, “Widely tunable, high-power, femtosecond noncollinear optical parametric oscillator in the visible spectral range,” *Photon. Res.*, vol. 9, pp. 1715–1718, Sep 2021.
- [28] J. Falk, “Instabilities in the doubly resonant parametric oscillator: A theoretical analysis,” *IEEE Journal of Quantum Electronics*, vol. 7, no. 6, pp. 230–235, 1971.
- [29] J. E. Bjorkholm, “Some spectral properties of doubly and singly resonant pulsed optical parametric oscillators,” *Applied Physics Letters*, vol. 13, no. 12, pp. 399–401, 1968.
- [30] L.-A. Wu, M. Xiao, and H. J. Kimble, “Squeezed states of light from an optical parametric oscillator,” *J. Opt. Soc. Am. B*, vol. 4, pp. 1465–1475, Oct 1987.
- [31] S. Jin and M. Xiao, “Extra intracavity squeezing of a degenerate optical parametric oscillator coupling with  $n$  two-level atoms,” *Phys. Rev. A*, vol. 49, pp. 499–505, Jan 1994.
- [32] M. Wolinsky and H. Carmichael, “Squeezing in the degenerate parametric oscillator,” *Optics Communications*, vol. 55, no. 2, pp. 138 – 142, 1985.
- [33] W. H. Louisell, A. Yariv, and A. E. Siegman, “Quantum fluctuations and noise in parametric processes. i,” *Phys. Rev.*, vol. 124, pp. 1646–1654, Dec 1961.
- [34] C. D. Nabors, S. T. Yang, T. Day, and R. L. Byer, “Coherence properties of a doubly resonant monolithic optical parametric oscillator,” *J. Opt. Soc. Am. B*, vol. 7, pp. 815–820, May 1990.
- [35] K. L. Vodopyanov, E. Sorokin, I. T. Sorokina, and P. G. Schunemann, “Mid-ir frequency comb source spanning 4.4 - 5.4  $\mu\text{m}$  based on subharmonic gas optical parametric oscillator,” *Opt. Lett.*, vol. 36, pp. 2275–2277, Jun 2011.
- [36] K. A. Ingold, A. Marandi, C. W. Rudy, K. L. Vodopyanov, and R. L. Byer, “Fractional-length sync-pumped degenerate optical parametric oscillator for 500-mhz 3- $\mu\text{m}$  mid-infrared frequency comb generation,” *Opt. Lett.*, vol. 39, pp. 900–903, Feb 2014.

- [37] M. W. Haakestad, T. P. Lamour, N. Leindecker, A. Marandi, and K. L. Vodopyanov, “Intracavity trace molecular detection with a broadband mid-ir frequency comb source,” *J. Opt. Soc. Am. B*, vol. 30, pp. 631–640, Mar 2013.
- [38] M. Vainio and J. Karhu, “Fully stabilized mid-infrared frequency comb for high-precision molecular spectroscopy,” *Opt. Express*, vol. 25, pp. 4190–4200, Feb 2017.
- [39] J. Roslund, R. M. De Araujo, S. Jiang, C. Fabre, and N. Treps, “Wavelength-multiplexed quantum networks with ultrafast frequency combs,” *Nature Photonics*, vol. 8, no. 2, p. 109, 2014.
- [40] S. Yokoyama, R. Ukai, S. C. Armstrong, C. Sornphiphatphong, T. Kaji, S. Suzuki, J.-i. Yoshikawa, H. Yonezawa, N. C. Menicucci, and A. Furusawa, “Ultra-large-scale continuous-variable cluster states multiplexed in the time domain,” *Nature Photonics*, vol. 7, no. 12, p. 982, 2013.
- [41] M. Jankowski, A. Marandi, C. R. Phillips, R. Hamerly, K. A. Ingold, R. L. Byer, and M. M. Fejer, “Temporal simultons in optical parametric oscillators,” *Phys. Rev. Lett.*, vol. 120, p. 053904, Feb 2018.
- [42] C. Ning and Z. Zhang, “Multi-soliton formation in femtosecond degenerate optical parametric oscillators,” *Opt. Lett.*, vol. 45, pp. 734–737, Feb 2020.
- [43] N. Leindecker, A. Marandi, R. L. Byer, and K. L. Vodopyanov, “Broadband degenerate opo for mid-infrared frequency comb generation,” *Opt. Express*, vol. 19, pp. 6296–6302, Mar 2011.
- [44] Y. S. Cheng, R. A. McCracken, and D. T. Reid, “Dither-free stabilization of a femtosecond doubly resonant opo using parasitic sum-frequency mixing,” *Opt. Lett.*, vol. 45, pp. 768–771, Feb 2020.
- [45] P. Salén, M. Basini, S. Bonetti, J. Hebling, M. Krasilnikov, A. Y. Nikitin, G. Shamuilov, Z. Tibai, V. Zhaunerchyk, and V. Goryashko, “Matter manipulation with extreme terahertz light: Progress in the enabling thz technology,” *Physics Reports*, vol. 836-837, pp. 1 – 74, 2019. Matter manipulation with extreme terahertz light: Progress in the enabling THz technology.

- [46] H. Hirori, A. Doi, F. Blanchard, and K. Tanaka, “Single-cycle terahertz pulses with amplitudes exceeding 1 mv/cm generated by optical rectification in linbo3,” *Applied Physics Letters*, vol. 98, no. 9, p. 091106, 2011.
- [47] A. Nahata, A. S. Weling, and T. F. Heinz, “A wideband coherent terahertz spectroscopy system using optical rectification and electro-optic sampling,” *Applied Physics Letters*, vol. 69, no. 16, pp. 2321–2323, 1996.
- [48] D. N. Nikogosyan, *Nonlinear Optical Crystals: A Complete Survey*. Springer Science+Business Media, 01 2005.
- [49] R. Sutherland, *Handbook of Nonlinear Optics*. Boca Raton: Taylor & Francis Group, 2nd ed., 2003.
- [50] G. Cerullo and S. De Silvestri, “Ultrafast optical parametric amplifiers,” *Review of Scientific Instruments*, vol. 74, no. 1, pp. 1–18, 2003.
- [51] J.-C. Diels and W. Rudolph, *Ultrashort Laser Pulse Phenomena (Second Edition)*. Burlington: Academic Press, 2006.
- [52] A. M. Weiner, *Ultrafast Optics*. Hoboken, New Jersey: John Wiley & Sons, Ltd, 1st ed., 2008.
- [53] J. A. Armstrong, N. Bloembergen, J. Ducuing, and P. S. Pershan, “Interactions between light waves in a nonlinear dielectric,” *Phys. Rev.*, vol. 127, pp. 1918–1939, Sep 1962.
- [54] M. Pollnau and M. Eichhorn, “Spectral coherence, part i: Passive-resonator linewidth, fundamental laser linewidth, and schawlow-townes approximation,” *Progress in Quantum Electronics*, vol. 72, p. 100255, 2020.
- [55] W. Lauterborn and T. Kurz, *Coherent Optics: Fundamentals and Applications*. Berlin, Heidelberg: Springer-Verlag, 2nd ed., 2003.
- [56] C. Rullière, *Femtosecond Laser Pulses*. New York: Springer, 2005.
- [57] A. Henderson, M. Padgett, F. Colville, J. Zhang, and M. Dunn, “Doubly-resonant optical parametric oscillators: tuning behaviour and stability requirements,” *Optics Communications*, vol. 119, no. 1, pp. 256 – 264, 1995.

- [58] M. Padgett, F. Colville, and M. Dunn, “Mode selection in doubly-resonant optical parametric oscillators,” *IEEE Journal of Quantum Electronics*, vol. 30, no. 12, pp. 2979–2985, 1994.
- [59] R. C. Eckardt, C. D. Nabors, W. J. Kozlovsky, and R. L. Byer, “Optical parametric oscillator frequency tuning and control,” *J. Opt. Soc. Am. B*, vol. 8, pp. 646–667, Mar 1991.
- [60] S. Harris, “Threshold of multimode parametric oscillators,” *IEEE Journal of Quantum Electronics*, vol. 2, no. 10, pp. 701–702, 1966.
- [61] S. Wong, *Self-phase-locking of degenerate synchronously pumped optical parametric oscillators*. PhD thesis, Stanford University, 2008.
- [62] B. Nandy, S. C. Kumar, and M. Ebrahim-Zadeh, “Phase-locked picosecond optical parametric oscillator,” *Opt. Lett.*, vol. 45, pp. 3981–3984, Jul 2020.
- [63] S. T. Wong, T. Plettner, K. L. Vodopyanov, K. Urbanek, M. Dignonnet, and R. L. Byer, “Self-phase-locked degenerate femtosecond optical parametric oscillator,” *Opt. Lett.*, vol. 33, pp. 1896–1898, Aug 2008.
- [64] H. L. Stover and W. H. Steier, “Locking of laser oscillators by light injection,” *Applied Physics Letters*, vol. 8, no. 4, pp. 91–93, 1966.
- [65] C. Ning, P. Liu, Y. Qin, and Z. Zhang, “Continuous wavelength tuning of nondegenerate femtosecond doubly resonant optical parametric oscillators,” *Opt. Lett.*, vol. 45, pp. 2551–2554, May 2020.
- [66] A. Yariv, *Quantum Electronics*. John Wiley & Sons, 3rd ed., 1988.
- [67] C. M. Dietrich, I. Babushkin, J. R. C. de Andrade, H. Rao, A. Demircan, and U. Morgner, “Higher-order dispersion and the spectral behavior in a doubly resonant optical parametric oscillator,” *Opt. Lett.*, vol. 45, pp. 5644–5647, Oct 2020.
- [68] R. Hamerly, A. Marandi, M. Jankowski, M. M. Fejer, Y. Yamamoto, and H. Mabuchi, “Reduced models and design principles for half-harmonic generation in synchronously pumped optical parametric oscillators,” *Phys. Rev. A*, vol. 94, p. 063809, Dec 2016.

- [69] T. Lang, *Ultrashort Laser Pulses from Optical Parametric Amplifiers And Oscillators*. PhD thesis, Gottfried Wilhelm Leibniz Universität Hannover, 07 2014.
- [70] A. V. Husakou and J. Herrmann, “Supercontinuum generation of higher-order solitons by fission in photonic crystal fibers,” *Phys. Rev. Lett.*, vol. 87, p. 203901, Oct 2001.
- [71] M. Conforti, F. Baronio, and C. De Angelis, “Nonlinear envelope equation for broadband optical pulses in quadratic media,” *Phys. Rev. A*, vol. 81, p. 053841, May 2010.
- [72] D. Zhang, Y. Kong, and J. yuan Zhang, “Optical parametric properties of 532-nm-pumped beta-barium-borate near the infrared absorption edge,” *Optics Communications*, vol. 184, no. 5, pp. 485 – 491, 2000.
- [73] G. Agrawal, *Nonlinear Fiber Optics*. Optics and Photonics, Elsevier Science, 2013.
- [74] C. M. Dietrich, J. R. C. Andrade, H. Rao, A. Demircan, I. Babushkin, and U. Morgner, “On the role of higher order dispersion in a doubly resonant optical parametric oscillator,” in *2020 Conference on Lasers and Electro-Optics (CLEO)*, pp. 1–2, 2020.
- [75] H. Rao, C. M. Dietrich, J. R. Andrade, A. Demircan, I. Babushkin, and U. Morgner, “A stabilized doubly resonant opo for thz applications.” Conference on Lasers and Electro-Optics/Europe - European Quantum Electronics Conference (CLEO/EU), submitted 28rd January 2021.
- [76] J. R. C. Andrade, *High power Kerr-lens mode-locked thin-disk oscillators*. PhD thesis, Gottfried Wilhelm Leibniz University of Hannover, 08 2020.
- [77] V. G. Dmitriev, G. G. Gurzadyan, and D. N. Nikogosyan, *Handbook of Nonlinear Optical Crystals*. Springer Science+Business Media, 01 1997.
- [78] D. J. Armstrong, W. J. Alford, T. D. Raymond, and A. V. Smith, “Absolute measurement of the effective nonlinearities of ktp and bbo crystals by optical parametric amplification,” *Appl. Opt.*, vol. 35, pp. 2032–2040, Apr 1996.

- [79] K. Mecseki, M. K. R. Windeler, M. J. Prandolini, J. S. Robinson, J. M. Fraser, A. R. Fry, and F. Tavella, “High-power dual mode IR and NIR OPCPA ,” in *High-Power, High-Energy, and High-Intensity Laser Technology IV* (J. Hein and T. J. Butcher, eds.), vol. 11033, pp. 65 – 75, International Society for Optics and Photonics, SPIE, 2019.
- [80] D. Ristau and T. Gross, “Ion beam sputter coatings for laser technology,” in *Advances in Optical Thin Films II* (C. Amra, N. Kaiser, and H. A. Macleod, eds.), vol. 5963, pp. 315 – 326, International Society for Optics and Photonics, SPIE, 2005.
- [81] I. H. Malitson, “Interspecimen comparison of the refractive index of fused silica,” *J. Opt. Soc. Am.*, vol. 55, pp. 1205–1209, Oct 1965.
- [82] H. H. Li, “Refractive index of alkaline earth halides and its wavelength and temperature derivatives,” *Journal of Physical and Chemical Reference Data*, vol. 9, no. 1, pp. 161–290, 1980.
- [83] D. T. F. Marple, “Refractive index of znse, znte, and cdte,” *Journal of Applied Physics*, vol. 35, no. 3, pp. 539–542, 1964.
- [84] J. Wei, J. M. Murray, J. O. Barnes, D. M. Krein, P. G. Schunemann, and S. Guha, “Temperature dependent sellmeier equation for the refractive index of gap,” *Opt. Mater. Express*, vol. 8, pp. 485–490, Feb 2018.
- [85] C. D. Salzberg and J. J. Villa, “Infrared refractive indexes of silicon germanium and modified selenium glass,” *J. Opt. Soc. Am.*, vol. 47, pp. 244–246, Mar 1957.
- [86] T. Skauli, P. S. Kuo, K. L. Vodopyanov, T. J. Pinguet, O. Levi, L. A. Eyres, J. S. Harris, M. M. Fejer, B. Gerard, L. Becouarn, and E. Lallier, “Improved dispersion relations for gaas and applications to nonlinear optics,” *Journal of Applied Physics*, vol. 94, no. 10, pp. 6447–6455, 2003.
- [87] R. J. Mathar, “Refractive index of humid air in the infrared: model fits,” *Journal of Optics A: Pure and Applied Optics*, vol. 9, pp. 470–476, apr 2007.
- [88] Q. Ru, T. Kawamori, P. G. Schunemann, S. Vasilyev, S. B. Mirov, and K. L. Vodopyanov, “Two-octave-wide (3–2  $\mu\text{m}$ ) subharmonic produced in a minimally



- dispersive optical parametric oscillator cavity,” *Opt. Lett.*, vol. 46, pp. 709–712, Feb 2021.
- [89] D. N. Puzyrev and D. V. Skryabin, “Ladder of eckhaus instabilities and parametric conversion in  $\chi(2)$  microresonators,” *Communications Physics*, vol. 5, p. 138, Jun 2022.
- [90] G. Van Rossum and F. L. Drake, *Python 3 Reference Manual*. Scotts Valley, CA: CreateSpace, 2009.
- [91] C. R. Harris, K. J. Millman, S. J. van der Walt, R. Gommers, P. Virtanen, D. Cournapeau, E. Wieser, J. Taylor, S. Berg, N. J. Smith, R. Kern, M. Picus, S. Hoyer, M. H. van Kerkwijk, M. Brett, A. Haldane, J. F. del Río, M. Wiebe, P. Peterson, P. Gérard-Marchant, K. Sheppard, T. Reddy, W. Weckesser, H. Abbasi, C. Gohlke, and T. E. Oliphant, “Array programming with NumPy,” *Nature*, vol. 585, pp. 357–362, Sept. 2020.
- [92] J. D. Hunter, “Matplotlib: A 2d graphics environment,” *Computing in Science & Engineering*, vol. 9, no. 3, pp. 90–95, 2007.
- [93] P. Virtanen, R. Gommers, T. E. Oliphant, M. Haberland, T. Reddy, D. Cournapeau, E. Burovski, P. Peterson, W. Weckesser, J. Bright, S. J. van der Walt, M. Brett, J. Wilson, K. J. Millman, N. Mayorov, A. R. J. Nelson, E. Jones, R. Kern, E. Larson, C. J. Carey, Í. Polat, Y. Feng, E. W. Moore, J. VanderPlas, D. Laxalde, J. Perktold, R. Cimrman, I. Henriksen, E. A. Quintero, C. R. Harris, A. M. Archibald, A. H. Ribeiro, F. Pedregosa, P. van Mulbregt, and SciPy 1.0 Contributors, “SciPy 1.0: Fundamental Algorithms for Scientific Computing in Python,” *Nature Methods*, vol. 17, pp. 261–272, 2020.
- [94] G. Van Rossum, *The Python Library Reference, release 3.8.2*. Python Software Foundation, 2020.
- [95] G. D. Boyd and D. A. Kleinman, “Parametric interaction of focused gaussian light beams,” *Journal of Applied Physics*, vol. 39, no. 8, pp. 3597–3639, 1968.
- [96] T. Suhara and M. Fujimura, *Waveguide Nonlinear-Optic Devices*. Berlin, Heidelberg: Springer-Verlag Berlin Heidelberg, 2003.

- [97] H. Carstens, S. Holzberger, J. Kaster, J. Weitenberg, V. Pervak, A. Apolonski, E. Fill, F. Krausz, and I. Pupeza, “Large-mode enhancement cavities,” *Opt. Express*, vol. 21, pp. 11606–11617, May 2013.
- [98] N. Lilienfein, C. Hofer, M. Högner, T. Saule, M. Trubetskov, V. Pervak, E. Fill, C. Riek, A. Leitenstorfer, J. Limpert, F. Krausz, and I. Pupeza, “Temporal solitons in free-space femtosecond enhancement cavities,” *Nature Photonics*, vol. 13, no. 3, pp. 214–218, 2019.
- [99] C. Gohle, T. Udem, M. Herrmann, J. Rauschenberger, R. Holzwarth, H. A. Schuessler, F. Krausz, and T. W. Hänsch, “A frequency comb in the extreme ultraviolet,” *Nature*, vol. 436, pp. 234–237, Jul 2005.
- [100] K. K. Hansen, T. Deffge, and D. Bauer, “High-order harmonic generation in solid slabs beyond the single-active-electron approximation,” *Phys. Rev. A*, vol. 96, p. 053418, Nov 2017.
- [101] J. Brons, V. Pervak, D. Bauer, D. Sutter, O. Pronin, and F. Krausz, “Powerful 100-fs-scale kerr-lens mode-locked thin-disk oscillator,” *Opt. Lett.*, vol. 41, pp. 3567–3570, Aug 2016.
- [102] C. R. E. Baer, C. Kränkel, C. J. Saraceno, O. H. Heckl, M. Golling, R. Peters, K. Petermann, T. Südmeyer, G. Huber, and U. Keller, “Femtosecond thin-disk laser with 141 w of average power,” *Opt. Lett.*, vol. 35, pp. 2302–2304, Jul 2010.
- [103] C. M. Dietrich, I. Babushkin, J. R. C. Andrade, L. Rust, and U. Morgner, “Intracavity enhancement in a doubly resonant opo,” in *2019 Conference on Lasers and Electro-Optics (CLEO)*, pp. 1–2, 2019.
- [104] C. M. Dietrich, I. Babushkin, J. R. C. Andrade, L. Rust, and U. Morgner, “Field enhancement in an doubly resonant optical parametric oscillator,” in *2019 Conference on Lasers and Electro-Optics Europe and European Quantum Electronics Conference*, p. cf\_1-5, Optical Society of America, 2019.
- [105] C. M. Dietrich, I. Babushkin, J. R. C. Andrade, H. Rao, A. Demircan, and U. Morgner, “Field enhancement in a doubly resonant optical parametric oscillator,” *Opt. Lett.*, vol. 44, pp. 4909–4912, Oct 2019.

- 
- [106] I. Babushkin, “Simulation code and notes to [105] (please contact babushkin@iqo.uni-hannover.de for more information).,” 2019.
- [107] T. Lang, A. Harth, J. Matyschok, T. Binhammer, M. Schultze, and U. Morgner, “Impact of temporal, spatial and cascaded effects on the pulse formation in ultra-broadband parametric amplifiers,” *Opt. Express*, vol. 21, pp. 949–959, Jan 2013.
- [108] H. Rao, C. M. Dietrich, J. R. Andrade, A. Demircan, I. Babushkin, and U. Morgner, “A stabilized doubly resonant optical parametric oscillator for strong-field applications.” Conference on Lasers and Electro-Optics (CLEO/US), submitted 3rd December 2020.
- [109] Rao, H., Dietrich, C. M., Andrade, J. R. C., Demircan, A., Babushkin, I., and Morgner, U., “Terahertz radiation in tailored two-color laser fields with a stabilized doubly resonant optical parametric oscillator,” *EPJ Web Conf.*, vol. 267, p. 01008, 2022.
- [110] K. F. Lee, J. Jiang, C. Mohr, J. Bethge, M. E. Fermann, N. Leindecker, K. L. Vodopyanov, P. G. Schunemann, and I. Hartl, “Carrier envelope offset frequency of a doubly resonant, nondegenerate, mid-infrared gas optical parametric oscillator,” *Opt. Lett.*, vol. 38, pp. 1191–1193, Apr 2013.
- [111] R. A. McCracken and D. T. Reid, “Few-cycle near-infrared pulses from a degenerate 1 ghz optical parametric oscillator,” *Opt. Lett.*, vol. 40, pp. 4102–4105, Sep 2015.
- [112] M. Vainio and L. Halonen, “Stabilization of femtosecond optical parametric oscillators for infrared frequency comb generation,” *Opt. Lett.*, vol. 42, pp. 2722–2725, Jul 2017.
- [113] B. G. Lipták, *Process Control and Optimization Volume II*. Boca Raton: Taylor & Francis Group, 4th ed., 2006.
- [114] A. Visioli, *Practical PID Control (Advances in Industrial Control)*. London: Springer-Verlag London Limited, 2006.

- [115] Y. Suemura, A. Tajima, N. Henmi, H. Morimura, and H. Takahashi, “An adaptive wavelength tunable optical filter employing an angle-tuned interference filter and an intelligent digital controller,” *Journal of Lightwave Technology*, vol. 14, no. 6, pp. 1048–1055, 1996.
- [116] K. Petermann, *Laser Diode Modulation and Noise*. Dordrecht, Holland: Springer Netherlands, 3th ed., 1988.
- [117] K. Åström and T. Hägglund, “Revisiting the ziegler-nichols step response method for pid control,” *Journal of Process Control*, vol. 14, no. 6, pp. 635–650, 2004.
- [118] B. Nandy, S. C. Kumar, and M. Ebrahim-Zadeh, “Phase-locked picosecond optical parametric oscillator,” *Opt. Lett.*, vol. 45, pp. 3981–3984, Jul 2020.
- [119] I. Babushkin, S. Skupin, A. Husakou, C. Köhler, E. Cabrera-Granado, L. Bergé, and J. Herrmann, “Tailoring terahertz radiation by controlling tunnel photoionization events in gases,” *New Journal of Physics*, vol. 13, p. 123029, dec 2011.
- [120] M. Tonouchi, “Cutting-edge terahertz technology,” *Nature Photonics*, vol. 1, pp. 97–105, Feb 2007.
- [121] P. Jepsen, D. Cooke, and M. Koch, “Terahertz spectroscopy and imaging - modern techniques and applications,” *Laser & Photonics Reviews*, vol. 5, no. 1, pp. 124–166, 2011.
- [122] P. González de Alaiza Martínez, X. Davoine, A. Debayle, L. Gremillet, and L. Bergé, “Terahertz radiation driven by two-color laser pulses at near-relativistic intensities: Competition between photoionization and wakefield effects,” *Scientific Reports*, vol. 6, p. 26743, Jun 2016.
- [123] F. Enders, A. Budweg, P. Zeng, J. Lauth, T. A. Smith, D. Brida, and K. Boldt, “Switchable dissociation of excitons bound at strained cdte/cds interfaces,” *Nanoscale*, vol. 10, pp. 22362–22373, 2018.
- [124] K. M. Wurst, M. Bender, J. Lauth, S. Maiti, T. Chassé, A. Meixner, L. D. A. Siebbeles, U. H. F. Bunz, K. Braun, and M. Scheele, “Correlated, dual-beam

- optical gating in coupled organic-inorganic nanostructures,” *Angewandte Chemie International Edition*, vol. 57, no. 36, pp. 11559–11563, 2018.
- [125] D. Zhang, Z. Lü, C. Meng, X. Du, Z. Zhou, Z. Zhao, and J. Yuan, “Synchronizing terahertz wave generation with attosecond bursts,” *Phys. Rev. Lett.*, vol. 109, p. 243002, Dec 2012.
- [126] Z. Zhou, D. Zhang, Z. Zhao, and J. Yuan, “Terahertz emission of atoms driven by ultrashort laser pulses,” *Phys. Rev. A*, vol. 79, p. 063413, Jun 2009.
- [127] I. Babushkin, A. J. Galan, V. Vaičaitis, A. Husakou, F. Morales, A. Demircan, J. R. C. Andrade, U. Morgner, and M. Ivanov, “All-optical attoclock: accessing exahertz dynamics of optical tunnelling through terahertz emission,” *arXiv*, vol. 1803.04187, 2018.
- [128] J. Fan, D. Zuber, R. Mevert, T. Lang, T. Binhammer, and U. Morgner, “Kerr-lens mode locked, synchronously pumped, ultra-broadband breathing pulse optical parametric oscillator,” *EPJ Web Conf.*, vol. 243, p. 18002, 2020.

# Chapter 7

## Related publications

### Journal publications

1. I. Babushkin, C. Bree, **C. M. Dietrich**, A. Demircan, U. Morgner, and A. Husakou  
*Terahertz and higher-order Brunel harmonics: from tunnel to multiphoton ionization regime in tailored fields*,  
Journal of Modern Optics **64** (10-11), 1078–1087 (2017)
2. **C. M. Dietrich**, I. Babushkin, J. R. C. Andrade, H. Rao, A. Demircan, and U. Morgner  
*Field enhancement in a doubly resonant optical parametric oscillator*,  
Optics Letters **44** (19), 4909–4912 (2019)
3. J. R. C. Andrade, N. Modsching, A. Tajalli, **C. M. Dietrich**, S. Kleinert, F. Placzek, B. Kreipe, S. Schilt, V. J. Wittwer, T. Südmeyer, and U. Morgner  
*Carrier-Envelope Offset Frequency Stabilization of a Thin-Disk Laser Oscillator via Depletion Modulation*,  
IEEE Photonics Journal **12** (2), 1-9 (2020)
4. **C. M. Dietrich**, I. Babushkin, J. R. C. Andrade, H. Rao, A. Demircan, and U. Morgner  
*Higher-order dispersion and the spectral behavior in a doubly resonant optical parametric oscillator*,  
Optics Letters **45** (20), 5644–5647 (2020)

5. R. Mevert, Y. Binhammer, **C. M. Dietrich**, L. Beichert, J. R. C. Andrade, T. Binhammer, J. Fan, and U. Morgner  
*Widely tunable, high power, femtosecond non-collinear optical parametric oscillator in the visible spectral range*,  
Photonics Research **9** (9), 1715-1718 (2021)

## Contributions to scientific conferences

1. I. Babushkin, C. Bree, **C. M. Dietrich**, A. Demircan, U. Morgner, and A. Husakou  
Oral Presentation: *Terahertz Brunel Harmonics in Two-color Fields with Incommensurate Frequencies in the Multiphoton Ionization Regime*,  
European Quantum Electronics Conference, **EE\_2\_1**, June 2017, Munich, Germany
2. **C. M. Dietrich**, I. Babushkin, J. R. C. Andrade, L. Rust, and U. Morgner  
Oral Presentation: *2  $\mu\text{m}$  doubly resonant parametric oscillator pumped by a thin disk ultrashort laser*,  
DPG Frühjahrstagung, **Q 3.3**, March 2018, Erlangen, Germany
3. **C. M. Dietrich**, I. Babushkin, J. R. C. Andrade, L. Rust, and U. Morgner  
Poster Presentation: *Doubly-resonant 2  $\mu\text{m}$  degenerate optical parametric-enhancement cavity*,  
8th EPS-QEOD Europhoton Conference, **WeP.21**, September 2018, Barcelona, Spain
4. **C. M. Dietrich**, I. Babushkin, J. R. C. Andrade, L. Rust, and U. Morgner  
Oral Presentation: *Intracavity enhancement in a doubly resonant OPO*,  
Conference on Lasers and Electro-Optics (CLEO/US), **STh4E.2**, May 2019, San Jose, USA
5. **C. M. Dietrich**, I. Babushkin, J. R. C. Andrade, L. Rust, and U. Morgner  
Oral Presentation: *Field enhancement in an doubly resonant optical parametric oscillator*,  
The European Conference on Lasers and Electro-Optics (CLEO/Europe), **cf.1\_5**, June 2019, Munich, Germany

- 
6. J. R. C. Andrade, S. Kleinert, A. Tajalli, **C. M. Dietrich**, F. Placzek, B. Kreipe, and U. Morgner  
Oral Presentation: *Depletion based thin-disk CEP stabilization*,  
The European Conference on Lasers and Electro-Optics (CLEO/Europe), **cf\_10\_4**,  
June 2019, Munich, Germany
  7. **C. M. Dietrich**, I. Babushkin, J. R. C. Andrade, L. Rust, and U. Morgner  
Online Presentation: *On the role of higher order dispersion in a doubly resonant optical parametric oscillator*,  
Conference on Lasers and Electro-Optics (CLEO/US), **JTh2E.21**, May 2020,  
San Jose, USA
  8. **C. M. Dietrich**, I. Babushkin, J. R. C. Andrade, H. Rao, and U. Morgner  
Online Presentation: *Influence of higher order dispersion on a half-harmonic generator*,  
9th EPS-QEOD Europhoton Virtual Conference, **Th-A3.6**, August 2020, Prague,  
Czech Republic
  9. H. Rao, **C. M. Dietrich**, J. R. C. Andrade, A. Demircan, I. Babushkin, and U. Morgner  
Online presentation: *A Stabilized Doubly Resonant Optical Parametric Oscillator for Strong-Field Applications*,  
Conference on Lasers and Electro-Optics (CLEO/US), **STu1D**, May 2021, San  
Jose, USA
  10. H. Rao, **C. M. Dietrich**, J. R. C. Andrade, A. Demircan, I. Babushkin, and U. Morgner  
Online Presentation: *A Stabilized Doubly Resonant OPO for THz Applications*,  
Conference on Lasers and Electro-Optics/Europe - European Quantum Elec-  
tronics Conference (CLEO/EU), **cd\_9**, June 2021, Munich, Germany
  11. R. Mevert, Y. Binhammer, **C. M. Dietrich**, L. Beichert, J. Fan, T. Binhammer,  
and U. Morgner  
*Two ultra-broadband OPOs in the visible spectral range*, submitted 9th June  
2021,  
EOS Annual Meeting (EOSAM), September 2021, Rome, Italy



12. H. Rao, **C. M. Dietrich**, J. R. C. Andrade, A. Demircan, I. Babushkin, and U. Morgner  
Poster Presentation: *Terahertz radiation in tailored two-color laser fields with a stabilized doubly resonant optical parametric oscillator*,  
10th EPS-QEOD Europhoton Conference on Solid-State, Fibre, and Waveguide Coherent Light Sources (EUROPHOTON 2022), **TUE-P-1.7**, October 2022, Hannover, Germany
  
13. H. Rao, **C. M. Dietrich**, J. R. C. Andrade, R. Mevert, F. J. Geesmann, A. Demircan, I. Babushkin, and U. Morgner  
Poster Presentation: *A Stabilized Doubly Resonant OPO for THz Applications*,  
Conference on Lasers and Electro-Optics/Europe - European Quantum Electronics Conference (CLEO/EU), **CF-P.19**, June 2023, Munich, Germany

# Acknowledgements

There is only one name on the cover of this work, but I could never have done this alone. I want to thank all the people who have supported me during my work and studies for many years.

First of all I would like to thank Uwe Morgner for the wonderful opportunity to work on this project. Uwe has supported me all these years and always encouraged me.

I would like to thank Detlev Ristau and Carsten Fallnich for being the examiner of my thesis and Michael Oestreich as the head of the committee.

Many thanks to the members of the working group for the great years. They will remain in my memory for a long time. The scientific discussions were always an enrichment. I would also like to thank the hard-working helpers José R. C. Andrade, Han Rao, Jintao Fan, Luise Beichert, Robin Mevert, David Zuber, Stephanie Willms, Sven Kleinert and Christoph Jusko who proofread my thesis.

Also special thanks to:

- José for his critical comments. We will be on the slopes again.
- to Christoph for the many trips to the QUTIF meetings throughout Germany
- Han, who will continue my work and his useful remarks
- to Dmitrii Perevoznik, who endured my constant coffee making in his office
- to all FWJLer which I met in my time as a PHD

- to my former master student Laura Rust who accompanied me during my first steps as a PHD student
- to Felix Scheling for helping me with the stabilization
- to Kai-Martin Knaak for his help and magnificent knowledge in electronics
- to the secretary and the workshop, which help me in tricky situations and help to realize ideas for my project

Many thanks to Ihar Babushkin and Ayhan Demircan. You were always a great help with all types of theoretical and mathematical questions. Your ingenuity and ideas were always great.

At last I would also like to thank my family and close friends. My parents have always supported me and made this long study possible.

# Chapter 8

## Curriculum Vitae

### Personal Details

Christian Markus Dietrich  
Weender Straße 93  
37073 Göttingen

born 26<sup>th</sup> of December, 1988 in Goch, Germany

### Ph.D. Studies

since 12/2015      Ph.D. student at the Institute of Quantum Optics at the Leibniz  
Universität Hannover, research group of Prof. Dr. Uwe Morgner

### Related Work Experience

since 08/2021      Development engineer at Qioptiq Photonics GmbH & Co. KG,  
Königsallee 23, 37081 Göttingen

08/2014–08/2015    Intern: IFISC (Institute for Cross-Disciplinary Physics and Com-  
plex Systems), Palma, Spain, Design and Realization of a Dynamic  
Semiconductor Laser Network

07/2009–04/2010    Military Service, Koblenz, army forces command (HFüKdo)

### Education

12/2015              Final degree: Master of Science (M.Sc.) - mark "very good"

- 10/2013–12/2015 Master student at the Westfälische Wilhelms-Universität in Münster  
in physics  
master project: *Design and Realization of a Dynamic Semiconductor Laser Network*
- 10/2010–10/2013 Bachelor student at the Westfälische Wilhelms-Universität in Münster  
in physics  
bachelor project: *Noncollinear second harmonic generation with integrated gratings in lithium niobate*